OPTIMIZING MAGNETIC BEHAVIOR AND SUPERCURRENT TRANSMISSION IN FERROMAGNETIC JOSEPHSON JUNCTIONS

By

Swapna Sindhu Mishra

A DISSERTATION

Submitted to
Michigan State University
in partial fulfillment of the requirements
for the degree of

Physics—Doctor of Philosophy

2022

ABSTRACT

OPTIMIZING MAGNETIC BEHAVIOR AND SUPERCURRENT TRANSMISSION IN FERROMAGNETIC JOSEPHSON JUNCTIONS

By

Swapna Sindhu Mishra

Josephson junctions containing ferromagnetic layers are being studied for their interesting physics and potential applications in energy-efficient superconducting electronics. These ferromagnetic Josephson junctions exhibit ground state phase shifts of either 0 or π, and controlling the phase is crucial to their applications as the memory elements for a superconducting computer. Phase control in ferromagnetic Josephson junctions has been demonstrated in a pseudo-spin valve structure containing Ni as the fixed layer and NiFe as the free layer. The same magnetic layers were also used in a prototype of the cryogenic memory called Josephson Magnetic Random Access Memory (JMRAM). However, the magnetic layers currently being used need to be optimized to improve their reliability and efficiency.

The fixed layer Ni has a multidomain magnetic structure and can interfere with the free layer switching. In this work, we propose replacing Ni with an unbalanced Ni/Ru/Ni synthetic antiferromagnet (SAF) where one Ni layer is thicker than the other, in hopes of achieving better magnetic properties and reducing the interference with the free layer switching. We first characterize the magnetic properties of the synthetic antiferromagnets as a function of Ni and Ru thicknesses to find the first antiferromagnetic coupling peak at a Ru thickness of 0.9 nm. We then study the magnetic properties of balanced Ni/Ru/Ni SAFs where both Ni layers have identical thickness. We then study the supercurrent transmission through these balanced Ni/Ru/Ni SAFs and find that the decay of supercurrent with Ni thickness is very slow with a decay length of 7.5 ± 0.8 nm. Finally, we study the magnetic

properties of unbalanced Ni/Ru/Ni SAFs and find that in some cases the coercivity of the free layer switching is smaller than Ni, which could potentially lead to it being a viable replacement for the Ni fixed layer.

The free layer NiFe has better switching properties than Ni, however it exhibits poor supercurrent transmission. In this work, we add thin layers of Ni at the interface between NiFe and the Cu spacer layers in our junctions with the hope of improving their critical currents. The idea behind this is based on lessons learned from Giant Magnetoresistance studies which showed that Ni/Cu interfaces have better spin-dependent properties for supercurrent transmission than NiFe/Cu interfaces. We characterize the magnetic properties and critical currents of Ni/NiFe/Ni trilayers as a function of Ni and NiFe layer thickness. We find that the magnetic properties of these trilayers are not severely degraded compared to NiFe. For a Ni thickness of 0.4 nm, we find that the maximum supercurrent in the π-state of these trilayer junctions is increased by a factor of four relative to the NiFe junctions. We explore this idea further by replacing Cu/NiFe interfaces with Pd/NiFe interfaces, and find an enhancement of supercurrent by a factor of two. These results seem to indicate that the supercurrent through ferromagnets can be enhanced by "engineering" the interface for better spin-dependent transport properties at the interfaces.

Copyright by
SWAPNA SINDHU MISHRA
2022

To my family, friends and mentors.

ACKNOWLEDGMENTS

This dissertation work depended on the support and efforts of numerous other people and I have been very fortunate to receive the support of my colleagues, friends and family during the course of my graduate studies at Michigan State University. It might be impossible to list all the names that I want to acknowledge in the next couple of pages, however, I am thinking of each individual in my mind while I write this thesis.

First and foremost, I would like to thank Prof. Norman Birge who has been an excellent advisor each and every day I have worked in the Birge group. Norman has been a great mentor and irrespective of how busy he is, he has always been accessible for discussions and answering questions. He was very understanding of personal issues that arose from time to time and always supported me to get through them by doing what's best for me. I have learned an immense amount of physics and an equal amount of other knowledge and skills required to carry out cutting-edge research from him. I loved his advising style which can be summed up as a form of relaxed optimism that I hope to emulate someday if I get a chance to mentor students of my own.

I would like to thank Dr. Reza Loloee for acting as a support system not just for the labs but also for me. I have had countless discussions with Reza about materials and equipment among other things, which have added immensely to my knowledge. Reza was always helpful whenever any problem arose due to equipment failure or from my general incompetence. It is fair to say that this study would never have been completed without Reza's help and guidance. Along with thanking him for all his help, I would also like to apologize to him for the countless troubles I have caused him during the last four years. I would like to thank Dr. Baokang Bi for traning me in various cleanroom equipment and for his continued

maintenance of the excellent Keck Microfabrication Facility that I used significantly during this work. I would also like to thank Dan Edmunds for his technical help with equipment and stimulating discussions on electronics.

I would like to thank all members of Birge group that I interacted with and learned from directly or indirectly. I would like to thank Dr. Victor Aguilar and Alex Madden for being excellent lab guides and discussion partners. I would also like to thank Josh Willard for teaching me countless things and also shouldering the responsibility of any additional work that I could not complete myself. I would like to deeply thank Bob Klaes for teaching me the basics of sample fabrication and measurement during my early days in the group. I thank Anna Osella, Ben Byrd and Jake Crawford for suggestions, discussions and contributions. I would like to thank past graduates from the Birge group, especially Dr. Joseph Glick, Dr. Bethany Niedzielski, Dr. Eric Gingrich and Dr. Trupti Khaire from whose theses and papers I learned most of what I know about superconductor-ferromagnet physics. I would like to thank Northrop Grumman Corporation and Michigan State University for financial support for carrying out the research in Birge group.

I thank Dr. Johannes Pollanen, Dr. Mohammad Maghrebi, Dr. Andreas von Manteuffel and Prof. Joey Huston for serving on my thesis committee and providing guidance on my research. I would like to thank Kim Crosslan for being an excellent person that I could go to for any academic or non-academic help and for always being an excellent source of moral support. I would also like to thank the many teachers and mentors I had at MSU, NISER, KBRC and DAV who taught me physics and other subjects.

Lastly, I would like to acknowledge and thank my close friends and family, without whom it would have been impossible to function as a person. I would like to especially thank Stephen Hemmerle, Cameron Kilgore, Michael Pajkos, Anna Bosgraaf and Bob Klaes

among many others, for being excellent friends while at MSU and for being my home away from home. Without these people, it would have been very hard for me to thrive in this foreign land and I hope to continue these friendships from afar. I would like to thank my parents, Rabi Narayan Mishra and Sukesini Mishra, and my sister, Barsa Baisakhi Mishra, for being supportive of my career in research and always encouraging me to follow my passion in life. I would also like to thank my close friends back in India, Swarupashree Mishra, Ranjit Ranjan Das, Chinmay Anand Swain and Avishek Swain, and others who have kept in touch and were very supportive during difficult times.

TABLE OF CONTENTS

LIST OF TABLES

LIST OF FIGURES

Chapter 1

Introduction

1.1 Why work on a superconducting computer?

By 2030, total electricity demand of information and communication technology, i.e. computing, is expected to consume about 21% of the world's total electricity [1]. This massive 8000 TWh energy consumption will primarily be driven by data centers and networks with a small fraction being used by consumer devices and the production of these machines. Because of the dense packing of motherboards and other electronics in these data centers, they generate a lot of heat and need to be cooled down constantly to be optimally functional. Most of this cooling takes place with the help of billions of litres of water every year [2]. The increasing amount of water consumption, most of which is potable, can produce water stress in many communities that are already facing a shortage. The industry has slowly shifted to using non-potable water and other creative forms of cooling such as setting up data centers under ocean water or in the arctic circle where temperatures remain cold throughout the year. These practices may save costs in the short term, but they are not sustainable in the long run because of the environmental costs, complexity of doing maintenance and the concentration of suitable locations in certain geographical regions.

The main reason behind these problems is the use of conductors (metals like Cu, Al, Au etc.) and semi-conductors (Si) for the transistors, wires and other parts of the computing circuit. Conductors and semi-conductors dissipate heat during operation leading to wastage of electricity and higher cooling costs. There is a major push in the semiconductor industry

to make these devices and interconnects more efficient to increase power efficiency and reduce heating, but there is a limit to these improvements because of the scale and complexity of the circuits. However, an alternative solution to these problems exists: the Joule heating can be circumvented by replacing conventional conductors by superconductors.

There has been a significant push towards the development of a superconducting computer in the recent past as a replacement for CMOS-based computers [3–5]. Although there are many challenges to making this technology physically and commercially viable, if implemented, this would revolutionize the field of computing along with reducing the cooling costs to a fraction of the current technologies. The superconducting transition temperatures for most elemental superconductors are low. Niobium, one of the most used superconductors for electronics, has its transition temperature around 9 K. So, cooling down to liquid Helium temperature is needed to maintain its superconducting state. However, projections show that the energy use of a fully superconducting computer (after the cost of cryogenic cooling is factored in) would be 10-100 times less than that of current Si-based technologies [3]. A superconducting computer also has the potential to be used as a controller for quantum computers that operate in the millikelvin temperature range, thus reducing external noise and making the combined system more compact [6].

1.2 Present state of superconducting computing

The use of superconductors in electronics began a few decades after their discovery, for example, in the cryotron switch invented by D. Buck at MIT Lincoln Laboratory in 1956 [7]. In 1962, the Josephson junction was predicted where you can have a supercurrent flow across a thin non-superconducting layer sandwiched by superconductors [8, 9]. With the discovery

of this Josephson effect, more complex uses in electronics were envisioned; for example, IBM's Josephson project in the 1970's [10]. Josephson junctions are being used in new logic circuits; for example, Resistive Single-Flux Quantum (RSFQ) logic proposed by K. Likharev, O. Mukhanov and V. Semenov in 1985 uses pico-second voltage pulses to encode and process digital information [11, 12]. Northrop Grumman Corporation also has its own Reciprocal Quantum Logic (RQL) which uses reciprocal pairs of SFQ pulses to encode information [13]. There are many different superconducting logic architectures that have been proposed and successfully implemented in the recent years by several groups [14–19].

Although processing logic is the most important part of a computer, it cannot function without memory and storage components. The NSA's superconducting technology assessment in 2005 predicted that the limiting factor for the development of a successful superconducting computer would be the memory and storage rather the performance of the logic processor [20]. The research and development of a superconducting memory is still catching up with the advances in superconducting logic.

1.3 Superconducting memory

An ideal candidate for a superconducting memory needs to be fast, non-volatile (turning off the device still retains the information), random-access (all data stored on the device should have reasonably similar access times, regardless of their physical location) and energy efficient. The Birge group at Michigan State University is studying ferromagnetic Josephson junctions for its possible applications in a superconducting memory device that satisfies these requirements [21–26]. Other groups are also using ferromagnetic Josephson junctions towards the same goal [27–32].

The Josephson Magnetic Random Access Memory (JMRAM) proposed by Northrop Grumman Corporation uses ferromagnetic Josephson junctions [33]. The JMRAM memory architecture is loosely based on the Magnetoresistive Random Access Memory (MRAM) that might someday replace the flash-based memory devices currently in use in most CMOS computers [34]. The magnetic structures of both these devices are very similar and the information is stored in the magnetic state for both. However, the read operations are different: JMRAM reads information from the ground-state phase difference across the ferromagnetic Josephson junction [35,36] whereas MRAM reads information from the magnetic orientation directly [37]. Fig. 1.1 shows a memory cell and an array of 4 memory cells used in JMRAM. Our work at Birge group focusses on the Magnetic Josephson Junction (MJJ) element present inside each memory cell. The MJJ plays the role of a single physical bit (0 or 1 state) by adding a variable phase to the SQUID loop [21, 24, 38].

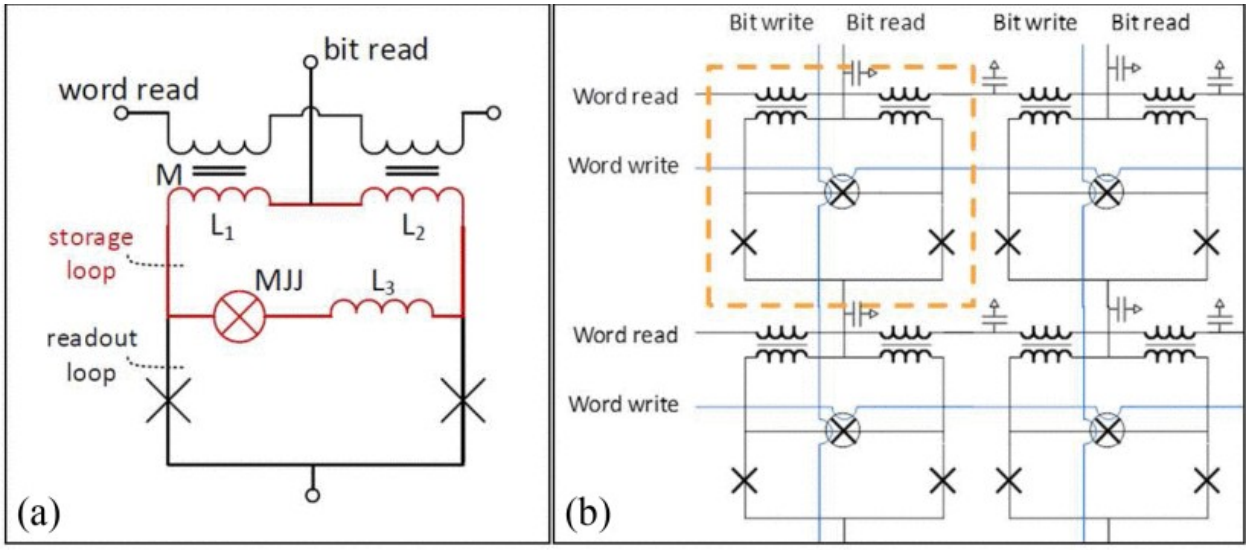

Figure 1.1: **JMRAM memory cell.** (a) A single memory cell where the X inside circle (in red) indicates the magnetic Josephson junction (MJJ) and (b) an array of 4 memory cells with read and write lines. Figure was taken from [33].

Although the JMRAM prototype has been demonstrated to work [33], there is still a long

way to go before it is reliable and commercially viable. The current size of the memory cells is much larger than flash/MRAM devices, so it needs to be much more compact for a superconducting computer to replace a CMOS computer of similar scale in terms of performance and efficiency. However, a bigger problem is the magnetic reliability and transmission efficiency of the magnetic layers of the JMRAM. The current prototype uses Ni and NiFe as the magnetic layers. Although Ni is good at supercurrent transmission when compared to other ferromagnets, it has a multidomain magnetic structure on the size scale of the current devices, which can lead to interference with the switching of the NiFe layer. On the other hand, NiFe has better magnetic switching properties but is terrible at supercurrent transmission, which limits the overall efficiency of the MJJ. In this thesis, we propose and demonstrate possible solutions to these problems by optimizing the layers for better magnetic behavior and larger supercurrent transmission.

1.4 Chapters Overview

In Chapter 2, we briefly review the theory of superconductivity, ferromagnetism and their interplay, directly relevant to the work performed in this thesis. We discuss some important aspects of the Josephson effect, superconductor-ferromagnet proximity effect and how these phenomena can be used to create a memory device.

In Chapter 3, we describe the fabrication and measurement process of our magnetic thin-films and ferromagnetic Josephson junctions. We briefly discuss the equipment used and we describe the experimental processes used in detail.

In Chapter 4, we propose Ni/Ru/Ni synthetic antiferromagnets (SAF) as a replacement for the Ni fixed layer. We study the magnetic properties of these Ni/Ru/Ni SAFs and

compare them to those of Ni. We also study the dependence of critical current as a function of the Ni thickness in the Josephson junctions containing these Ni/Ru/Ni SAFs. We see that the supercurrent decays slowly with Ni thickness for these junctions containing SAFs.

In Chapter 5, we propose solutions to improve the supercurrent transmission through the NiFe layers by adding thin layers of Ni on either side or by replacing the adjacent Cu spacer layers in the junctions with Pd layers. We base our proposals on knowledge gained from Giant Magnetoresistance (GMR) studies about the conduction properties at ferromagnet-normal layer interfaces [39]. We show that by adding thin layers of Ni, we increase the critical currents by a factor of 4-5 in the π-state of the Josephson junction. Replacing Cu with Pd shows an increase by a factor of 2.

In Chapter 6, we conclude by summarizing the results of our work. We also discuss some questions that need to be answered and areas where future work should be focused.

Chapter 2

Theory

In this chapter, we discuss the theory behind the phenomena widely used in the course of this study: superconductivity, ferromagnetism and their interactions.

2.1 Superconductivity

Superconductivity was discovered in 1911 when Heike Kamerling Onnes saw that the electrical resistance of mercury dropped from a finite value to an unmeasurably small value below 4.2 K [40]. In the early years, this novel and puzzling phenomena was considered to be an anomaly, however it is now known that many different materials exhibit this phenomena under the right conditions, i.e. low temperatures and/or high pressures. Onnes won the Nobel prize in 1913 for his discovery. In 1933, another puzzling discovery was made by Walther Meissner and Robert Ochsenfeld where they found that superconductors expel magnetic fields when they are superconducting [41]. The field of superconductivity is very much evolving and new discoveries continue to be found to this day.

The quantum mechanical reason behind the superconductivity in some conventional materials is reasonably well understood, however for many other materials the exact mechanism still remains unknown. In this work, we use Niobium as our superconductor which is a conventional superconductor and well studied. The microscopic theory describing conventional superconductors is known as BCS theory and was developed by John Bardeen, Leon Cooper and John Robert Schrieffer [42]. In this theory, conduction in superconductors happens not

via single electrons (fermionic), but via pairs of electrons (bosonic) that condense into a macroscopic quantum state.

2.1.1 The Meissner-Ochsenfeld Effect and London Theory

Meissner and Ochsenfeld dicovered in 1932 that below a certain temperature T_c, the magnetic field inside a superconductor is expelled [41]. They also observed that if the cooling takes place in the presence of a magnetic field, the superconductor becomes a perfect diamagnet. This field cancellation at T_c takes place via emergence of surface currents that perfectly negate the magnetic field inside the superconductor. The Meissner effect is uniquely seen in superconductors and is often used as a test for superconductivity.

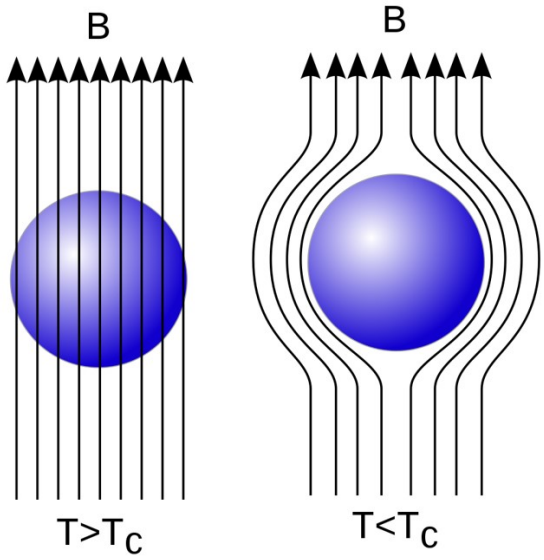

Figure 2.1: **The Meissner effect.** Left image shows superconductor (in blue) above T_c with magnetic field lines penetrating the material in the presence of a magnetic field B. Right image shows the expulsion of magnetic field below T_c. Figure was taken from [43].

One of the early explanations of Meissner effect was proposed by Fritz and Heinz London [44]. They derived equations for moving electrons inside a perfect diamagnet to describe the electromagnetic fields inside a superconductor. Applying Newton's second law to electrons in

a superconductor, the electric field $\vec{E}$ in a superconductor causes the electrons to accelerate:

$$-e\vec{E} = m\frac{d\vec{v}}{dt} \tag{2.1}$$

where e, m and $\vec{v}$ are the charge, mass and velocity of electrons, respectively. The current density $\vec{J}$ in the superconductor is given by

$$\vec{J} = -ne\vec{v} \tag{2.2}$$

where n is the density of superconducting electrons. Combining both equations, we get

$$\frac{\partial \vec{J}}{\partial t} = \frac{\vec{E}}{\Lambda} \tag{2.3}$$

where $\Lambda = m/(e^2 n)$. To replace $\vec{E}$ by the magnetic field $\vec{B}$ in the above equation, we can use the Maxwell equation

$$\vec{\nabla} \times \vec{E} = \frac{-\partial \vec{B}}{\partial t} \tag{2.4}$$

which leads to

$$\frac{\partial}{\partial t}\left[\vec{\nabla} \times \vec{J} + \frac{\vec{B}}{\Lambda}\right] = 0. \tag{2.5}$$

Thus, the quantity inside the brackets is conserved for a superconductor. The Meissner-Oschenfeld experiments suggested that inside a bulk superconductor $\vec{B} = 0$ and $\vec{J} = 0$, which leads to the London equation

$$\vec{\nabla} \times \vec{J} + \frac{\vec{B}}{\Lambda} = 0 \tag{2.6}$$

Using the Maxwell equation,

$$\vec{\nabla} \times \vec{B} = \mu_0 \vec{J} + \mu_0 \epsilon_0 \frac{\partial \vec{E}}{\partial t}. \tag{2.7}$$

and taking a curl of both sides, we get

$$\vec{\nabla} \times (\vec{\nabla} \times \vec{B}) = \vec{\nabla}(\vec{\nabla} \cdot \vec{B}) - \nabla^2 \vec{B} = \vec{\nabla} \times \left(\mu_0 \vec{J} + \mu_0 \epsilon_0 \frac{\partial \vec{E}}{\partial t} \right). \tag{2.8}$$

For an electric field approximately constant in time and using $\vec{\nabla} \cdot \vec{B} = 0$, Eqn. 2.6 and Eqn. 2.8 imply that

$$\nabla^2 \vec{B} = \frac{\mu_0}{\Lambda} \vec{B} \tag{2.9}$$

$$\nabla^2 \vec{J} = \frac{\mu_0}{\Lambda} \vec{J} \tag{2.10}$$

The length scale over which electromagnetic fields and currents can penetrate inside a superconductor is given by the London penetration depth,

$$\lambda_L = \sqrt{\frac{\Lambda}{\mu_0}} = \sqrt{\frac{m}{\mu_0 e^2 n}} \tag{2.11}$$

This implies that the fields at the surface of the superconductor decay to zero over the distance λ_L as seen in the Meissner effect.

2.1.2 BCS Theory

After London's theory, another important contribution to the understanding of superconductivity was made by Vitaly Ginzburg and Lev Landau in 1950 [45]. They used the theory of second-order phase transitions and expressions of free energy density for the superconducting

electrons to explain the Meissner effect. This theory also partially explained the Josephson effect (which will be discussed later in this chapter). Although the Ginzburg-Landau theory worked well within certain limitations, it was unable to explain the microscopic origin of superconductivity. However, it acted as a bridge between London theory and BCS theory. In 1950, another important contribution was made by C. A. Renolds [46] and E. Maxwell [47] when they showed that the T_c in superconductors varied with the mass of the element's isotopes, suggesting that superconductivity might be related to the lattice interactions.

John Bardeen, Leon Cooper and Bob Schrieffer proposed the first microscopic theory for conventional superconductors including Nb and its alloys [42]. The theory is now known as BCS theory after their last names. The electrons in most metals interact with each other through the Coulomb force and phonons, which are quantized vibrations of the crystal lattice. Fröhlich in 1952 [48] and Bardeen and Pines in 1955 [49] had shown that when two electrons exchange virtual phonons, they generate a weak attractive interaction. Within a narrow band in k-space at a low enough temperature, this attractive potential is non-zero, thus leading to the formation of a two electron bound state. Similarly, Cooper in 1956 [50] had shown that two electrons with oppositely aligned spins near the Fermi level will form a bound state in the presence of a weak attractive interaction. In 1957, Schrieffer along with Bardeen and Cooper, proposed a macroscopic quantum state of these "Cooper pairs" by extending it to an N-particle system [42].

BCS theory showed that the energy gap Δ needed for superconductivity is dependent on the temperature T. They showed that the energy gap at zero temperature is given by

$$\Delta(0) = 1.764 k_B T_c \tag{2.12}$$

where k_B is the Boltzmann constant. Experimental tests in different materials have shown that Δ lies between 1.5-2.5 $k_B T_c$ [51]. The energy gap predicted by BCS theory was first observed by Michael Tinkham and Rolfe Glover in 1956 where they saw a sharp rise in the far infrared absorption spectrum of a superconductor [52]. In 1960 Ivar Giaever also observed a similar energy gap in Al/AlO_x/Pb tunnel junctions using differential conductance measurements [53].

2.1.3 The Josephson Effect

The Josephson effect is another fascinating macroscopic quantum phenomenon arising due to superconductivity. In 1962, Brian Josephson predicted that when two superconductors are separated by a thin barrier (shown in Fig. 2.2), a supercurrent can flow even without any external bias voltage applied [8]. This is known as the dc Josephson effect and the supercurrent is given by

$$I_s = I_c \sin \phi \tag{2.13}$$

where ϕ is the phase difference between the two superconductors. The above equation is also known as the current-phase relation and is valid when the current is smaller than the critical current. Note that $\phi = \phi_2 - \phi_1$ is the difference of the macroscopic phases that are used to describe the wavefunctions of the superconductors.

When the current is larger than the critical current, a finite voltage V is present across the junction and the phase difference acquires a time dependence, given by

$$\frac{d\phi}{dt} = \frac{2eV}{\hbar} = \frac{2\pi V}{\Phi_0} \tag{2.14}$$

where $\Phi_0 = 2\pi\hbar/(2e)$ is the magnetic flux quantum. The supercurrent oscillates at a fre-

Figure 2.2: **Diagram of a Josephson junction.** The junction consists of two superconductors S_1 and S_2 (in blue) separated by a thin barrier (in orange). The intrinsic macroscopic phase of the superconductors is given by ϕ_1 and ϕ_2, respectively.

quency $\nu = 2eV/h$. The Josephson energy stored in the junction can be calculated to be

$$E = E_J(1 - \cos\phi) \tag{2.15}$$

where $E_J = \hbar I_c/2e$ is the Josephson coupling energy.

2.1.4 The RCSJ model

An ideal Josephson junction described by the Josephson effect equations will have no dissipation, however this is not the case for a physical Josephson junction. A model to describe these physical systems can be built by shunting an ideal Josephson junction described in the previous subsection by a resistance R and a capacitance C between the electrodes, as shown in Fig. 2.3.

In the presence of a bias current I, the circuit can be described by the equation

$$C\frac{dV}{dt} + \frac{V}{R} + I_c \sin\phi = I \tag{2.16}$$

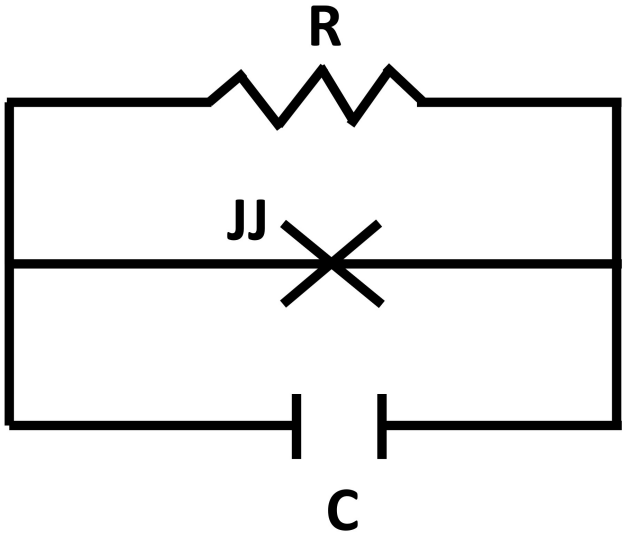

Figure 2.3: **The RCSJ model of a physical Josephson junction.** In this model, an ideal Josephson junction JJ is shunted with a resistor R and capacitor C.

Using the ac Josephson relation, we can rewrite this equation as

$$\left(\frac{\hbar}{2e}\right)^2 C\frac{d^2\phi}{dt^2} + \left(\frac{\hbar}{2e}\right)^2 \frac{1}{R}\frac{d\phi}{dt} = E_J\left(\frac{I}{I_c} - \sin\phi\right) \tag{2.17}$$

In the case of overdamped junctions, the capacitance C is small and this equation reduces to a first-order differential equation

$$\frac{d\phi}{dt} = \frac{I_c^2 R}{E_J}\left(\frac{I}{I_c} - \sin\phi\right) \tag{2.18}$$

The voltage averaged over one time period can be obtained by integrating the above equation and solving for the time period, leading to the **RSJ model**:

$$|V| = R \times \Re\left\{\sqrt{I^2 - I_c^2}\right\} \tag{2.19}$$

where $\Re$ represents the real part. The voltage remains zero for $|I| \leq I_c$ and approaches Ohm's law for $|I| >> I_c$, as shown in Fig. 2.4.

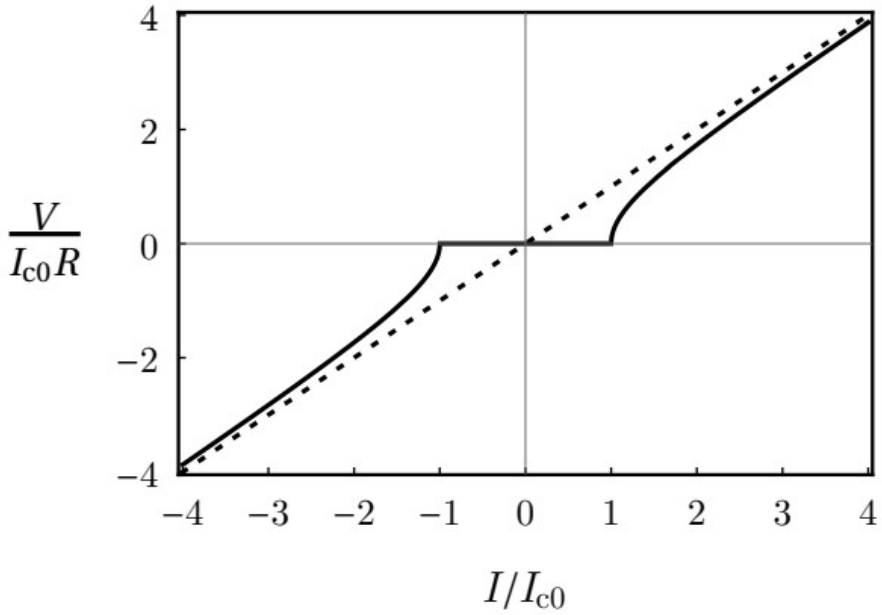

Figure 2.4: **Voltage–current curve for the RSJ model of a Josephson junction.** The votage and current are normalized. Figure was taken from [54].

2.2 Ferromagnetism

There are broadly three classes of magnetic materials: paramagnets, diamagnets and ferromagnets. This classification is based on the magnetic susceptibility

$$\chi_m = M/H \tag{2.20}$$

where H is the magnetic field applied to the material and M is the magnetization induced in the material. $\chi_m > 0$ for paramagnets (meaning they tend to align in the direction of the field), $\chi_m < 0$ for diamagnets (meaning they tend to align opposite to the direction of the field). For ferromagnets, χ_m is thousands of times higher than for typical paramagnets.

This classification was demonstrated by Pierre Curie in 1895 [55]. Curie also demonstrated that the magnetic susceptibility of paramagnets and diamagnets is inversely proportional to the temperature ($\chi_m \propto 1/T$). This is known as Curie's law and happens because thermal fluctuations destroy the magnetic ordering inside the material. However, Curie was unable to find an explanation for ferromagnetism.

Peter Weiss in 1906 tried to describe the phenomenon of ferromagnetism with the help of spontaneous magnetization and magnetic domains [56]. These postulates do not explain the quantum mechanical origins of ferromagnetism, however they are fundamental to the understanding of ferromagnets and are commonly used to this day. If a ferromagnet is cooled below a certain temperature called the Curie temperature (T_{Curie}), it develops an ordered magnetic state spontaneously. This ordered phase has a net magnetization even without an applied field. When a field is applied at a temperature T above T_{Curie}, ferromagnets follow the Curie-Weiss law (instead of the simpler Curie's law),

$$\chi_m = \frac{C}{T - T_{\text{Curie}}} \tag{2.21}$$

where C is a constant. Above T_{Curie}, ferromagnets lose the ordered phase and become paramagnetic. Ferromagnets are often found in a demagnetized state, but when a field is applied they produce a strong magnetization which persists even after the removal of the field. Weiss explained this behavior by predicting that ferromagnets consist of many magnetic domains. Inside these domains, all spins are pointed along a single direction, however the domains themselves can point in random directions, thus causing the net magnetization of the material to be nearly zero.

After the development of the field of quantum mechanics and better understanding of

spins, Werner Heisenberg [57] and Paul Dirac [58] independently showed that the origin of ferromagnetism can be explained by the exchange interaction. This interaction happens because indistinguishable particles (like electrons) are subject to exchange symmetry when two particles are exchanged. The basis of this exchange interaction is the Coulomb repulsion between the electrons. When this exchange interaction is strong, it forces all the spins to align parallel to each other which leads to spontaneous magnetization and thus leading to the phenomenon of ferromagnetism.

2.2.1 Magnetic Domains

Along with the exchange interaction between the magnetic moments, there are other factors such as the dipole-dipole interaction that play a crucial role in the ordering of moments inside a ferromagnet. Exchange is strong but has a short range while dipolar interaction is weaker but has a much longer range. The ferromagnet will seek to minimize its overall energy combined from all interactions, which can lead to the formation of magnetic domains.

Landau and Lifshitz in 1935 proposed a theory to predict the shape and size of magnetic domains and also showed that these magnetic domains can be macroscopic in size [59]. The boundaries between these domains are known as domain walls where spins rotate from the direction of one domain to another. The size of these domain walls is dependent on material characteristics but on average spans across around 100–150 atoms. Fig. 2.5 shows a domain wall between two domains pointing up and down, respectively.

2.2.2 Magnetic Anisotropy

The crystal structure of the ferromagnet can heavily influence the microscopic nature of the spins and their interactions via orbital overlaps. This can lead to directional dependence

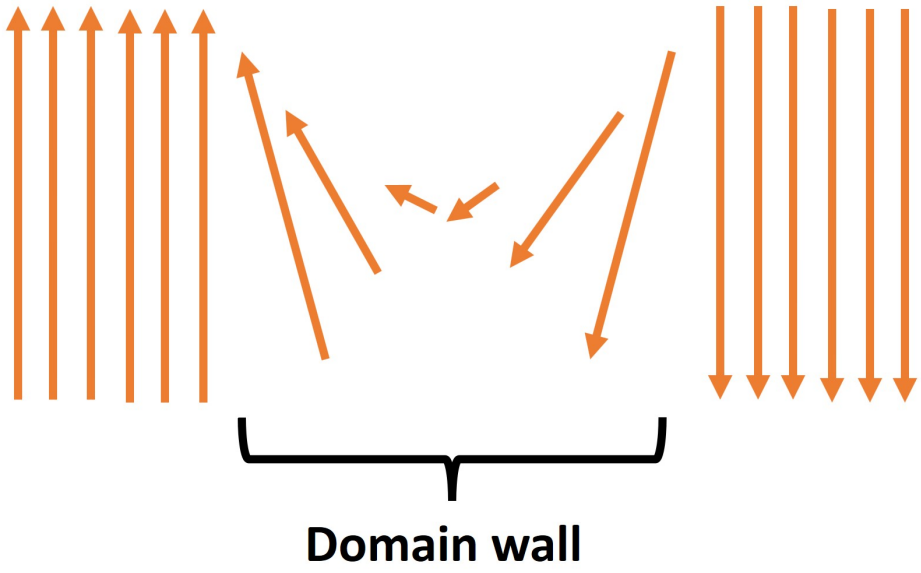

Figure 2.5: **Domains and domain wall.** The diagram shows two domains pointing up and down, respectively, separated by a domain wall. Inside a domain wall, spins rotate from one direction to the other gradually. The spins look smaller because of the perspective during rotation and not due to a change in magnitude.

of properties and this kind of anisotropy is known as magnetocrystalline anisotropy. The primary source of magneto-crystalline anistropy is the spin-orbit interaction.

It can be easier (requiring lower field or energy) to magnetize ferromagnets in a certain direction, called the easy axis. Similarly, there can be directions where it is the hardest to magnetize the ferromagnet, called a hard axis. Uniaxial and cubic anisotropy are two examples of magneto-crystalline anisotropy commonly found in ferromagnets.

Similarly, the physical shape of the ferromagnet can influence its magnetic properties. For example, in the absence of magnetocrystalline anisotropy, a sphere will have uniform properties in all directions, however an ellipse or cuboid will be easier to magnetize along the longer axis versus the shorter ones because of the non-uniformity of magnetic fields inside and outside the ellipse or cuboid. The magneto-crystalline and shape anisotropy when taken together can lead to unique directional properties dependent on the growth conditions, shape

and size (along with inherent microscopic properties) of the ferromagnet.

2.2.3 Magnetization Reversal and Hysteresis Loops

Edmund Stoner and Erich Wohlfarth in 1948 proposed a model to describe the magnetic switching of a single-domain ferromagnet [60]. Although many of the magnetic materials that are used for magnetic storage are multi-domained, the Stoner-Wohlfarth model is still relevant for their understanding. In this model (shown in Fig. 2.6) , the magnetization $\vec{M}$ is uniform throughout the ferromagnet and rotates when the magnetic field $\vec{H}$ changes. We assume that the ferromagnet has a uniaxial anisotropy constant K with easy axis along $\hat{z}$. H is applied in the xz-plane. A first order approximation of the energy per unit volume is given as

$$u = u_{\text{aniso}} + u_{\text{ext}} \tag{2.22}$$

where u_{aniso} and u_{ext} are the energy per volume due to anisotropy and the external field respectively. We can expand it further as

$$u = K \sin^2\theta - \mu_0 \vec{M} \cdot \vec{H} \tag{2.23}$$

where θ is the angle that $\vec{M}$ makes with z-axis. Defining $K = \mu_0 \beta M^2/2$, where β is a constant, we get

$$u = \frac{\beta}{2}\mu_0 M^2 \sin^2\theta - \mu_0 M(H_x \sin\theta + H_z \cos\theta) \tag{2.24}$$

Consider the simple case where H is along the easy axis (or z-axis). We can simplify the above equation to

$$u = \frac{\beta}{2}\mu_0 M^2 \sin^2\theta - \mu_0 M H \cos\theta \tag{2.25}$$

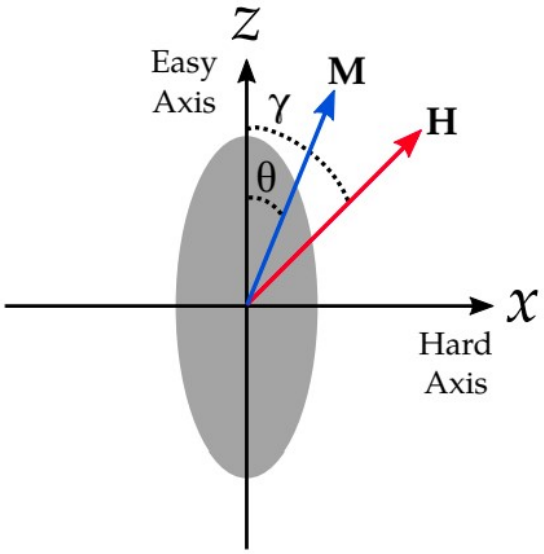

Figure 2.6: **Diagram of the Stoner-Wohlfarth model.** The easy and hard axes of the ellipse are along z and x, respectively. A magnetic field H is applied in the xz-plane which leads to a magnetization M. Figure was taken from [54].

As we can see, the energy is minimized when magnetization is aligned along the easy axis. If we take the first order derivative of this equation with respect to θ, we will see that there exist two solution curves. If H is applied in the negative z-direction, then second order derivatives show that the solution at $\theta = 0$ becomes metastable and increasing H beyond this point forces the magnetization to a new energy minimum at $\theta = \pi$, thus suddenly reversing its direction. This response of M versus H is known as a magnetization reversal curve. Because of the existence of two solutions as discussed above, the magnetization will not retrace its path when H is swept in the opposite direction. Thus a ferromagnet displays hysteretic behavior and retains the memory of the previous magnetic configuration. For the case when H is in arbitrary direction, we see a more complex behavior as shown in Fig 2.7: the magnetization curve can be more rounded depending on the angle.

However, typical M vs H curves for real materials look different: they are usually more

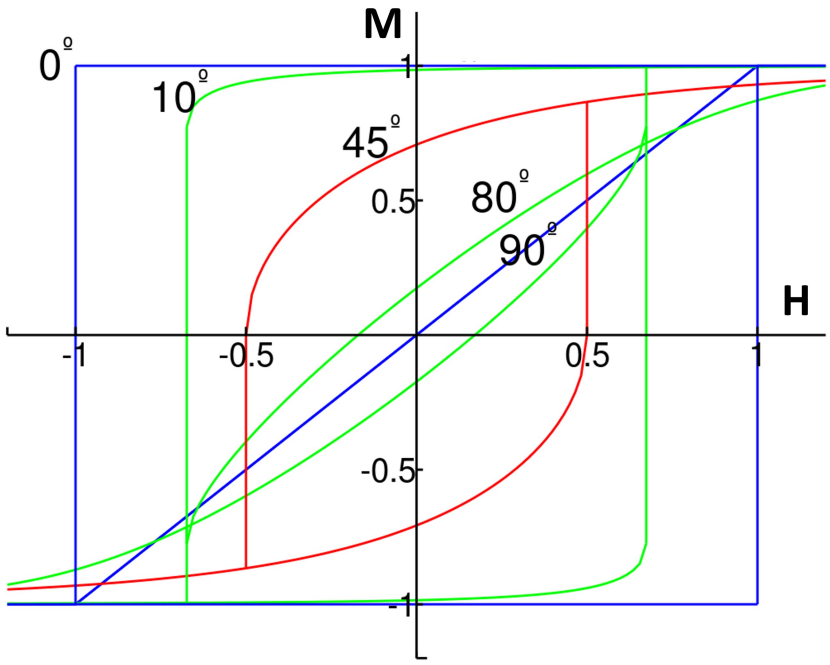

Figure 2.7: **Hysteresis curves predicted by the Stoner-Wohlfarth model.** The figure shows M vs H curves for different angles between the magnetic field and the easy axis. Figure was taken from [61].

rounded and less sharp (see Fig. 2.8). The M is non-linear with H and rises until a sufficiently large field to a constant value of M_s known as the saturation magnetization. In Fig. 2.8 M_r denotes to the remanent magnetization i.e. the magnetization that remains after the field is returned to zero. H_c is called the coercive field that must be applied in opposite direction to reverse the magnetization direction. Materials with small H_c (for example, NiFe or Permalloy) are known as magnetically soft whereas materials with high H_c (for example, Ni, Co, Fe) are known as magnetically hard.

To obtain useful information from these hysteresis curves, we fit these magnetization versus field curves to the function:

$$M(H) = M_s \times \text{Erf}\left(\frac{H - H_c}{\sqrt{2\sigma}}\right) \tag{2.26}$$

where Erf is the Gauss error function and σ is the switching width. By fitting experimental M versus H data to this function we can obtain the H_c, σ and M_s.

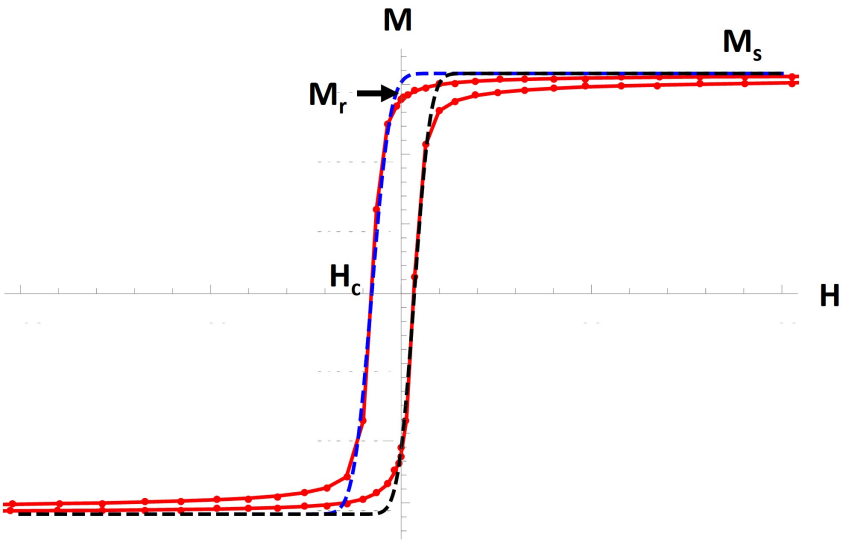

Figure 2.8: **Hysteresis curves in real materials.** The red points and red curve show experimental M vs H data and the dashed blue and black lines are fits to Eqn. 2.26.

2.3 Interaction between superconductivity and ferromagnetism

Superconductivity and ferromagnetism are thought of as inherently antagonistic forms of order. In conventional superconductors, the two electrons that form a Cooper pair have anti-parallel spins whereas in a ferromagnet the electron spins prefer to be aligned parallel to each other. As we saw earlier, superconductors expel magnetic field and similarly magnetic fields can destroy superconductivity. However, there is more to the interplay between superconductor(S) and ferromagnets(F) than just that. It has been established that magnetic fields can penetrate into the superconductor and similarly, superconductivity can leak into ferromagnets (or non-superconducting normal metals (N) or insulators (I)) via something called the proximity effect. This interaction between superconductors and ferromagnets contains interesting physics and potential for amazing applications.

2.3.1 Proximity effect at S/N interfaces

Before we study the proximity effect at S/F interfaces, we need to discuss the interaction at S/N interfaces. Holm and Meissner in 1932 found that an S/N/S junction (two superconductors separated by a thin normal metal layer) had zero resistance, which demonstrates that superconductivity can extend beyond the skin of the superconductor [62]. This interesting phenomenon is known as proximity effect. The wavefunction describing the Cooper pairs in a superconductor, known as the pair-correlation function decays into the normal metal as shown in Fig. 2.9.

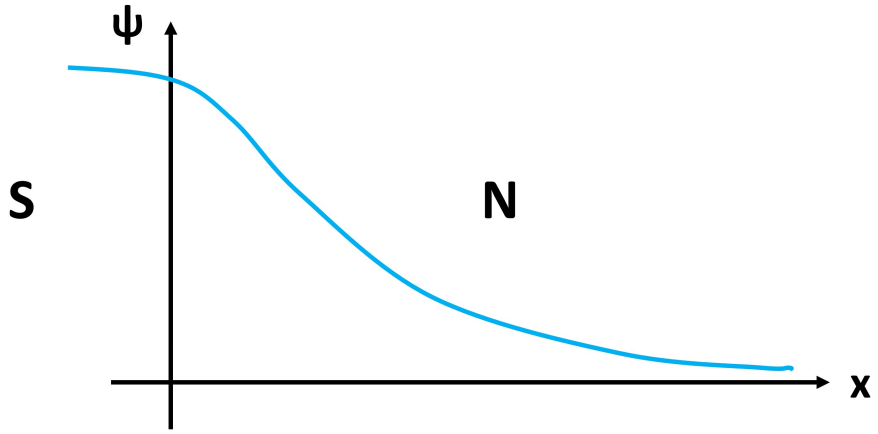

Figure 2.9: **Proximity effect at superconductor (S) – normal metal (N) interface.** The pair correlation function Ψ decays with thickness x inside N. In the case of a single superconductor and in the absence of any phase gradient, Ψ can be taken as purely real.

For some metals like Cu this decay can take place over a large thickness, up to the order of hundreds of nanometers. But how does this proximity effect take place?

Superconductors have an energy gap near the Fermi surface but normal metals do not. Because of this, for electrons near the Fermi surface, the transmission is forbidden across the S/N interface. This puzzle was solved by Alexander Andreev in 1964. He showed that although the direct transfer of single electrons across the interface is forbidden, a double

charge transfer process is permissible [63]. In this process, two electrons in the normal metal can be transferred into the superconductor to form a Cooper pair. This absence of the second electron in the normal metal can be thought of as a hole reflected at the S/N interface. For electrons moving from the superconductor into the normal metal, the opposite process happens. This mechanism is known as Andreev reflection and is shown in Fig. 2.10.

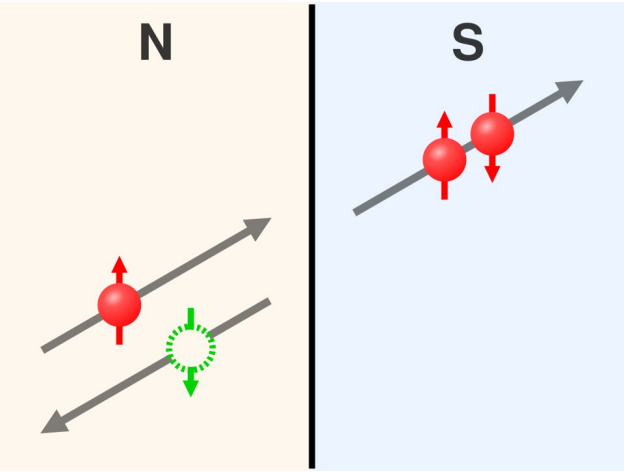

Figure 2.10: **Andreev reflection at an N–S interface.** An electron (in red) incident at the N/S interface from the N side forms a Cooper pair in S and a retroreflected hole (green) in N. Normal current in N is thus converted to supercurrent in S via this process.

Andreev reflection at a smooth interface conserves the momentum of electrons parallel to the interface by design. To conserve the total spin, the incident electron and the reflected hole need to be from opposite spin bands. This is not an issue in normal metals but is problematic for ferromagnets, as we will see later. Andreev reflection also preserves the phase coherence of the electrons and the reflected holes up to a certain distance. This length scale varies with temperature, material properties and impurities. When the transport is ballistic (without any disorder or scattering) the coherence length in the normal metal is given by

$$\xi_{N,\text{ballistic}} = \frac{\hbar \nu_F}{2\pi k_B T} \tag{2.27}$$

where ν_F is the Fermi velocity, k_B is the Boltzman constant and T is the temperature. When the transport is diffusive (with disorder and scattering), the coherence length is given by

$$\xi_{N,\text{diffusive}} = \sqrt{\frac{\hbar D}{2\pi k_B T}} \tag{2.28}$$

where D is the diffusion constant.

2.3.2 Proximity effect at S/F interfaces

The proximity effect is significantly altered when we replace the normal metal with a ferromagnet. As we discussed earlier, Andreev reflection now has to account for the electron pairs occupying different spin bands which can lead to the suppression of this process [64,65]. Ferromagnets have very short correlation length for the Cooper pairs leading to fast decay of the supercurrent over short distances inside the ferromagnet [66]. However, along with this rapid decay, the pair correlation function shows an interesting behavior: it oscillates! The oscillation of the pair-correlation function was first predicted by Fulde and Ferrel in 1964 [67] and Larkin and Ovchinnikov in 1965 [68] for bulk superconductors in the presence of an exchange field. This is often referred to as the FFLO state after their last names. The oscillation at the S/F interface is similar in nature to the FFLO state, however the exact mechanism is different.

To explain this fascinating behavior, let us consider a simplified model of ferromagnets similar to the one used by E. Demler, G. Arnold and M. Beasley in their 1997 work on the proximity effect [69]. In this model the spin-bands are parabolic in k-space with a gap of twice the exchange energy E_{ex} with the spin-up direction having lower energy, as shown in the Fig 2.11. Let us also consider only spin and center of mass components for the pair

correlation function for simplicity.

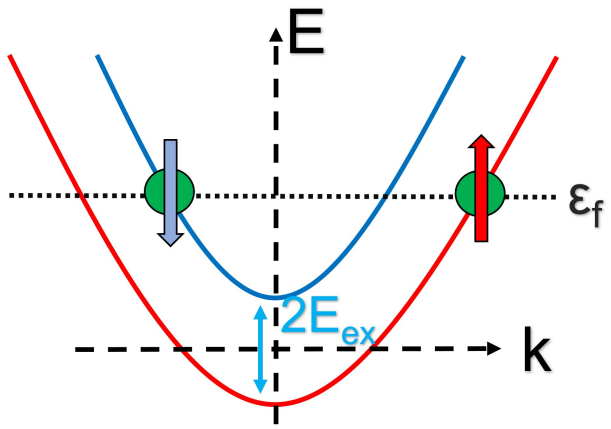

Figure 2.11: **A simplified model of spin bands in a ferromagnet (F).** The diagram shows two electrons in opposite spin bands near the Fermi energy. The spin-bands are parabolic in k-space with a gap of twice the exchange energy E_{ex}.

In the S layer, the Cooper pairs then have the spin-singlet wavefunction.

$$\Psi = \frac{1}{\sqrt{2}}(|\uparrow\downarrow\rangle - |\downarrow\uparrow\rangle) \tag{2.29}$$

When oppositely aligned Cooper pairs enter the ferromagnet, they occupy different spin bands as shown and have different wavevectors $k_F^{\uparrow}$ and $k_F^{\downarrow}$, respectively. Since the potential energy of the electrons changes (spin-up decreases by E_{ex} and spin-down increases by same amount), their kinetic energies must also change to conserve the total energy. This imparts a net center of mass momentum to the Cooper pair given by

$$\hbar Q = \hbar(k_F^{\uparrow} - k_F^{\downarrow}) \approx \frac{2E_{\text{ex}}}{\nu_F} \tag{2.30}$$

Thus the $|\uparrow\downarrow\rangle$ state will acquire $+\hbar Q$ momentum while the $|\downarrow\uparrow\rangle$ state will acquire a $-\hbar Q$

momentum. Thus the wavefunction can be rewritten as

$$\Psi = \frac{1}{\sqrt{2}}(|\uparrow\downarrow\rangle\, e^{iQX} - |\downarrow\uparrow\rangle\, e^{-iQX}) \tag{2.31}$$

where X is the center-of-mass coordinate for the Cooper pair. Expanding the exponential to sine and cosine, we get

$$\Psi = \frac{1}{\sqrt{2}}[(|\uparrow\downarrow\rangle - |\downarrow\uparrow\rangle)\cos QX + i(|\uparrow\downarrow\rangle + |\downarrow\uparrow\rangle)\sin QX] \tag{2.32}$$

The cosine term is the spin-singlet component while the sine term is the spin-triplet component of the wavefunction. If we consider a more general case, the electrons make an incident angle θ with the interface. So the momentum change is given by $\hbar/(\nu_F \cos\theta)$ in the x-direction and zero in y and z. Integrating over all angles of incidence, the average Cooper pair distribution for the spin-singlet component in the ballistic limit is given by

$$\Psi \propto \frac{\sin(x/\xi_F)}{x/\xi_F} \tag{2.33}$$

where

$$\xi_{F,\text{ballistic}} = \frac{\hbar\nu_F}{2E_{\text{ex}}} \tag{2.34}$$

Thus, in the ballistic limit, the pair correlation function oscillates and decays algebraically. In the diffusive limit, the spin-singlet pair correlation function oscillates and decays exponentially [70] and is given by

$$\Psi \propto \exp(-x/\xi_F)\sin(x/\xi_F) \tag{2.35}$$

where

$$\xi_{F,\text{diffusive}} = \sqrt{\frac{\hbar D_F}{E_{\text{ex}}}} \tag{2.36}$$

where D_F is the diffusion constant.

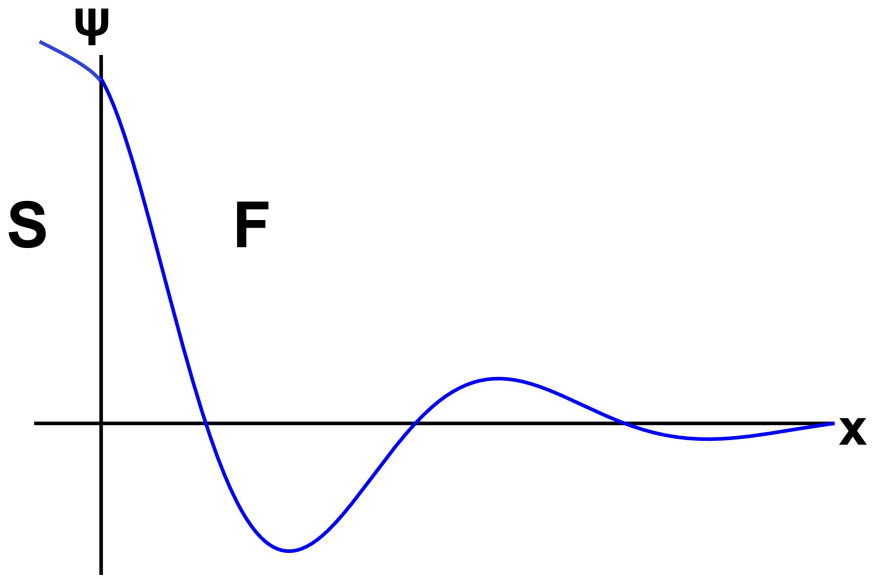

Figure 2.12: **Proximity effect at an S–F interface.** The pair correlation function Ψ decays and oscillates with thickness x inside F. For a single superconductor and in the absence of any phase gradient, Ψ can be taken as purely real.

For strong ferromagnets the exchange energy is relatively large, resulting in a coherence length of the order of a nanometer.

2.3.3 Phase ocillations in ferromagnetic Josephson junctions

We saw that the pair correlation function oscillates between positive and negative values for S/F interfaces with the F layer thickness. This oscillating effect when combined with the Josephson effect in a S/F/S junction results in a situation where the equilibrium phase difference between the two superconducting electrodes is either 0 or π depending on the thickness of the F layer, as shown in Fig. 2.13. The 0-phase junctions have the same energy

as conventional Josephson junctions discussed earlier in Eq. 2.15:

$$E(\phi) = E_J(1 - \cos\phi) = \frac{\hbar I_c}{2e}(1 - \cos\phi) \tag{2.37}$$

The minimum energy is when the phase $\phi = 0$. In π-phase junctions, the energy is given by

$$E(\phi) = E_J(1 - \cos(\phi - \pi)) = \frac{\hbar I_c}{2e}(1 - \cos(\phi - \pi)) \tag{2.38}$$

The minimum energy is when the phase $\phi = \pi$.

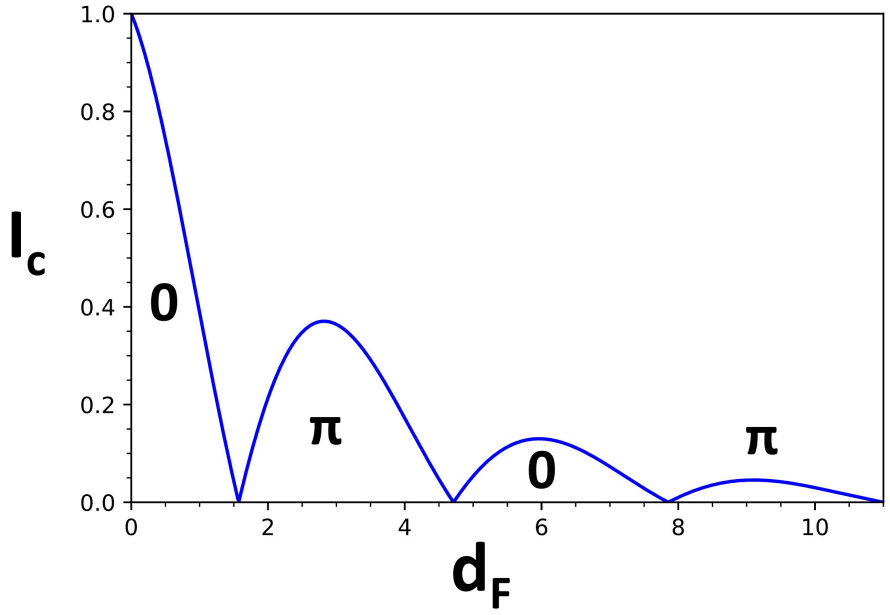

Figure 2.13: **Phase oscillations in an S/F/S Josephson junction.** The critical current I_c oscillates between 0 and π phases and decays as a function of F layer thickness d_F.

This effect was predicted by Bulaevskii *et al.* in 1977 for magnetic impurities in S/I/S Josephson junctions [71] and by Buzdin *et al.* in 1982 for S/F/S Josephson junctions [66]. The first experimental verification of π-junctions was performed in the early 2000's by V. Ryazanov [72] *et al.* and T. Kontos *et al.* [73]. It should be noted that in S/F/S junctions,

only two distinct values of ϕ are allowed: 0 or π as shown by Buzdin *et al.* in 1982 [66].

2.3.4 Fraunhofer effect in ferromagnetic Josephson junctions

Let us consider the case for short Josephson junctions where the distance between the superconducting electrodes d is small compared to the width of the junction. Let us assume that the thickness of each superconducting electrode t is much larger than the London penetration depth λ_L. We also assume that the critical current density through the junction J_c is homogeneous. Let us first consider the case where $\vec{M} = 0$ to simplify the derivation. We will then modify the results to account for the internal magnetization of the F layer.

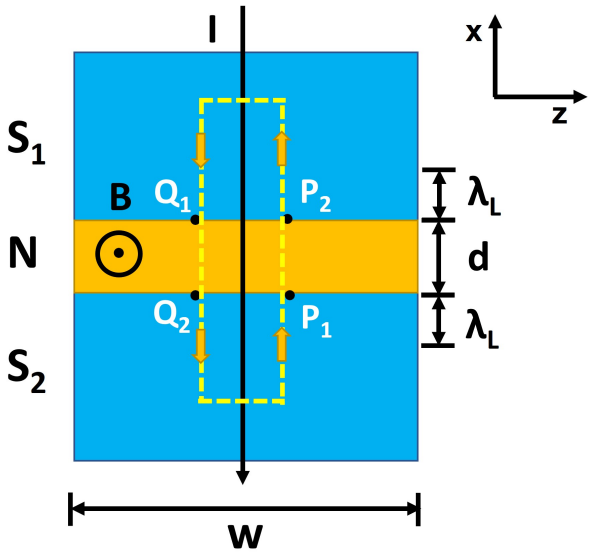

Figure 2.14: **Geometry for Fraunhofer pattern derivation in a Josephson junction.** The figure shows a rectangular cross-section with width w and length l (along y, not visible here). The thickness of the normal metal spacer layer is d. The integration path is shown in yellow dotted lines. The magnetic field is along y and the current is flowing along $-x$.

Let us consider four points Q_1, Q_2, P_1 and P_2 along a loop that extends deep into the superconductors, separated by a small dz on the z-axis, as shown in Fig. 2.14. The phase

accumulation around the closed loop is given by

$$\Delta\phi = 2\pi\frac{\Phi}{\Phi_0} \tag{2.39}$$

where $\Delta\phi = \phi_P - \phi_Q$, $\phi_Q = \phi_{Q_1} - \phi_{Q_2}$ and $\phi_P = \phi_{P_1} - \phi_{P_2}$. There are no contributions to this expression from the current density since both integrations along the z-direction vanish deep in the superconductor and the integrations along the x-direction cancel the contributions from the adjacent paths dz away. The flux in the closed path is given by

$$d\Phi = Btdz \tag{2.40}$$

where $\vec{B} = B\hat{y}$ and $t = d + 2\lambda_L$. Combining the two equations above, we get

$$\Delta\phi = 2\pi\frac{Bt}{\Phi_0}dz \tag{2.41}$$

Integrating over z, we get

$$\phi(z) = \frac{2\pi tB}{\Phi_0}z + \phi(0) \tag{2.42}$$

The supercurrent density is then given by

$$J_s(z) = J_c \sin\phi(z) = J_c \sin\left(\frac{2\pi tB}{\Phi_0}z + \phi(0)\right) \tag{2.43}$$

Integrating over area, we get the supercurrent,

$$I_s = \int J_s(z)dA \tag{2.44}$$

Josephson junctions with a rectangular cross section of length l and width w will lead to a supercurrent

$$I_s = \int_{z=-w/2}^{w/2} \int_{y=-l/2}^{l/2} J_c \sin\left(\frac{2\pi tB}{\Phi_0} z + \phi(0)\right) dydz = J_c wl \frac{\sin(kw/2)}{kw/2} \sin\phi(0) \tag{2.45}$$

where $k = \frac{2\pi tB}{\Phi_0}$. The total flux in the junction is

$$\Phi = B(d + 2\lambda_L)w. \tag{2.46}$$

Using $kw/2 = \pi\Phi/\Phi_0$ and $J_c wl = I_c$, we get the maximum supercurrent as a function of the flux,

$$I_c(\Phi) = I_{c0} \left| \frac{\sin\left(\frac{\pi\Phi}{\Phi_0}\right)}{\frac{\pi\Phi}{\Phi_0}} \right| \tag{2.47}$$

This dependence of I_c with Φ is known as the Fraunhofer pattern, because of its similarity to the pattern in single slit diffraction of light.

For a junction with a circular cross section, we use the polar coordinates instead and following similar steps, the maximum supercurrent is found to be

$$I_c(\Phi) = 2I_{c0} \left| \frac{J_1\left(\frac{\pi\Phi}{\Phi_0}\right)}{\frac{\pi\Phi}{\Phi_0}} \right| \tag{2.48}$$

This function is known as an Airy pattern. Although this formula is derived for circular junctions, it is also valid for elliptical junctions if the field is parallel to one of the principal axes of the ellipse. We plot both the Fraunhofer pattern and the Airy pattern in Fig 2.15.

For the above derivation, we assumed that $\vec{M} = 0$. However, for junctions with ferromagnetic layers, the magnetization M is non-zero. Assuming a single magnetic domain, we

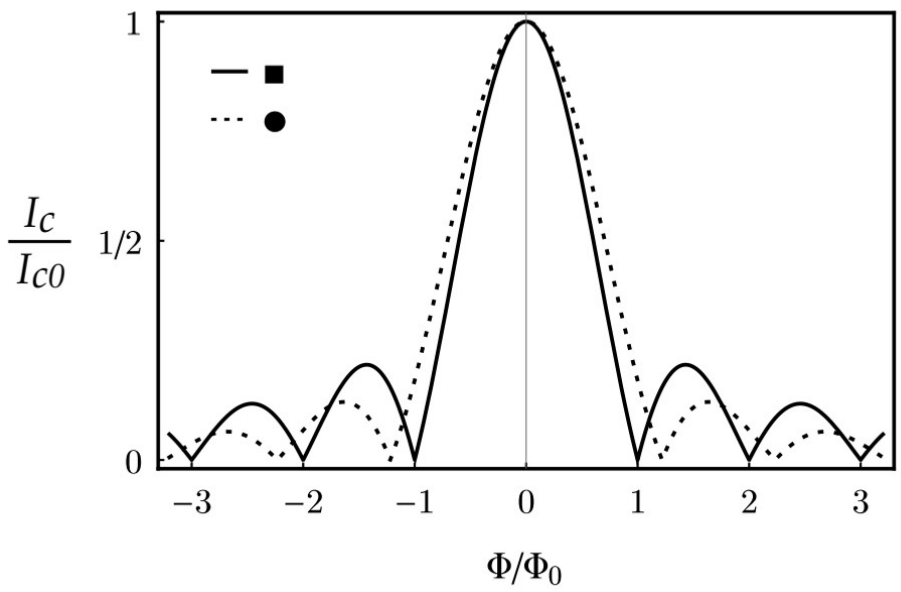

Figure 2.15: **Current-flux relation for rectangular and circular Josephson junctions.** Solid lines show the Fraunhofer patterns (normalized I_c vs Φ) for rectangular Josephson junctions and dashed lines show the Airy pattern for circular Josephson junctions. The normalized current oscillates as a function of the normalized flux. Figure was taken from [54].

can follow similar steps with a modification to the total magnetic flux:

$$\Phi = B(d + 2\lambda_L) + \mu_0 M w d_F \tag{2.49}$$

where d_F is the thickness of the ferromagnetic layer, w is the width of the junction. The Fraunhofer pattern for a ferromagnetic Josephson junction is shown in Fig. 2.16.

The Fraunhofer pattern is shifted by an amount

$$H_{\text{shift}} = -\frac{M d_F}{2\lambda_L + d} \tag{2.50}$$

There is another feature seen in Fig. 2.16: there is a sudden drop in I_c at a certain field in either direction. This is due to the hysteretic nature of the ferromagnetic layers. When the applied field becomes large enough to counter the H_c of the F layer, the magnetization

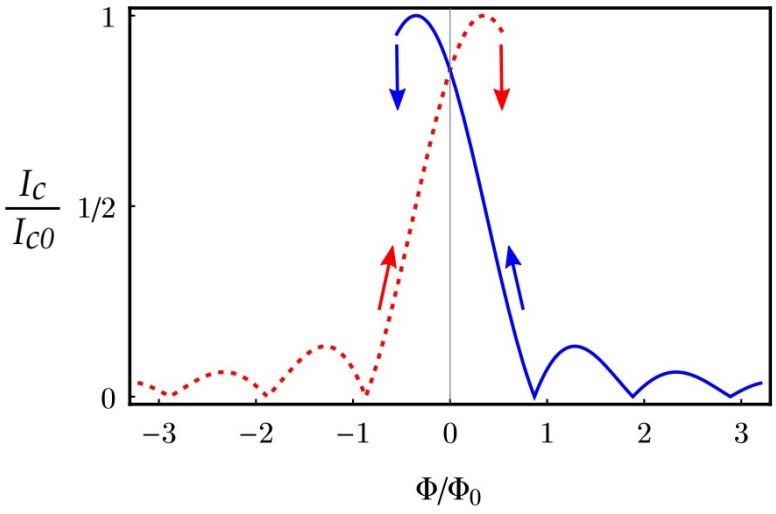

Figure 2.16: **Fraunhofer pattern for a ferromagnetic Josephson junction.** The downsweep is shown in solid blue line and the upsweep is shown in dashed red line. The normalized I_c oscillates as a function of the normalized Φ. The patterns are shifted in either direction due to internal flux from the ferromagnetic layers. The sudden drop in critical current is due to switching of the magnetization of the ferromagnetic layers. Figure was taken from [54].

changes sign. This switches the Fraunhofer pattern into a different curve solution.

2.3.5 Dependence of critical current on ferromagnetic layer thickness

As discussed previously, the critical current I_c of the ferromagnetic Josephson junctions depend on the thickness of the ferromagnetic layer d_F. Since the areas of the junctions can vary in experimental studies, it is more helpful to study the product of I_c with normal state resistance R_N to compare these Josephson junctions. Since resistance is inversely dependent on the junction area, the product I_cR_N can be compared independent of the junction area.

The behavior of I_cR_N versus d_F has been theoretically predicted in various cases. In the case of ballistic transport, the dependence is oscillatory (between 0 and π) with an algebraic decay [66], whereas for the case of diffusive transport, the dependence is oscillatory with an exponential decay [74]. The crossover from ballistic to diffusive limit has also been

studied [75, 76]. In the ballistic limit, the behavior is governed by Eilenberger equations whereas for the diffusive limit, Usadel equations are used assuming nearly identical properties for majority and minority spin bands. However, for strong ferromagnetic materials the Usadel equations are not valid [75]. There have been some studies where microscopic calculations have been performed for ballistic systems based on the Bogoliubov-deGennes equations, but the band structres used were not realistic [77,78]. Theoretical calculations of critical currents that take into account the complex band structures of ferromagnets were performed recently by Ness *et al.*, however they only studied Ni [79].

In this work, we use Ni and NiFe ferromagnets with Cu and Pd spacer layers between them and Nb as the superconducting layer. There have been no detailed theoretical studies of realistic ferromagnetic systems and effect of interfaces on the critical currents, however it is possible to use existing theoretical formulas to fit the experimental data. For example, some works have used the algebraic decay in ballistic transport to fit data for Ni [80] and Co [81]. The data from our group do not fit well to the algebraic decay, but fit well to the exponential decay which suggests that the transport in these junctions is diffusive in nature [82]. The equation for diffusive transport is given by

$$I_c R_N = V_0 \exp\left(\frac{-d_F}{\xi_{F1}}\right)\left|\sin\left(\frac{d_F - d_{0-\pi}}{\xi_{F2}}\right)\right| \tag{2.51}$$

where ξ_{F1} and ξ_{F2} are the length scales that control the decay and oscillation period of the $I_c R_N$ with d_F, V_0 is the maximum $I_c R_N$ and $d_{0-\pi}$ is the thickness at which the $0-\pi$ transition takes place.

Chapter 3

Experimental Techniques

3.1 Methods and Equipment

Various experimental techniques were used in the fabrication of samples and their measurement during the course of this thesis work. We discuss the general usage of the equipment below and will discuss the methods specific for our work in later sections.

3.1.1 Sputtering

Sputtering is used for the uniform deposition of metals in thin layers during sample fabrication. Sputtering processes can vary a lot, but in general, ionized atoms are used to eject metals from a source and these metallic vapors are then deposited onto a sample. The whole process takes place in a vacuum chamber which is required for the creation of a plasma and by controlling the rate and energy of these ionized atoms, one can control the rate and quality of the deposition.

The sputtering system used in this work is shown in Fig. 3.1. It can accommodate eight guns at present arranged in a circular pattern. Four of these guns are large DC triode magnetron guns with 2.25 inch sputter targets, three are small DC magnetron guns with 1 inch sputter targets and the last gun is an ion mill. Therefore we can sputter 7 different materials in a single run and also remove materials with an ion mill to clean the sample layers before sputtering. The guns have outlets for argon gas which is then ionized by a tungsten filament placed inside the gun parts at low vacuum (1-2 mTorr). The density of

plasma created by the interaction between Ar atoms and electrons from the tungsten wire can be controlled by controlling the current through the filament and the plasma current. The electrons are guided by a magnetic field created from permanent magnets near the gun. The sputter targets are biased with a negative voltage which attracts the Ar^+ ions to collide and knock the metal atoms off the target and onto the samples. This deposition rate can be controlled by changing the target voltage and the plasma current. The target voltage and current values for commonly used materials in large DC triode magnetron guns are listed in Table 3.1. The power settings for small DC magnetron guns are listed in Table 3.2.

Material (Symbol)	Target Voltage (V)	Target Current (A)	Sputter rate (Å/s)
Niobium (Nb)	600	0.6	4.7
Aluminium (Al)	300	0.45	1.8
Permalloy (Py)	350	0.35	2.3
Nickel (Ni)	250	0.35	1.4
Nickel (Ni)*	160	0.3	0.7
Palladium (Pd)	130	0.44	2.7
Silver (Ag)	100	0.3	1.0

Table 3.1: **Power settings and sputter rates for large DC triode magnetron guns.** The target voltages, target currents and sputter rates for different materials are listed. The * symbol signifies special settings used for Ni layers thinner than 0.5 nm.

The guns are covered by a shutter plate on top that can be used to control the open/close of big/small guns. Chimneys are also placed on top of the guns to avoid cross-contamination between guns. The samples are arranged in a circle on a sample plate which goes on top of the shutter plate. Both these plates are attached to motors that are computer-controlled via a Labview program. To accurately measure the deposition rate, the sample plate is equipped with a crystal vibration based film thickness monitor taking into account the density of the

Material (Symbol)	Power (W)	Sputter rate (Å/s)
Copper (Cu)	19	4.7
Gold (Au)	20	6.5
Ruthenium (Ru)	10	0.5
Silver (Ag)	10	1.5

Table 3.2: **Power settings and sputter rates for small DC magnetron guns.** The power settings and sputter rates for different materials are listed.

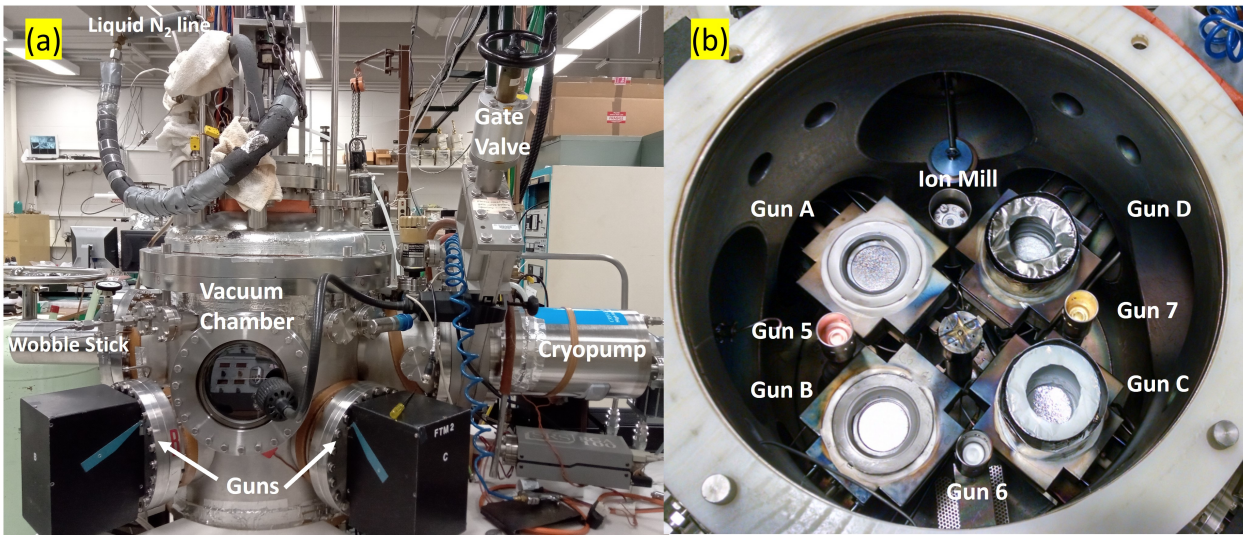

Figure 3.1: **Images of sputter chamber and guns.** (a) Sputter chamber with important visible parts labeled. (b) Sputter guns with targets and ion mill. Gun A, B, C & D are large guns and Gun 6, 7 & 8 are small guns. The large guns are in various stages of assembly to show the sputter targets and the gun parts. Figure (b) was taken from [54].

sputtered material. The chamber is connected to a roughing pump and a cryopump to create a base pressure in the low 10^{-8} Torr range. After testing the guns, the chamber is baked for 8 hours at around 100 °C to release water vapor from the chamber walls. The water is adsorbed by activated charcoal in the cryopump. The chamber is then continuously pumped overnight or longer to create an extremely clean environment. The chamber is also connected to an argon gas purifier and a Meissner trap cooled by liquid nitrogen to trap water, both of which are turned on prior to the run. The sputtering is typically performed at an argon

pressure of 2.5×10^{-3} Torr and sample temperature between -15 °C and -25 °C. The chimneys and sample plates are covered with fresh aluminum foil to avoid contamination and buildup of materials with multiple runs. The sample shutter parts are cleaned in acid before each run to remove deposited materials. The shutters along with the sample holders are then scrubbed and cleaned in an ultrasonic bath of acetone, alcohol and water each for 10 to 15 minutes and then blow dried in high heat for maximum cleanliness.

3.1.2 Photolithography

Photolithography is a useful technique to create patterns in deposited layers. The process is highly reproducible and can be used to create feature sizes of a few microns in the contact-based process typically used by university cleanrooms. Feature sizes can be smaller than 100 nm with the deep-UV projection process used in industrial cleanrooms. The pattern is copied from a photo-mask onto the film by using ultraviolet light and photo-sensitive chemicals (photoresist). First the photoresist is spun and baked onto a Si chip. The chip is then placed under a photomask and is exposed to UV light. In the case of positive photoresists, the exposed area becomes soluble in a developer chemical. In the case of negative photoresists, the exposed area becomes insoluble in the developer. After development, the pattern emerges on the chip. Materials can then be deposited in the empty spaces of these patterns or materials in the unwanted areas can be removed with a chemical or mechanical etch process.

We use photolithography for patterning the bottom and top leads of our Josephson junctions. Clean Si chips are first placed on a Resist Spinner which uses vacuum to hold the chips in place while spinning at high speeds. The positive photoresist we typically use is Microposit S1813-G2 which is then spun onto the substrates. The chip is then placed inside an oven and baked to harden the photoresist. For the bottom lead, we use an additional

layer of photoresist LOR below the S1813-G2 layer to create wider undercuts at the bottom for material deposition. The LOR layer is spun and baked in a similar way to S1813-G2, but at different rpm and temperatures. For the top lead we only use the S1813-G2 layer. After baking, the chip is placed on a sample stage in an ABM mask aligner (shown in Fig. 3.2) and held down in place by vacuum. The mask is similarly placed on top of another stage and held down by vacuum. The sample stage is then raised slowly to almost touch the mask. The mask aligner has a microscope to look at the relative alignment between the sample and the mask. The alignment can be manually adjusted linearly in X and Y axis and rotationally along the plane. Features that require precise alignment can be made with the help of vernier marking features incorporated into the mask (and by extension onto the chip in a previous lithography step). After alignment is complete, the UV light (with peaks around 365 nm and 405 nm) exposes the chip. For the bilayer, the chip is developed in MIF319 developer whereas for the single layer, it is developed in Developer 352, both followed by a rinse in water and blow drying. The pattern can now be verified under a microscope to make sure the process went as expected. The sample is now ready for material deposition.

After the material deposition, the samples go through a lift-off process to remove the residual photoresist and material deposited on top of the photoresist. We use warm PG remover or acetone for this lift-off process. Once the material starts lifting off, this is followed by an ultrasonic bath in PG remover or acetone to fully remove the layers that might be stuck, followed by a rinse in water and blow drying. Since there could be a few monolayers of photoresist still on the chip, we place the chip in a plasma etcher at low power to "descum" the chip.

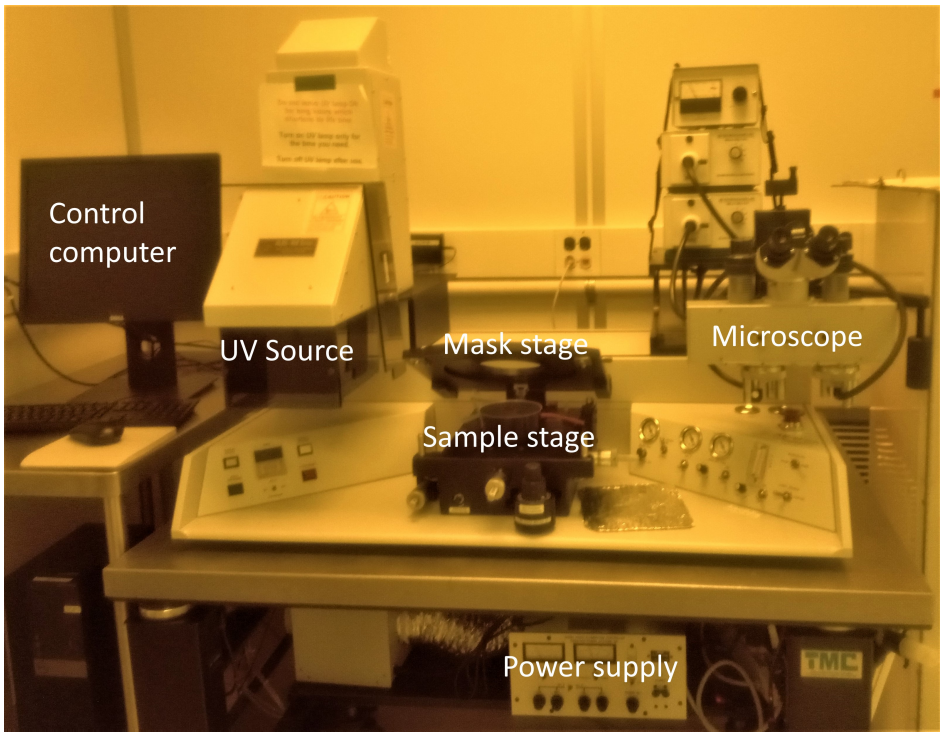

Figure 3.2: **Image of ABM Mask Aligner.** Important parts are labeled. Because of the photo sensitive nature of the photolithography process, the room lighting is yellow.

3.1.3 Electron-beam Lithography

For features smaller than a few microns, contact-based photolithography is no longer precise and accurate. So, a different lithography method that uses electron beam for exposure is used. The method is similar in principle to the photolithography process outlined above, however there are some important distinctions. The resist (positive or negative) is sensitive to electrons instead of ultraviolet light and the exposure happens via a fine-tuned computer-controlled pattern of electron beams instead of a physical mask. We use electron-beam lithography for the fabrication of elliptical Josephson junctions and for the fabrication of magnetic pillar arrays.

A negative e-beam resist ma-N 2401 is first spun onto a clean Si chip on the Resist Spinner. The chip is then placed on a hotplate and baked to harden the resist. After baking,

the chip is transferred onto a plate which is then placed inside a Hitachi SU5000 Scanning Electron Microscope (SEM) at vacuum (shown in Fig. 3.3). The sample stage is then raised slowly to be around 15 mm below the electron beam source. The beam is then started using appropriate settings. For Josephsons junctions, the settings used are: aperture 4, spot size 1, intensity 30 and beam current of around 60 pA. For magnetic pillar arrays, the settings used are: aperture 3, intensity 25 and beam current 450 pA. The focus and stigmation is then adjusted at very high magnification using a stigmation sample with helpful patterns. The magnification is then returned to a low setting (200X) and the target area of the sample is found. The sample is then aligned using 2 sets of markers set down during previous stages of sample fabrication at 200X and 1000X, respectively. The alignment is done with the help of Nanometer Pattern Generation System (NPGS) software. The elliptical pattern of $1.25\,\mu m \times 0.5\,\mu m$ is then written at the desired areas (usually at 3 places per chip). In addition, a pinwheel and a bigger ellipse are written away from the pillars. These features help in knowing whether the e-beam lithography went well and also for later during the lift-off stage. For arrays, just the ellipse pattern is written several million times which can take several hours to complete.

After the writing is complete, the junction samples are removed from the SEM and are developed in a AZ-MIF 300 developer to remove the resist everywhere except the exposed places. The sample is then rinsed in water and blow dried and the pattern is verified under a microscope. The sample is now ready for further processing using Ion Milling and silicon oxide depositon (discussed later) after which the resist is removed in warm PG remover. Because of the small size of these patterns and added materials, the junctions are sometimes hard to lift-off and therefore we use a Q-tip to scrub the junction area to aid in the lift-off. The sample is then rinsed in IPA, water and then blow dried. The samples are then checked

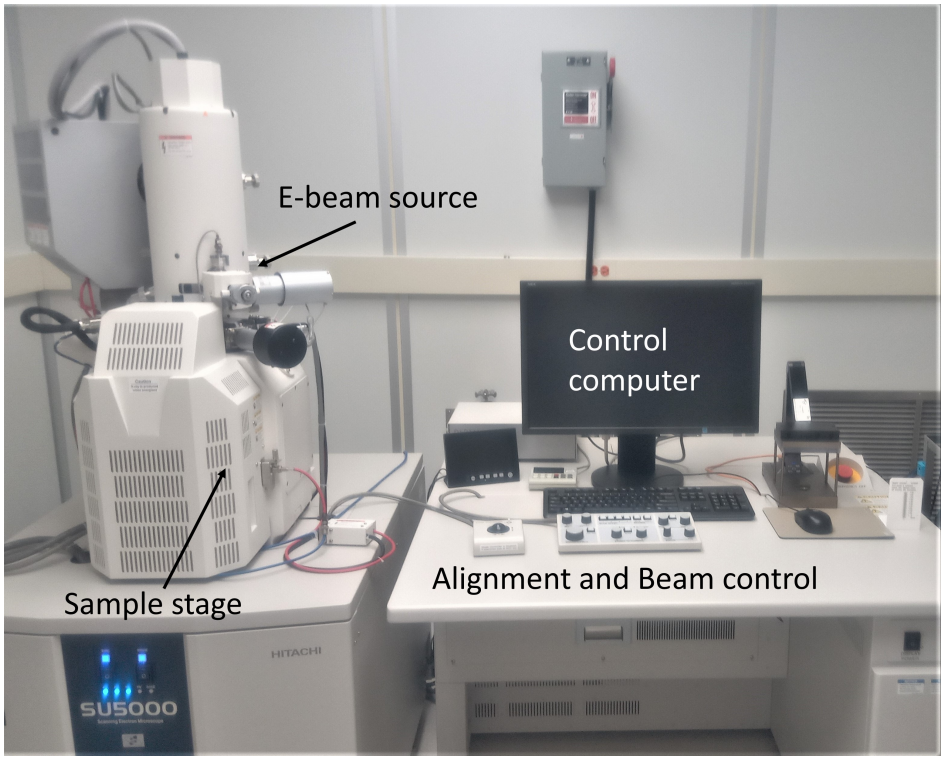

Figure 3.3: **Image of Hitachi SU5000 Scanning Electron Microscope (SEM).** Important parts of the SEM are labeled.

under an optical microscope to verify that the lift-off is complete. For arrays, the process is different and will be discussed later.

3.1.4 Ion Milling and Thermal Evaporation of SiO_x

Ion milling is a process used to etch metal layers using energetic ions and we use it for defining the areas of our Josephson junctions. In ion milling, argon atoms are ionized at low vacuum and the target sample is bombarded with them to remove atoms from the sample surface. The ionized argon atoms are produced by heating a tungsten filament. This ion beam is then accelerated by a graphite grid biased with negative voltage. A neutralizer filament is used to reduce mutual repulsion of ions by injecting electrons into the beam. By controlling the Ar flow, beam, accelerator and neutralizer currents and voltages, one can

control the rate and energy of the Ar atoms and therefore, the rate of metal removal from the sample. The process works similar to sputtering but in this case the energetic ions are used for material removal from the sample instead of deposition onto the sample.

The chamber we use for ion milling is shown in Fig. 3.4 and is a smaller version of the sputtering chamber discussed earlier. Instead of a cryo-pump, we have a continually running turbo-pump connected to the main chamber. The main chamber is rarely opened to the atmosphere directly (unless changing targets, filaments or performing diagnostics) and so no baking is necessary most of the runs. The chamber has 3 guns: an ion milling gun, a small 1 inch sputtering gun for gold deposition and a thermal evaporator for silicon oxide deposition. The guns are covered by a shutter plate with a small opening slightly larger than the guns. The sample plate is placed above the shutter plate and has 5 sample holders, a film thickness monitor (FTM) and an opening similar to the shutter plate. Both the shutter and sample plates are connected to poles placed below and above the chamber, respectively. The top of the chamber is connected to a load-lock which can be opened/closed to the main chamber with the help of a gate valve. Samples can be loaded into the load lock using a magnetic probe with the gate valve closed, the load lock can then be pumped to low vacuum using a roughing pump and then the samples loaded into the chamber by opening the gate valve. This way, the main chamber is never directly open to outside and clean vacuum can be maintained for quick operation. Once the samples have been loaded, it takes 4-5 hours for the chamber to reach the required pressure. First we sputter some gold onto the FTM. The ion mill is then turned on and set to the following values: beam voltage = 300 V, accelerator voltage = -30 V, discharge voltage = 39 V, beam current = 9 mA and neutralizer current = 9.5 mA. Then we align the FTM on top of the ion mill and measure the milling rate. Layer thicknesses of metals can be converted into equivalent thickness of Au using the

k-factor values which have been previously measured. The samples are milled for a time that is calculated based on this equivalent Au thickness. Metal is etched everywhere except under the elliptical pattern of e-beam resist, thus forming a pillar. The samples are covered with a physical mask which opens only the junction area to milling and protects the outside areas where the junction leads are located.

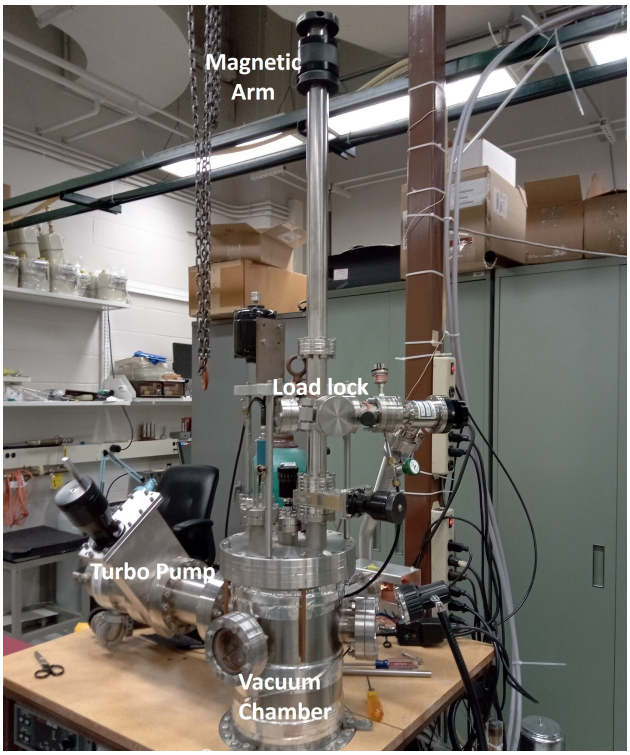

Figure 3.4: **Image of vacuum chamber for ion milling and silicon oxide deposition.** Visible important parts of the chamber are labeled.

Once the pillar has formed, it is necessary to cover the rest of the chip. This protects the pillars from damage and also creates an insulating layer between the bottom leads and the future top leads to avoid any shorts. The insulating material we use for our process is silicon oxide (SiO_x). SiO_x is is deposited on the chips using thermal evaporation where a current is passed through a boat containing SiO_x pellets. The pellets sublimate when heated and this vapor is deposited onto the samples directly above. The rate of deposition can be controlled

by controlling this current. To maintain the uniformity of the layers in all directions, the sample is slowly rotated during the deposition.

Once the SiO_x has been deposited, the samples are taken out and put into different holders which hold them vertically at a low angle. The samples are then placed inside this chamber again for side milling on each side. The side milling removes excess SiO_x on the side walls of the resist and makes it easier for them to lift-off.

3.1.5 SQUID Magnetometry

A SQUID (Superconducting Quantum Interference Device) can be used to measure extremely small magnetic fields of the order of 10^{-14} T. The SQUID magnetometer we use in our lab is a state-of-the-art system built by Quantum Design and is called the Magnetic Property Measurement Systems 3 (MPMS3). The MPMS3, shown in Fig. 3.5, has a superconducting magnet that can generate magnetic fields up to 7 T and can control the sample temperatures in the range of 1.8-400 K. The field and temperature controls have sensitive feedback loops that enable extreme precision and accuracy. Along with a DC SQUID magnetometer, the MPMS3 also has Vibrating Sample Magnetometer (VSM) capability which can achieve even better sensitivity than a normal SQUID. In the VSM mode, the sample is vibrated at a preset frequency inside a set of pickup coils. The induced voltage can then be measured, which is proportional to the product of the magnetic moment, vibration frequency and vibration amplitude.

The sample (thin films or elliptical arrays) is first cut into a small piece that can be inserted inside a straw. The straw along with the sample is then mounted on a probe and inserted inside the MPMS3. After finding the sample position with the strongest signal, the chamber is purged with He and then pumped to a low He pressure (for thermalization of the

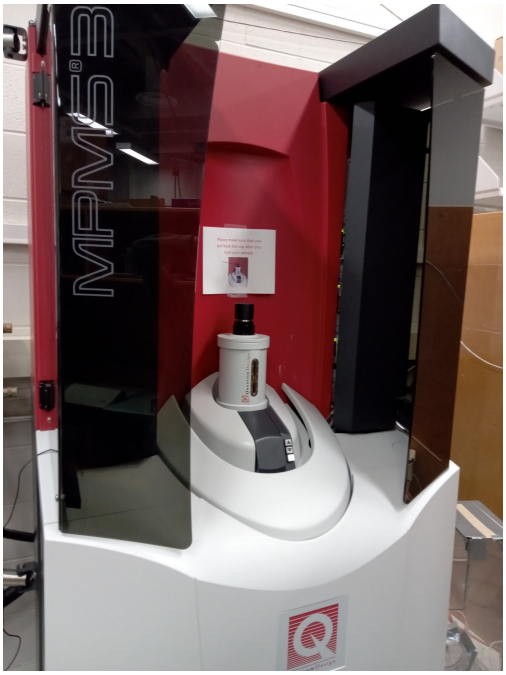

Figure 3.5: **Image of Quantum Design MPMS3.** Most parts are hidden inside the housing.

sample) and then cooled to the necessary temperature (usually 10 K). The moment versus field curves are then measured with appropriate field limits and other settings.

3.1.6 Transport Measurement Probes

We measure the transport properties of ferromagnetic Josephson junctions at various magnetic fields at a temperature of 4.2 K. To do this, we use low-temperature measurement probes built in-house by Prof. William Pratt, peripheral electronics and a Dewar filled with liquid helium. Two different probes and electronic systems were used for this project: Quantum Dipper I (QD-I) and Quantum Dipper IV (QD-IV). Both probes have capability to do four-probe $I - V$ measurements, and have a superconducting magnet to generate persistent fields up to 1 T. QD-I is more sensitive and can measure extremely small voltages down to tens of pV because it contains an rf-SQUID circuit inside. It is also very compact and has the magnet (and its wires) mounted on the probe itself while QD-IV has them in

an external sheath with separate wire connections. QD-IV is simpler and less sensitive but has different capabilities. Because it doesn't have a SQUID inside, we can put more wires inside without worrying about space or noise and has the capability to switch between 5 different junctions on a single chip while QD-I can only measure one junction during each dip. Since the magnet and the sample probes are separate, we can also do sample changes much more quickly because we only need to warm/cool the thinner sample probe. Samples with high critical currents are usually measured with QD-IV while samples with very low critical currents are measured with QD-I. Both probes are shown in Fig. 3.6.

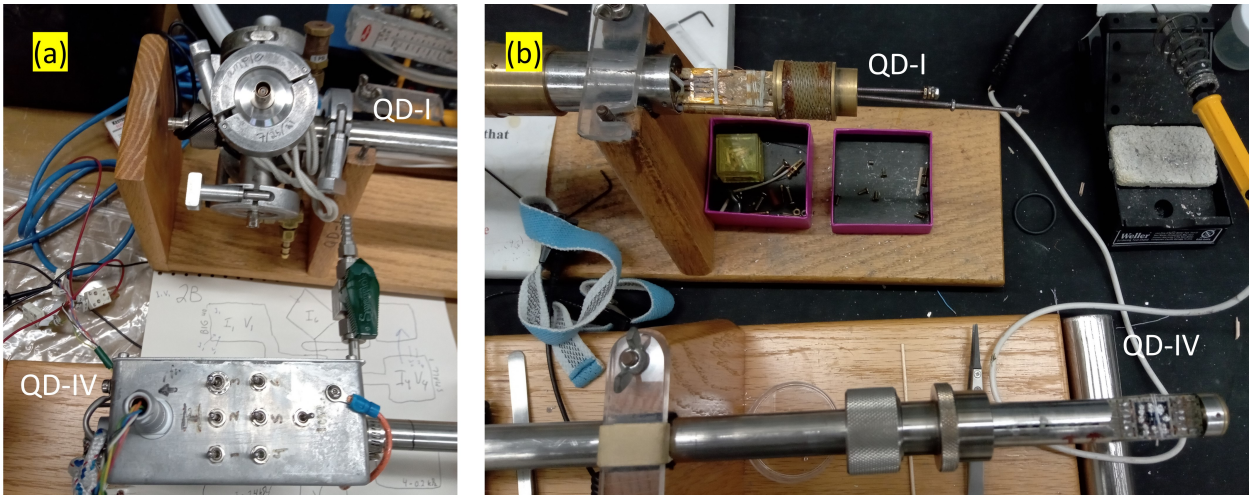

Figure 3.6: **Images of the top and bottom parts of Quick Dipper I and IV.** (a) The top part of QD-I and QD-IV where connections are made to the peripheral electronics for measurement. (b) The bottom part of QD-I and QD-IV where the sample is mounted and connected to $I-V$ leads. For QD-I, this part also contains a superconducting magnet, whereas for QD-IV, the magnet is contained in a separate sheath.

QD-I is equipped with a rf-SQUID comparator circuit to measure extremely small voltages. The circuit diagram for the rf-SQUID comparator is shown in Fig. 3.7. The sample is represented by the resistor R_s and connected to an inductor and a reference resistor R_{ref} in a loop. This loop is then coupled to an rf-SQUID through a transformer. When biased with a current, the Josephson junction sample will develop a voltage and a change in this

voltage will induce a current in the SQUID loop. This results in a change in the flux of the rf-SQUID which is detected by SQUID controller (Quantum Design 2010) outside. It then outputs a feedback voltage V_{out} that passes through a feedback resistor R_F and R_{ref}. This feedback maintains a balance between the sample and the reference resistor. In the limit of infinite open-loop gain, the voltage can be inferred using the formula:

$$V_s = V_{\text{out}} \left(\frac{R_{\text{ref}}}{R_{\text{ref}} + R_F} \right) \tag{3.1}$$

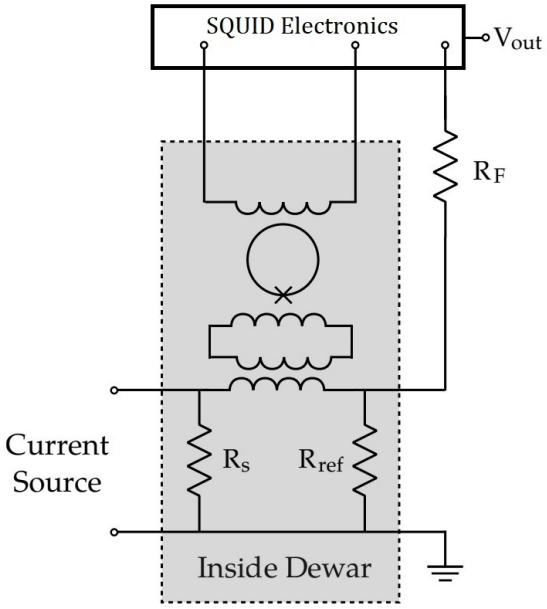

Figure 3.7: **Schematics of the rf-SQUID comparator circuit in QD-I.** The rf-SQUID is inductively coupled to an LC circuit through a transformer. The LC circuit contains the sample with resistance R_s and a reference resistor R_{ref}. This leads to large amplification of very small voltage changes with low rms voltage noise. Figure was modified from [54].

Using the values of $R_{\text{ref}} = 126\,\mu\Omega$ and $R_F = 2\,\text{k}\Omega$, we can see that the voltage gain is of the order of 10^7. So in principle, V_s can be extremely small, down to the order of picovolts for a measurable output with low noise.

The sample is first mounted on the probe and fixed in place using cotton threads. The

current and voltage ($I-V$) measurement wires are then attached to the leads with the help of indium blobs. The probe is then dipped in the liquid He Dewar slowly and connected to the peripheral electronics. For QD-IV, the peripheral electronics consist of a nano-voltmeter, separate current sources for the sample, magnet and persistence switch and a box to switch between the 5 pillars. For QD-I, the peripheral electronics consist of a voltmeter, separate current sources for the sample (built in-house and powered by 12 V batteries to isolate noise from the main power line), magnet and persistence switch and the SQUID controller box. Once connected, the current sources can be controlled by a LabVIEW program on a nearby computer and voltages can be read simiarly within the same software. The software can save the $I-V$ curves taken at each field point and another software can help with the plotting and analysis of the raw data.

3.2 Fabrication process for thin-films

The fabrication steps for thin-films is detailed below:

1. Silicon wafers are diced into chips of size 0.5 inch $\times$ 0.5 inch. To protect the wafers during the dicing, S1813-G2 photoresist is spun and baked on them beforehand.

2. The chips (usually up to 16 in a single run) are then taken to the cleanroom where they are rinsed in acetone to remove excess resist and then placed inside test tubes filled with acetone. The test tubes are then placed in a beaker together and placed in an ultrasonic bath for 15 minutes.

3. The acetone is then replaced with isopropyl alcohol (IPA) and the test tubes are placed in the bath for 15 more minutes. The IPA is then poured out and the chips are

transferred into a beaker with water one at a time. After swishing them for about a minute, they are removed and blow dried with a nitrogen gas gun.

4. The chips are then placed in a Plasma Etcher in vacuum. Plasma is then turned on in the presence of oxygen at 300 W for 300 s to clean the chip thoroughly.

5. The chips are then placed inside clean sample holders for the sputtering chamber. The holders have a copper heat sink to keep the samples cool during the sputtering process. If the deposition involves NiFe (Permalloy), a magnet is placed between each sample and the heat sink to create a field for setting the magnetocrystalline easy axis direction. The holders are cleaned prior to this step by scrubbing with a metallic brush and then placing them in an ultrasonic bath of acetone, alcohol and water in sequence. Then they are heat dried to remove all moisture. The sample holder masks are also placed in a 3:1 solution of nitric acid and water for 45 minutes before the scrubbing step. We sometimes add a drop of hydrofluoric acid if necessary to remove persistent metal deposits.

6. The sample holders with the chips are then loaded on the sample plate of the sputter chamber. This is done after the targets, gun parts, chimneys and shutter plate are in-place (sometimes, it also involves regenerating the cryo-pump a couple of hours beforehand). The sample plate is then lowered into the chamber, the chamber is closed, and the roughing pump is turned on to achieve low vacuum pressure of around 10^{-2} mTorr.

7. The roughing pump valve is then closed and the chamber is opened to the cryopump fully using a gate valve. It takes roughly 20 minutes to reach a pressure below 10^{-6} mTorr which is low enough to test the guns.

8. The water supply to the guns is turned on for cooling and the power supply to the large guns is turned on. The Ar gas is then turned on and cryopump valve closed a few turns to increase the pressure to $10^{-2} - 10^{-1}$ Torr. The plasma is then turned on and once it stabilizes, the pressure is slowly reduced to around 2.5×10^{-3} Torr.

9. The target power supplies are then turned on and the voltages are slowly increased in steps of 50 V every 20 s. The voltage and current (or power) required for sputtering vary with each target material and depend on the required rate and quality of deposition (see Table 3.1 and Table 3.2). Once the appropriate voltage and current are reached, the guns are left on for 5 minutes to check for any problems in the plasma stability and fluctuations in target/gun power supplies. The small guns are then turned on and checked for a couple of minutes. If there are persistent problems, the chamber needs to be reopened and examined.

10. If there are no problems, the targets, guns, Ar supply are then switched off. The chamber is then baked for 8 hours with the cryopump valve only open for 10 turns. Water supply to the small guns is left on during baking to avoid overheating.

11. The cryopump valve is then left open fully for several hours (preferably overnight) to pump the chamber pressure as low as possible.

12. On the day of the sputter run, the gas purifier is first turned on. The nitrogen gas lines and liquid nitrogen lines are connected to the sputter chamber. The sample is cooled down to around -20 °C. The temperature is constantly monitored throughout the sputtering process to keep it in the range of -15 to -25 °C.

13. The guns and plasma are then turned on at high pressure and then the pressure is

reduced to the sputtering pressure. The target power supplies are then turned on and the voltages and currents are ramped up to the required amount.

14. The deposition rates are then measured with an FTM and then sequence files for the sputtering process are prepared. The deposition rates are usually remeasured every couple of samples.

15. The sputtering process is started. It involves opening the sample holder mask by using a wobble stick in the beginning and closing it at the end for each sample deposition. It also involves turning the small guns on/off when required.

16. After all the samples have been sputtered, the targets are turned off followed by the plasma and the Ar gas. The nitrogen gas and liquid lines are disconnected. The heaters for the chamber are turned on. Once the chamber reaches room temperature, the chamber is opened.

17. The samples are then removed from the holders in the clean room, and put in glass vials with appropriate labels. The samples are ready to be measured.

3.3 Fabrication process for nanomagnet arrays

The fabrication process for pillar arrays is slightly more complicated and is detailed below:

1. Steps 1-16 for thin-film fabrication are followed first.

2. The chips are then placed on the Resist Spinner and ma-N 2401 is spun at 3000 rpm for 40 s. The resist is then baked on a hotplate at 90 °C for 60 seconds.

3. A mark is made on the top right of the chip to select a starting point for the arrays.

4. The chips are then transferred into the SU5000 SEM and the vacuum is turned on. The electron beam is turned on and the stigmation is done. After that, the beam is focused at the point where the scratch was made.

5. The array-writing program is then run to write the arrays. This process can take several hours and hence is left overnight to run by itself.

6. After the completion of the run, the samples are taken out and developed in AZ-MIF 300 developer for 10 s. The patterns are now complete and the chips ready for ion milling to remove magnetic layers everywhere except under the pillar patterns.

7. The samples are placed in the ion-milling holders in thermal contact with Cu heat sinks (to avoid too much heating during ion milling) and the holders are transferred into the small chamber using the load lock. The chamber is left to pump down overnight.

8. Once a favorable pressure is reached, we deposit Au on the FTM. The ion mill power supply is then turned on and stable settings are achieved. The Au is then milled off to check the milling rate.

9. The samples are milled enough to remove all the magnetic material. Once the milling is complete, the power supply is turned off and the samples are removed via the load lock.

10. Normally, we would lift off the resist for Josephson junction pillars, however since we are only going to perform magnetic measurements, the non-magnetic resist can be left on the chip and no lift off is necessary.

11. The chips are then attached to a Si wafer by adding a few drops of S1813-G2 and baking them in the oven at 90 °C for 1 hour.

12. The wafer with the chip is then placed on the resist spinner and completely covered with S1813-G2. It is then spun at 5000 rpm for 50 s. The wafer with the chip is then baked at 110 °C for 2 hours to make it dry.

13. The wafers are then taken to the dicer where only the part containing the arrays are diced off for measurement. The pattern is 99 × 39 bits repeated 45 × 55 times as shown in Fig. 3.8. The arrays give us approximately 9.5 million bits which have enough signal to be measured by the SQUID magnetometer.

14. The diced samples are removed from the wafer and the chip and are now ready for measurement.

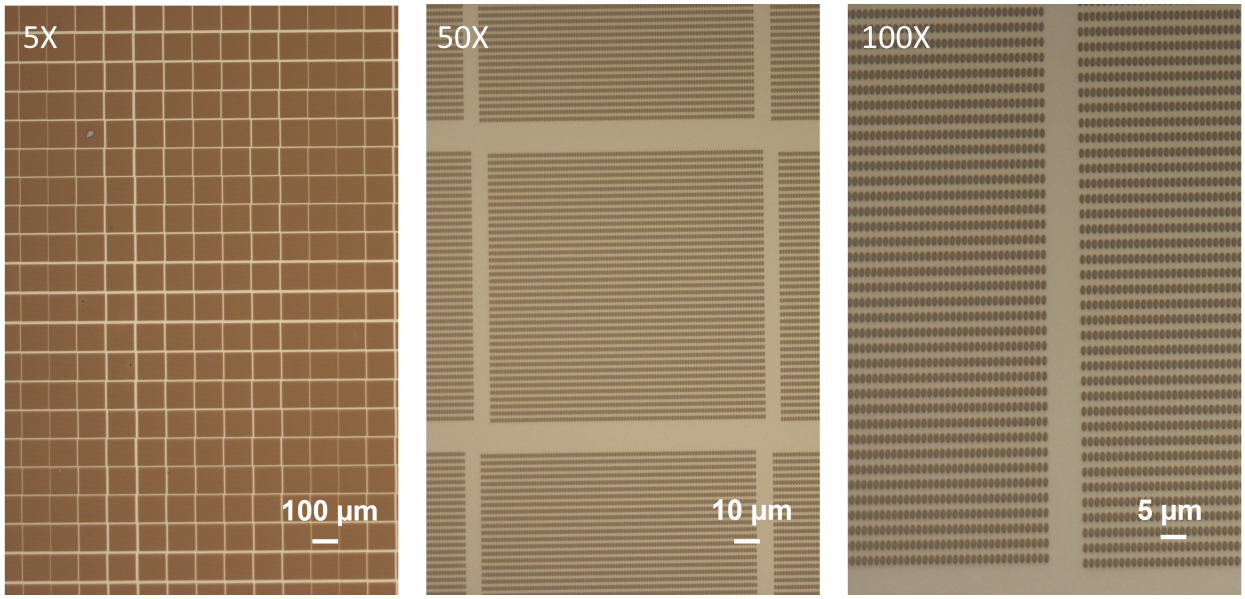

Figure 3.8: **Images of pillar arrays after fabrication.** The images were taken using an optical microscope at 5X, 50X and 100X magnification with scale bars shown at the bottom. Each pillar measures 0.5 µm × 1.25 µm. Each square pattern is 100 µm in dimension and contains 99 × 39 pillars. The pattern is repeated 45 x 55 times on the chip to form the sample.

3.4 Measurement process for thin-films or nanomagnet arrays

The measurement process for thin-films and nanomagnet arrays is similar and is detailed below:

1. The thin-film samples are put on a flat and soft surface and the backs are scribed at the center using a sharp diamond scribe. The chip is then broken into two equal pieces at the outline. The same process is repeated again on one half to form quarters. The sample is now ready to be placed in the straw. The pillar arrays are ready for the straws after the dicing process and do not need to go through this step.

2. The sample pieces are then slowly guided inside a plastic straw with the help of a thin wooden stick. Once the samples reach the necessary location, the straw is trimmed to the appropriate size. The straws are then mounted on a thin carbon fiber rod and lowered into the SQUID magnetometer.

3. A small field (usually a few hundred Oersteds) is applied and the sample center with the strongest signal is found for alignment. The field is then turned off.

4. The chamber is then purged a couple of times and pumped out. The temperature is lowered to around 10 K (sometimes we measure samples at room temperature i.e. 298 K or various other temperatures).

5. The sample is then aligned again at a small field. Because the straw and the rod shrink at low temperatures, the sample can move about 2 mm between room temperature and low temperature.

6. The field is then turned on to the requested value using a computer program and the magnetic moment is measured. This is done along downsweep and then upsweep again

at a fixed (or carefully decided variable) field step size to measure the moment versus field curves. The data are saved digitally and can be extracted later for analysis.

7. The field is then turned off, the chamber is warmed back to 305 K and the sample straw is removed.

8. The sample pieces are preserved and taken to the cleanroom for area measurements under a microscope. We can also perform area measurements using a picture taken with a phone camera and ImageJ program, but the area estimates are less accurate.

3.5 Fabrication process for Josephson junctions

The fabrication process for Josephson junctions is time consuming and has multiple steps. The schematics are shown in Fig. 3.9 and images of the pillar under optical microscope in various steps are shown in Fig. 3.10. The process is as detailed below:

1. Steps 1-4 for thin-film fabrication are followed first.

2. The chips are then placed on the resist spinner. LOR is spun at 4000 rpm for 50 seconds and then baked at 180 °C for 45 minutes in the oven. S1813-G2 is then spun on the chips at 5000 rpm for 50 s and baked in the oven at 95 °C for 45 minutes.

3. The ABM mask aligner is turned on and the intensity of the UV light is monitored to be accurate.

4. The chips are then placed on the ABM mask aligner and held down by vacuum (one at a time). The mask for Josephson junctions bottom and top leads is placed and held down by vacuum similarly.

5. The chip is aligned exactly under the bottom lead pattern and raised slowly until it almost touches the mask. Alignment can be performed by eye and aid of the microscope is usually unnecessary at this point.

6. The chip is then raised up to touch the mask and press onto it. Optical fringes appear and start moving on the chip when observed at an angle. The chip is raised until the fringes stop moving. This is when the contact is optimal.

7. The chip is exposed to UV light through the mask for 3.5 seconds. Once all chips are exposed they are then removed from the mask aligner along with the mask and the UV lamp is turned off.

8. The samples are then developed in Developer 352 for 45 seconds followed by a rinse in water and blow drying. The bottom lead pattern is verified under the microscope to make sure the process went as expected.

9. The chips are then placed in the plasma etcher at 100 W for 120 seconds. The samples are now ready for material deposition.

10. Steps 5-16 for thin-film deposition are then followed. A Nb/Al multilayer that acts as the superconducting bottom lead is deposited during this run.

11. The samples are then transferred into test tubes filled with PG remover in the clean-room. The test-tubes are placed on the hotplate at 110 °C until the layers start to peel around the bottom lead pattern.

12. After the layers have peeled off, the test tubes are placed in a gentle sonicator for few minutes until only the bottom lead patterns are left. The chips are then rinsed in IPA and water followed by blow drying.

13. Then bottom lead patterns are imaged under the microscope and verified to have lifted off properly.

14. Steps 2-5 for the array fabrication process are followed with minor differences. Instead of the program for arrays, single pillars are written at 6 different spots in the center of the bottom lead pattern. There is no scratch made by hand, instead, the alignment markers in the bottom lead pattern are used to write the pillars at the desired location.

15. Steps 6-9 for array fabrication process are followed with some differences. Masks are used in the sample holders to mill only the area surrounding the junctions. After the milling is complete and the pillars have formed, we turn on the SiO_x thermal deposition. After checking the rates, 50 nm of SiO_x is deposited on the chips. The samples are then removed from the chamber.

16. The chips are then inserted in the side mill holders and placed back in the small chamber. The milling process is repeated, however this time we only mill each chip for 2+2 minutes at a rate of roughly 9 Å/s. The sample holders are then removed, the samples are flipped vertically and the process is repeated.

17. The samples are then taken back into the cleanroom and the junctions are imaged with the optical microscope.

18. The samples are then placed in PG remover on a hotplate at 110 °C for about 20 minutes for lift-off. To aid this process, the junction area is scrubbed with a Q-tip. They are then rinsed in IPA and water and blow dried. The samples are then imaged with the microscope and compared with previous images to confirm the lift-off.

19. The chips are then placed in a Plasma Etcher in vacuum. Plasma is then turned on in the presence of oxygen at 300 W for 300 s to clean the chip thoroughly.

20. Steps 2-13 of Josephson junction fabrication process are repeated for the top leads with some differences. We do not use LOR for the top leads. The top lead pattern on the mask is used. The alignment process requires the use of microscope and vernier scales on the chip and the mask to carefully align the top lead position. The exposure time is 8 seconds instead of 3.5 seconds. Before the development of the top lead stencil, the chips are dipped in Chlorobenzene for 5 minutes. Before the deposition of the top Nb/Au layer, 5 nm of Au is milled first using the ion mill gun in the sputter chamber.

21. After the liftoff process, the chips are imaged for checking any discontinuity in the leads and general damage. The samples are now ready for measurement and are placed inside glass vials and labeled appropriately.

3.6 Measurement process for Josephson junctions

The measurement process for Josephson junctions is detailed below:

1. Indium blobs are pressed on the sample leads of the chips. The samples are then placed on the sample stage of the Quick Dipper, and tied down with the help of thread.

2. The $I - V$ connecting wires are then fixed to the sample leads with the help of more indium blobs. Once they are firmly in place, the sample resistance is checked to be in the appropriate range.

3. The Quick Dipper is then lowered into a Dewar containing liquid helium slowly to avoid sudden boil-off.

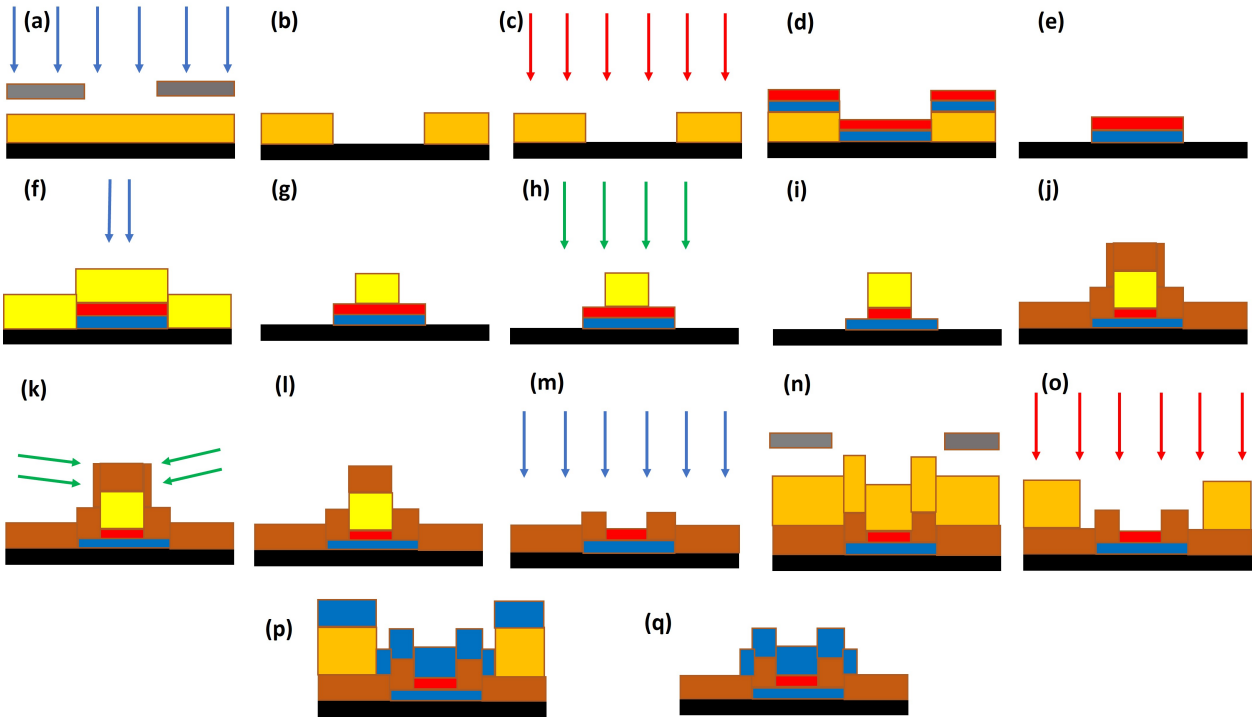

Figure 3.9: **Cross-sectional view of the Josephson junction fabrication process.** Si substrate is shown in black, photomasks are shown in grey, S1813-G2 photoresist is shown in orange, Nb superconductor is shown as blue, ferromagnetic and other metallic layers are shown in red, ma-N 2401 e-beam resist is shown in yellow, SiO_x is shown in brown, blue arrows represent UV light in step (a) & (m) and e-beam in step (f), red arrows represent material deposition and green arrows represent material removal. (a) shows the bottom lead lithography (b) shows the formation of the bottom lead stencil, (c) & (d) show material deposition via sputtering, (e) shows bottom leads after the etching process, (f) shows e-beam lithography process, (g) shows formation of the pillar geometry, (h) & (i) show the ion milling process, (j) shows SiO_x deposition, (k) shows side milling, (l) shows the pillar after side milling and before lift-off (m) shows the lift-off process for e-beam resist and (n)-(q) show the formation of the top lead, similar to bottom lead formation in (a)-(e).

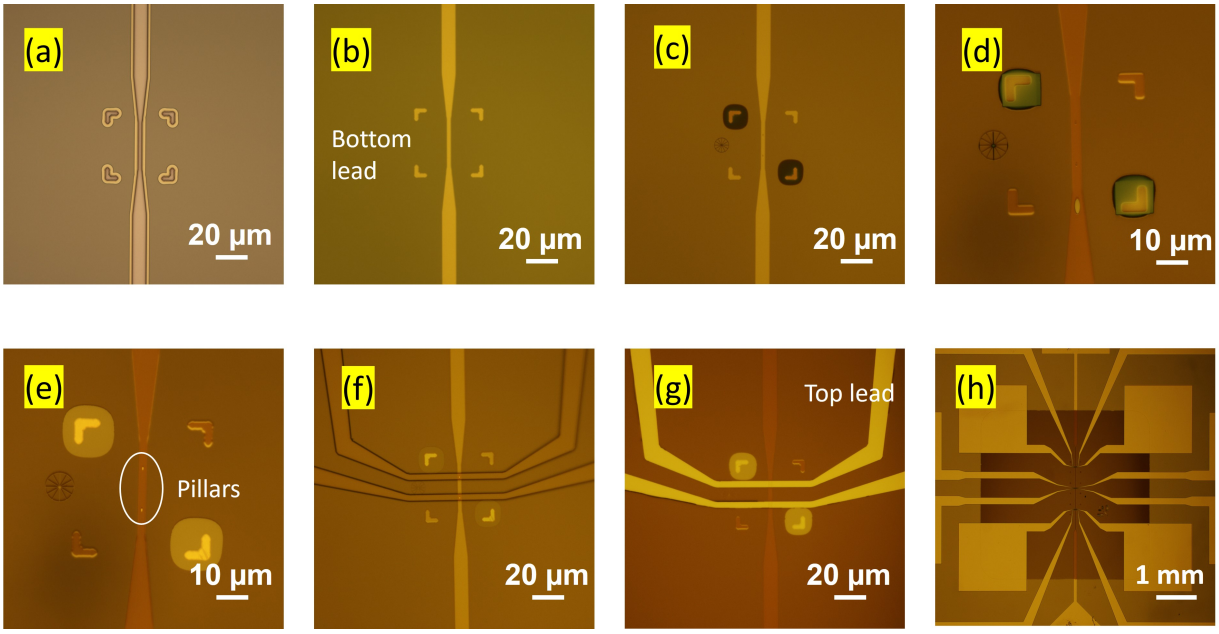

Figure 3.10: **Top view of the Josephson junctions during the fabrication process.** The images were taken using an optical microscope and are shown with scale bars are the bottom. (a) shows the bottom lead lithography (b) shows the deposited bottom lead layer, (c) shows e-beam pillar lithography (pillars not visible due to small size and lower magnification), (d) shows the chip after the ion milling and SiO_x deposition, (e) shows the pillars after lift-off (two pillars visible at the center), (f) shows the top lead lithography, (g) shows the top leads after deposition and (h) shows most of the chip and all lead connections at a low magnification.

4. The Dewar is then placed near the measurement station and the Quick Dipper is connected to all the electronics discussed earlier.

5. A test run is performed at 0 field to find the resistance and measure a typical $I - V$ curve. If the junction has a bad resistance or short, the measurement is aborted and a different pillar is checked.

6. Some samples are first run at a very high field to initialize the magnetic state of the junction.

7. The $I - V$ curves are then measured for fields in downsweep and upsweep.

8. Two junctions on each chip are measured. If using QD-I, this involves removing the dipper from the Dewar and reconnecting a different pillar. For QD-IV, this involves switching to a different pair of wires already connected to the necessary leads.

9. The Quick Dipper is then slowly removed from the Dewar while heating it with a blow drier to remove any condensation.

Chapter 4

Synthetic Antiferromagnets

In this chapter we will give a brief introduction to synthetic antiferromagnets (SAFs) and spin-valves. We will then discuss the magnetic properties of SAFs and the transport properties of ferromagnetic Josephson junctions containing these SAFs. The motivation behind this work is to explore the viability of replacing the fixed Ni layer in the spin-valve structure of the JMRAM. As discussed earlier, the current JMRAM design has certain magnetic problems with the fixed Ni layer. Ni is relatively good at carrying supercurrent for a ferromagnet, but has multi-domain magnetic structure and hence can interfere with the switching of the NiFe free layer. Since the magnetic switching properties of Ni improve with increasing thickness (see Appendix B), one possible solution is to replace the thin Ni layer with a thicker layer. However, this would displace the position of the device in the $0-\pi$ valley and affect the controllable switching of the phase. What we want to do instead is to somehow have thicker and magnetically better-behaved Ni layers without changing the location of the position of the device in the $0-\pi$ valley. One way to do that is by replacing Ni with a Ni-based synthetic antiferromagnet. To act as a fixed layer, this synthetic antiferromagnet will have to be unbalanced i.e. one of the layers is thicker than the other and the difference in thickness of these two layers is the same as the original Ni fixed layer. We will explain the reason behind this choice of replacement in the next section and the physics making such a replacement possible in Josephson junctions in a later section where we present our transport results.

First we studied balanced (both Ni layers with same thickness) Ni/Ag/Ni blanket films for this purpose but were unable to get a antiferromagnetic coupling with the deposition technique we have. (We discuss our results in the Appendix A.) Therefore we studied balanced Ni/Ru/Ni blanket films next. Since we found antiferromagnetic coupling in these systems, we studied the transport properties of Josephson junctions with balanced Ni/Ru/Ni synthetic antiferromagnets. The transport properties were in a viable range, so we studied the magnetic properties of unbalanced Ni/Ru/Ni blanket films next. We also studied the magnetic properties of spin-valves with unbalanced Ni/Ru/Ni as fixed layer and NiFe as free layer in both blanket films and elliptical arrays. We saw improvement in magnetic switching properties in some cases and in others we saw them worsen. Because of the ambiguity we did not proceed with the transport study of Josephson junctions of these layers during the course of the study.

The important results from the balanced Ni/Ru/Ni SAF study were published in [26].

4.1 Introduction

4.1.1 Synthetic antiferromagnets

Synthetic antiferromagnets are artificial antiferromagnets that consist of two or more thin ferromagnetic layers separated by a non-magnetic layer. Coupling of the ferromagnetic layers results in antiparallel alignment of the magnetization of the ferromagnets. This coupling is due to Ruderman–Kittel–Kasuya–Yosida (RKKY) interaction [83–85]. The coupling takes place via the nuclear magnetic moments or the localized inner d- or f-shell electron spins in a metal and involves an interaction mediated by the conduction electrons. RKKY was originally for dilute magnetic impurities in metals but it is also useful in the context of the

giant magnetoresistance (GMR) effect. GMR was discovered when the coupling between thin layers of magnetic materials separated by a non-magnetic spacer material was found to oscillate between ferromagnetic and antiferromagnetic as a function of the distance between the layers [86].

Let's consider the case of two ferromagnetic (F) layers with a coupling layer, as shown in Fig. 4.1. For a particular thickness of the coupling layer, the coupling between the F layers is antiparallel. If the thicknesses of both ferromagnetic layers are equal to each other, then it is known as a balanced SAF. If the thickness of one of the F layers, d_1 is larger than the other, d_2, then it is known as an unbalanced SAF.

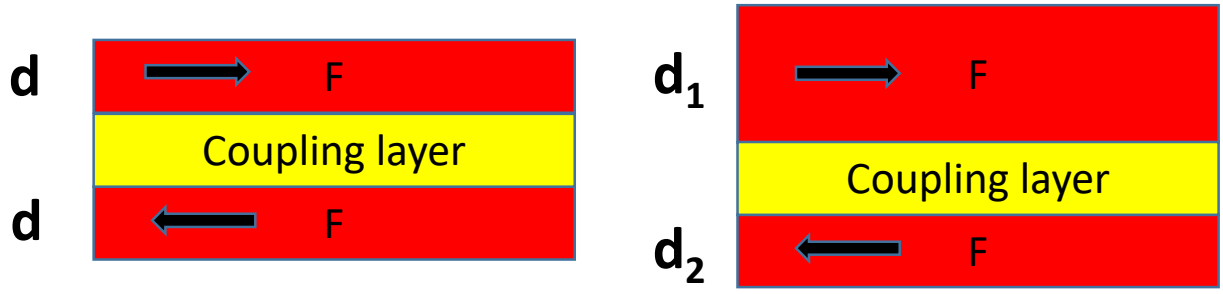

Figure 4.1: **Cartoon representation of synthetic antiferromagnets (SAFs).** Balanced SAFs are shown on the left panel and unbalanced SAFs are shown on the right panel. Red layers represent ferromagnetic layers with black arrows representing their magnetic orientation. Yellow layers represent the coupling layer.

4.1.2 Spin-valves

Spin-valves are magnetic structures with two uncoupled ferromagnetic layers as shown in Fig. 4.2. One of the ferromagnetic layers F_1 is known as the fixed layer and the other F_2 is known as the free layer. The fixed layer is typically made of a magnetically harder material (for example, Ni) with a larger switching field whereas the free layer is magnetically softer (for example, NiFe) with a smaller switching field. The free layer can be switched between

parallel or antiparallel states with the application of a small field (or a current).

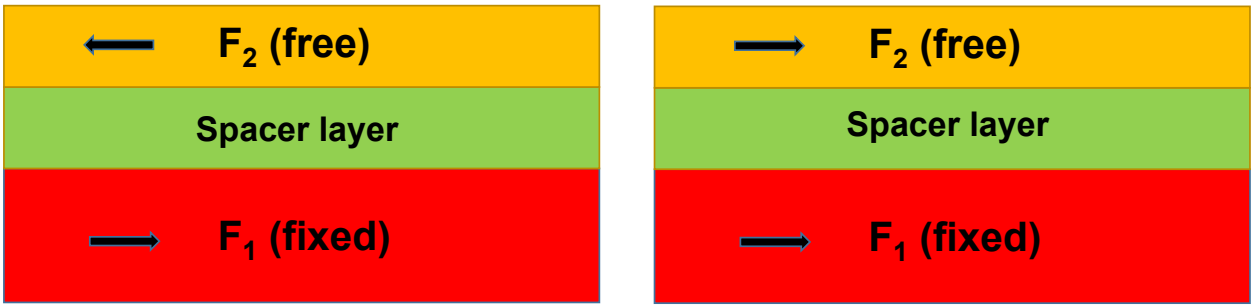

Figure 4.2: **Cartoon representation of a spin-valve.** The spin-valve is in antiparallel configuration in the left panel and parallel configuration in the right panel. The fixed ferromagnetic (F) layer is shown in red, the free F layer is shown in yellow and the spacer layer is shown in green. The black arrows represent the magnetic orientation of the ferromagnetic layers.

Spin-valves have a significant application in memory devices where the magnetic information can be stored in the overall orientation of both layers.

4.2 Balanced Ni/Ru/Ni system

4.2.1 Magnetic properties of blanket films

We deposited thin multi-layers of Nb(5)/Cu(2)/[Ni(2.0)/Ru(x)]$_3$/Ni(2.0)/Cu(2)/Nb(5) with x = 0.6-1.3 nm in steps of 0.1 nm. The samples were grown at a temperature of about -25 °C. The moment versus field measurements were performed using the MPMS3 at 5 K and the sample areas were measured using a smartphone camera and ImageJ software. The moment/area (m/area) vs field (H) curves for a subset of samples are shown in Fig 4.3.

The saturation m/area varies with the Ru thickness, d_{Ru} which might mean dead layers, bad centering or an error in the area measurement. However, the important result is that we see some samples with antiferromagnetic behavior in this set, as noticed by the lack of hysteresis and the m/area vs H curve passing very close to the origin. The saturation field H_{sat} (i.e. field at which the moment saturates) is a good indicator of the antiferromagnetic

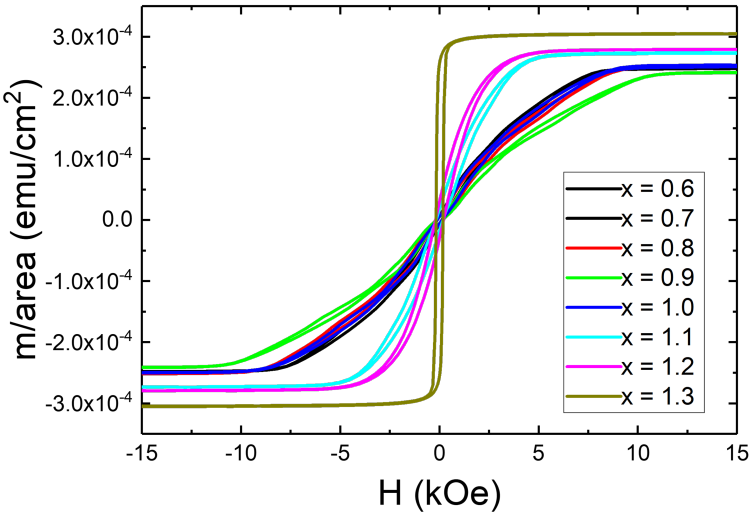

Figure 4.3: **m/area vs H for [Ni(2.0)/Ru(x)]$_3$/Ni(2.0).** The curves show a range of antiferromagnetic and ferromagnetic behavior depending on the Ru thickness.

coupling strength. The inverse of the slope of the m/area vs H curves is also a good indicator of the coupling strength. The 1/Slope was calculated by using 5 points around zero moment and fitting them to a straight line. Both H_{sat} and 1/Slope were extracted from the plots and plotted against the Ru thickness d_{Ru} in Fig. 4.4.

The H_{sat} and 1/Slope plots behave similarly to each other and the peak of the antiferromagnetic coupling is around $d_{\text{Ru}} = 0.9$ nm. The variation in coupling strength between ferromagnetic and antiferromagnetic samples is because of RKKY interaction.

Since the repeated Ni/Ru/Ni multilayers exhibited RKKY interaction, we studied single Ni/Ru/Ni layers next. We deposited Nb(5)/Cu(2)/Ni(2.0)/Ru(x)/Ni(2.0)/Cu(2)/Nb(5) which has only two Ni layers sandwiching a Ru layer. The Ru layer thickness x was varied from 0.6-1.3 nm in steps of 0.1 nm and 1.5-2.7 nm in steps of 0.2 nm. The moment versus field measurements were performed using the MPMS3 at 10 K and the sample areas were measured using a microscope for better accuracy. The moment was divided by the sample

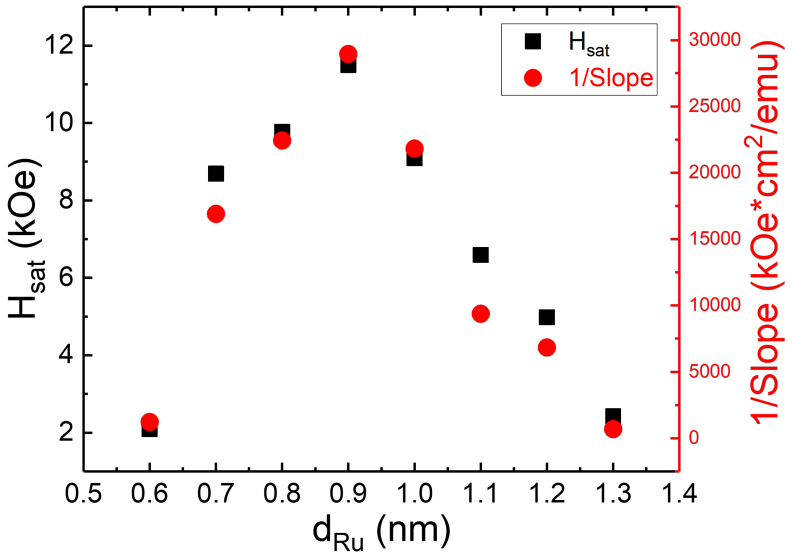

Figure 4.4: **H_{sat} and 1/Slope vs d_{Ru} for [Ni(2.0)/Ru(x)]$_3$/Ni(2.0).** H_{sat} is shown on the left axis with black squares and 1/Slope is shown on the right axis with red circles. Both plots have peaks at $d_{Ru} = 0.9$ nm.

area and the total nominal thickness of the Ni layers to obtain the magnetization M. The M vs H curves for a subset of samples are shown in Fig 4.5.

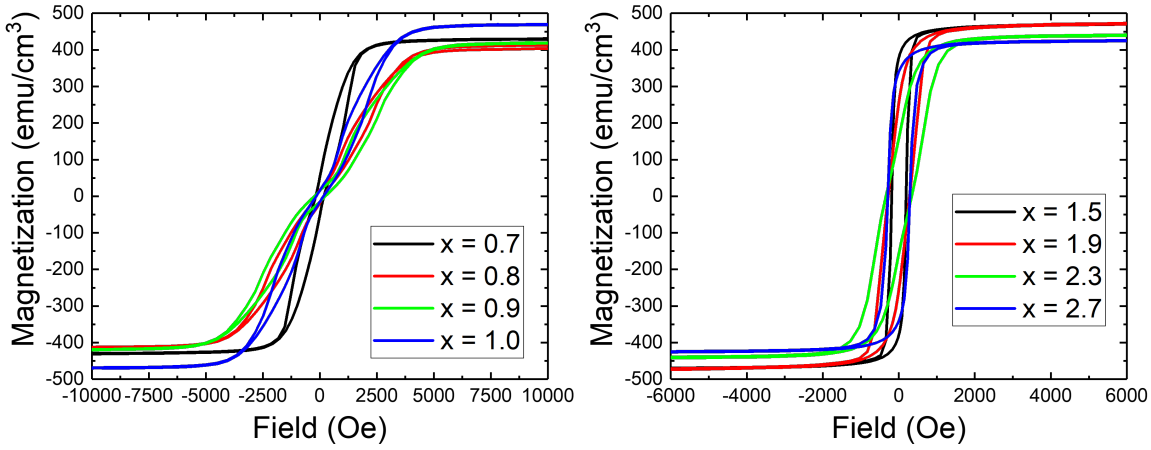

Figure 4.5: **Magnetization vs field for Ni(2.0)/Ru(x)/Ni(2.0).** The curves oscillate between ferromagnetic and antiferromagnetic behavior with Ru thickness.

In Fig. 4.5 we see a similar variation from ferromagnetic to antiferromagnetic behavior

as was previously seen in Fig. 4.3. The change in slope at low fields in the 0.9 nm data may be an indication of spin-flop behavior occurring in regions of the sample where the magnetocrystalline anisotropy favors alignment with the external field. We ignore that region of the data and estimate the saturation field by extrapolating the approximately linear dependence at higher fields to the saturation value. 1/Slope was calculated by using 5 points around zero moment and fitting them to a straight line. H_{sat} and 1/Slope are plotted against the Ru thickness, d_{Ru}, in Fig. 4.6.

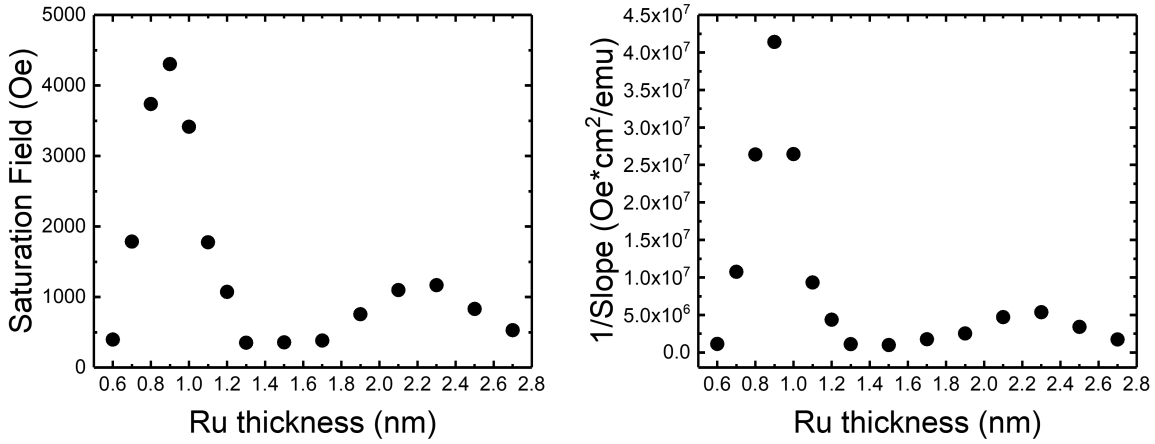

Figure 4.6: **Saturation field and 1/Slope vs Ru thickness for Ni(2.0)/Ru(x)/Ni(2.0).** Both plots have their first peaks at $d_{\mathrm{Ru}} = 0.9$ nm.

The plots look similar, as expected and the peak of the antiferromagnetic coupling is again seen around $d_{\mathrm{Ru}} = 0.9$ nm. Because of the larger thickness range explored in this sample set, we also observe a second peak in the antiferromagnetic coupling at $d_{\mathrm{Ru}} = 2.3$ nm. The coupling strength, J_1 can be obtained from the saturation field using the formula [87]:

$$J_1 = \frac{\mu_0 H_{\mathrm{sat}} M_{\mathrm{sat}} d_F}{2}. \tag{4.1}$$

We calculate J_1 to be 0.18 and 0.052 erg/cm^2 for the first and second peaks, respectively. The

coupling strength at the first peak is much weaker than in Co/Ru/Co SAFs but comparable to that in Co/Cu/Co SAFs [86]. We also studied the properties of Ni(2.0)/Ru(2.3)/Ni(2.0) with varying temperature and compared them to that of Ni(4.0). We discuss these results in Appendix C.

The next thing we studied is if this RKKY coupling holds true for thicker Ni layers. We deposited Nb(5)/Cu(2)/Ni(4.0)/Ru(y)/Ni(4.0)/Cu(2)/Nb(5) where y = 0.6–1.3 nm in steps of 0.1 nm. The magnetization versus field measurements at 10 K for a subset of the samples are shown in Fig 4.7.

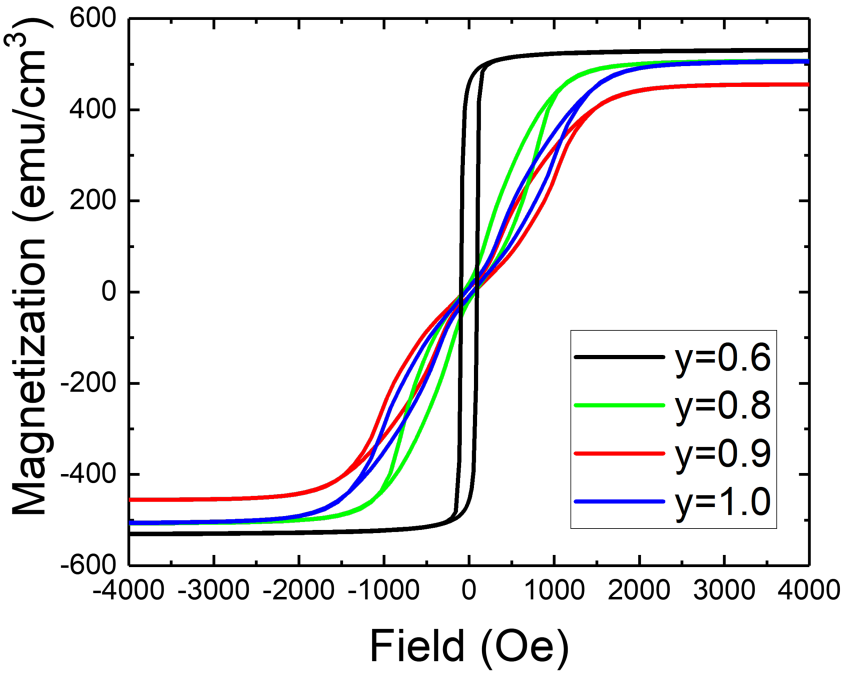

Figure 4.7: **Magnetization vs field for Ni(4.0)/Ru(y)/Ni(4.0).** The curves show a range of ferromagnetic and antiferromagnetic behavior with Ru thickness.

The coupling for this Ni thickness behaves similarly to the ones discussed earlier. Both H_{sat} and 1/Slope were extracted from the M vs H curves and plotted against the Ru thickness in Fig 4.8. We see a similar variation as before with a peak at 0.9 nm, but the

data exhibit larger scatter.

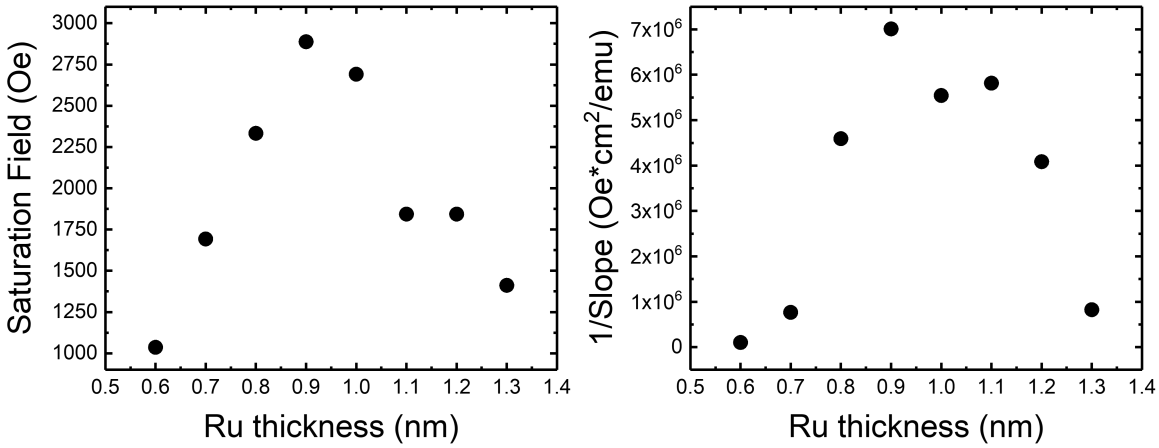

Figure 4.8: **Saturation field and 1/Slope vs Ru thickness for Ni(4.0)/Ru(y)/Ni(4.0).** Both curves have peaks at y = 0.9 nm.

Since our eventual goal was to create Josephson junction devices with these Ni SAFs and study the behavior with varying Ni thickness, we deposited and studied the magnetic behavior of Nb(5)/Cu(2)/Ni(x)/Ru(0.9)/Ni(x)/Cu(2)/Nb(5) blanket films where x = 0.8-4.0 nm in steps of 0.4 nm. We chose the Ru thickness to be 0.9 nm to get the strongest antiferromagnetic coupling. The magnetization versus field measurements at 10 K are shown for a subset of samples in Fig 4.9.

There are several things to note. All samples exhibited strong antiferromagnetic coupling except the ones with 0.8 and 1.2 nm of Ni respectively (not shown in the figure). The 0.8 nm sample was ferromagnetic indicating that the coupling does not work for very thin layers of Ni. The 1.2 nm sample showed antiferromagnetic coupling, but also showed some hysteresis at low field indicating that the coupling strength decreases below a certain Ni thickness. To characterize these samples further we plotted H_{sat} and M_{sat} of these samples vs total Ni thickness $2d_{\mathrm{Ni}}$ as shown in Fig. 4.10. The uncertainties in H_{sat} were attributed to the field step size where the point lies and that for M_{sat} were estimated to be 5% from the area

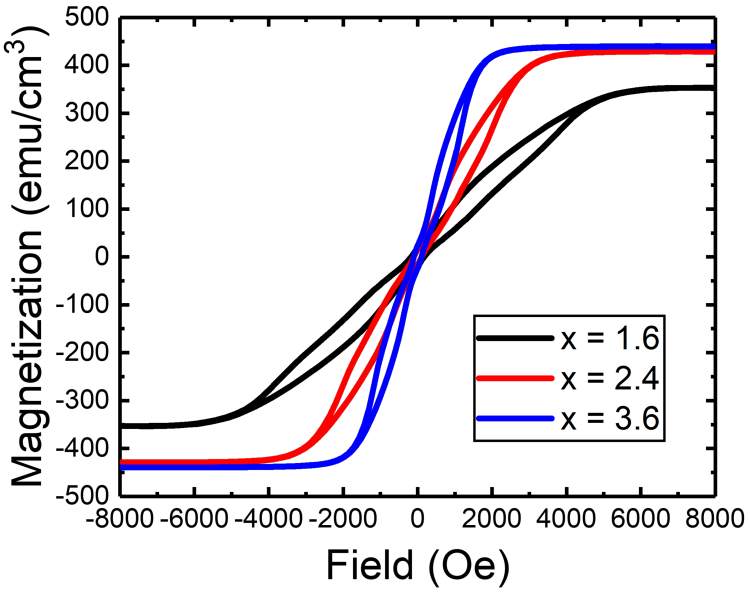

Figure 4.9: **Magnetization vs field for Ni(x)/Ru(0.9)/Ni(x).** All shown curves exhibit antiferromagnetic behavior.

measurement.

The H_{sat} falls as $1/2d_{\text{Ni}}$, as expected. M_{sat} stabilizes around 450 kA/m for the thick samples; this value is close to the bulk value for Ni of 510 kA/m at low temperature [88]. The decrease in M_{sat} for the thinner samples is attributed to magnetically dead layers at the Ni/Ru and Ni/Cu interfaces. To obtain the dead layer thickness, we plot the saturation moment per area versus the total Ni thickness in Fig. 4.11.

The total magnetic dead layer thickness of the SAFs arising from the two Ni/Cu and two Ni/Ru interfaces obtained from the x-intercept of linear fit is 1.24 $\pm$ 0.07 nm. The slope of this fit provides an estimate of the saturation magnetization of Ni, $M_{\text{Ni}} = 554 \pm 15$ kA/m. This value is a bit higher than bulk, but we should not take this value too seriously because the straight-line fit assumes that the dead layer thickness is constant in all the samples.

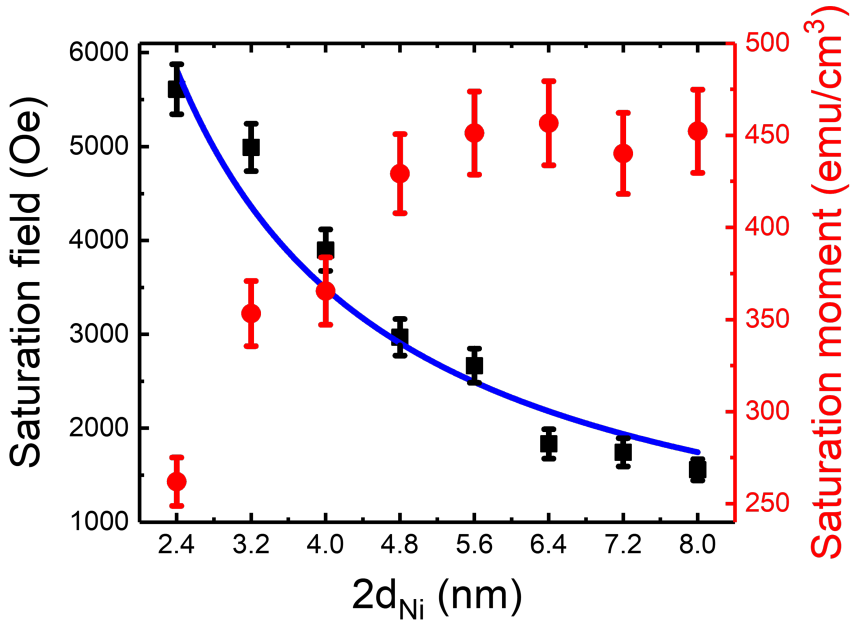

Figure 4.10: **Saturation field and moment vs $2d_{Ni}$ for Ni(d_{Ni})/Ru(0.9)/Ni(d_{Ni}).** The solid blue line is the fit of H_{sat} (black squares) to c/$2d_{Ni}$ where c is a constant. The error bars in H_{sat} represent the uncertainty due to the field steps and the error bars in M_{sat} (red circles) represent the 5% uncertainty in the area measurement.

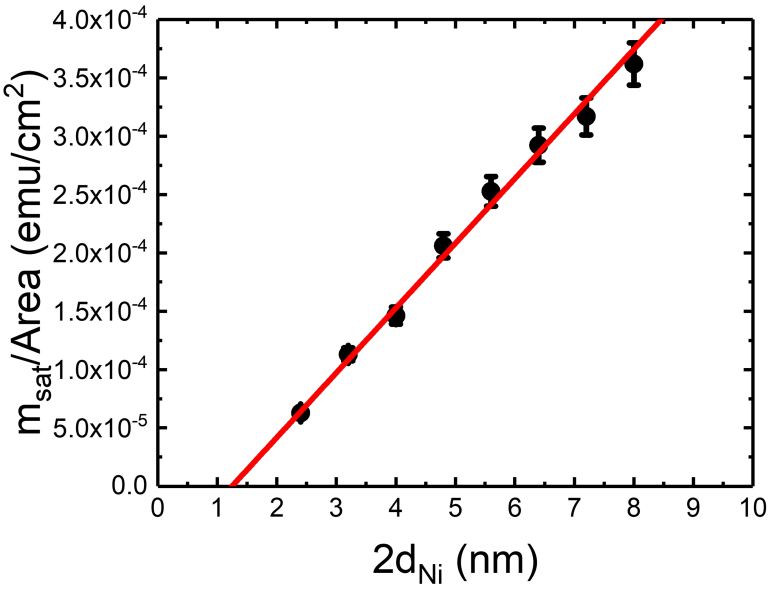

Figure 4.11: **m_{sat}/area vs $2d_{Ni}$ for Ni(d_{Ni})/Ru(0.9)/Ni(d_{Ni}).** The red curve is a linear fit of the experimental data in black circles. The error bars represent the uncertainty in the area measurement which is estimated to be 5%.

4.2.2 Transport in Josephson junctions

Josephson junctions were fabricated using the methods outlined in Chapter 3. The bottom lead deposition consisted of $[\mathrm{Nb}(25)/\mathrm{Al}(2.4)]_3/\mathrm{Nb}(20)/\mathrm{Cu}(2)/\mathrm{Ni}(d_{\mathrm{Ni}})/\mathrm{Ru}(0.9)/\mathrm{Ni}(d_{\mathrm{Ni}})$ /Cu(2)/Nb(5)/Au(10) where d_{Ni} was varied from 1-3 nm in steps of 0.2 nm. After formation of elliptical pillars with lateral dimensions of 1.25 µm × 0.5 µm, 5 nm of Au was milled and then the top lead consisting of Nb(160)/Au(10) was deposited. Transport measurements were performed at 4.2 K inside a liquid helium dewar using a sample probe equipped with a superconducting magnet. $I-V$ curves were measured in fields up to 100 mT in both directions. The $I-V$ curves were then fit to the RSJ model (Eqn. 2.19) discussed previously to extract the values of critical current I_c. The dependence of I_c on the magnetic field H for a typical sample is plotted in Fig. 4.12 and fit to the Airy function (Eqn. 2.48) for the case without an internal magnetization, discussed previously.

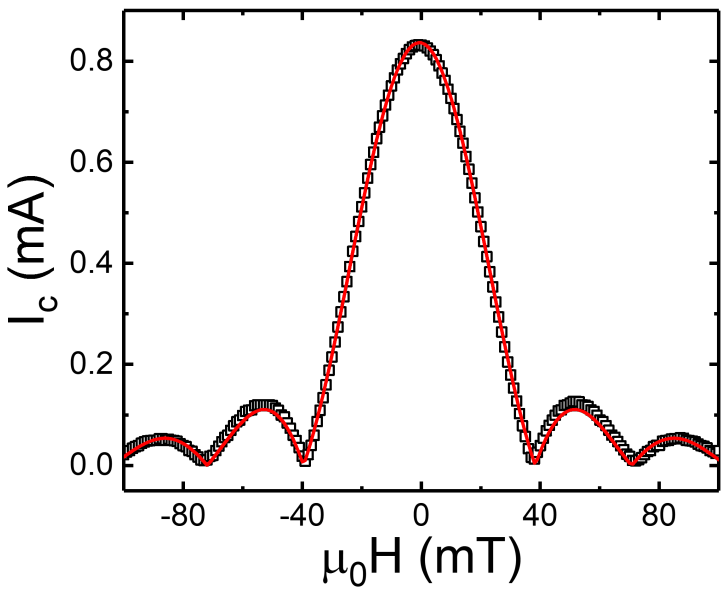

Figure 4.12: **I_c vs H for a typical Ni(d_{Ni})/Ru(0.9)/Ni(d_{Ni}) Josephson junction.** The experimental data are shown in black squares. The red curve shows a fit to Eqn. 2.48.

The Airy pattern is well centered at zero field and doesn't have any visible hysteresis for almost all of the junctions measured (only one sweep direction is shown in the Fig. 4.12). This implies that the junctions have nearly zero remanent magnetization because of strong antiferromagnetic coupling. The magnetic measurements in the previous section show a hysteresis, but those measurements are performed at very high fields. For a low field range, the hysteresis is negligible. We discuss more on this in Appendix D.

We multiply the maximum I_c value (obtained from the Airy fit) by the normal state resistance R_N to obtain I_cR_N. This product is independent of the junction area. Figure 4.13 shows a plot of I_cR_N versus the total Ni thickness $2d_{\mathrm{Ni}}$. Two junctions at each thickness were measured to factor for variations in thickness and interface quality during the sputtering process. The junction-to-junction variation in I_cR_N is typical for Josephson junctions containing thin layers of strong ferromagnetic materials [22]. The data for the thinnest junctions (at $d_{\mathrm{Ni}} = 1.0$ nm) are anomalously high compared to the rest of the data. The exact reason is unknown but it may be related to the observations of ferromagnetic behaviour of thin film samples with Ni thickness below 1.2 nm.

As seen in the figure, I_cR_N decays slowly with Ni thickness. The data are fit to an exponential function,

$$I_cR_N = V_0 e^{\frac{-2d_{\mathrm{Ni}}}{\xi_{\mathrm{Ni}}}} \tag{4.2}$$

The equation follows the data closely if we ignore the first points at 2 nm and the decay length ξ_{Ni} was found to be 7.5 $\pm$ 0.8 nm in that case. If we include those data points, the decay length reduces to 5.3 $\pm$ 0.6 nm, but the curve does not fit the data well. For simple S/F/S Josephson junctions (without a SAF) I_cR_N oscillates and decays algebraically with F-layer thickness for ballistic transport [66] or oscillates and decays exponentially for diffusive

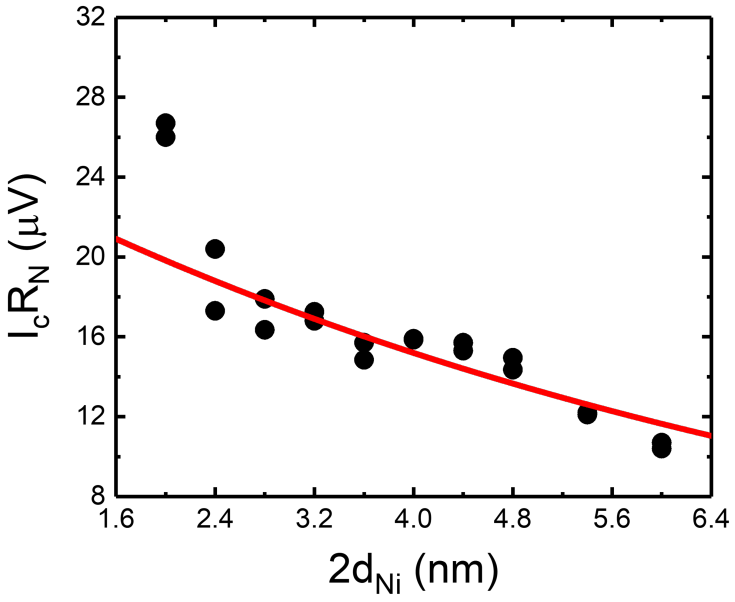

Figure 4.13: **I_cR_N vs $2d_{Ni}$ for Ni(d_{Ni})/Ru(0.9)/Ni(d_{Ni}) Josephson junctions.** The experimental data are shown in black circles and the red curve showing an exponential decay is a fit to Eqn. 4.2 (excluding points at 2 nm).

transport [74]. When the F layer is replaced by a SAF, this oscillation is not observed due to cancellation of the electron pair phase accumulations in the two opposing F layers of the SAF [89–92]. In the ballistic limit when there is no bulk or interface scattering, it is predicted that there is no decay of I_c with SAF thickness, and the I_c values should be similar to those in S/N/S junctions [89]. In the presence of disorder, an exponential decay [92] is predicted. Ness *et al.* calculated the supercurrent through Nb/Ni/Nb Josephson junctions using a realistic band model for Ni and a combination of density functional theory and Bogoliubov-de-Gennes theory [79]. They found that the supercurrent oscillates and decays exponentially with a decay constant $\xi_{\mathrm{Ni}} = 4.1$ nm. In our junctions which contain disorder, the measured decay length is longer than the value calculated by Ness *et al.* for ideal junctions that contain no disorder. That result is not predicted by the standard theories in the diffusive limit [89, 91]. We had always assumed that the transport in our junctions was

diffusive rather than ballistic because of the presence of multiple interfaces and disorder, but the data suggest that that the transport could be partially ballistic through crystal columns. Previous studies on multilayers deposited in our sputtering system show columnar growth often with epitaxy between the different materials within a single column or grain [93].

Josephson junctions containing Ni have also been studied experimentally [80,94,95]. Baek *et al.* observed a maximum π-state I_cR_N value of about 80 μV with transitions between the 0 and π-state at Ni thicknesses of about 0.8 and 3.4 nm. The maximum value of I_cR_N in Fig. 4.13 is somewhat smaller, probably because of spin memory loss [96] and poor band matching between the Ni/Ru/Ni SAF layers (by poor band matching we mean that a majority band electron in the first Ni layer becomes a minority band electron in the second layer).

In conclusion, our balanced Ni/Ru/Ni SAF Josephson junctions showed excellent magnetic properties and relatively good supercurrent transmission. Although I_c values are about a third of what we would expect for plain Ni, the long decay constant makes thicker unbalanced Ni/Ru/Ni SAF junctions a prospective replacement for the thin Ni fixed layer currently used in the spin-valve Josephson junctions in Northrop Grumman's JMRAM [33].

4.3 Unbalanced Ni/Ru/Ni system

4.3.1 Unbalanced Ni/Ru/Ni blanket films

Since the study on balanced Ni/Ru/Ni systems gave us favorable results, we studied the magnetic properties of unbalanced Ni/Ru/Ni blanket films next. We deposited two sets of samples: Nb(5)/Cu(2)/Ni(3.0)/Ru(0.9)/Ni(x)/Cu(2)/Nb(5) where x = 1.2, 1.6, 2.0 and 2.4 nm, and Nb(5)/Cu(2)/Ni(4.0)/Ru(0.9)/Ni(x)/Cu(2)/Nb(5) where x = 1.2-3.2 nm in steps of 0.4 nm. The moment versus field measurements were performed in SQUID-VSM mode at

10 K and the sample areas were measured using ImageJ. The moment was divided with the sample area and total Ni layer thickness to obtain the magnetization i.e. moment/volume. The moment/volume versus field curves for both sample sets are shown in Fig. 4.14.

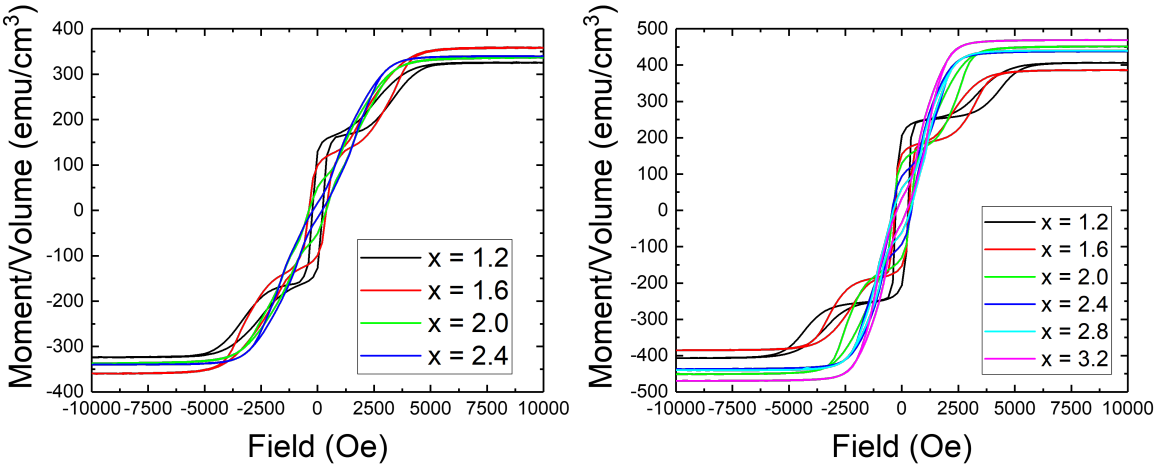

Figure 4.14: **M vs H for Ni(3.0)/Ru(0.9)/Ni(x) and Ni(4.0)/Ru(0.9)/Ni(x).** Because of the unbalanced nature of these samples, they switch in phases.

The samples have distinct but expected M vs H curves. All the samples have similar moments/volume (with small deviations) indicating that most of the Ni is magnetically active and without dead layers. Each curve has 3 distinct loops. The sharp central loop is similar to the hysteresis seen in a normal magnet, since this is where the thicker Ni layer switches in the direction of the applied magnetic field with the thinner layer in anti-parallel orientation. The top and bottom loops are more rounded and represent the slow rotation of the thinner Ni layer to align parallel to the thicker Ni layer at saturation fields. As we can see, the overall curve is sharper for a larger thickness difference between the two Ni layers, i.e. the Ni(3.0) set is more sloped than the Ni(4.0) set.

4.3.2 Spin valve arrays with unbalanced Ni/Ru/Ni SAFs and NiFe

Since the unbalanced SAFs behaved as expected, we studied them as a fixed magnetic layer in a spin-valve structure. We discussed spin-valves and the motivation behind replacing the Ni fixed layer in JMRAM by unbalanced Ni/Ru/Ni SAFs earlier in this chapter. We fabricated pillar arrays with the structure $[Nb(25)/Al(2.4)]_3/Nb(20)/Cu(2)/NiFe(1.3)/Cu(4)/FL/Cu(2)/Nb(5)/Au(10)$, where the FL stands for fixed layer and is either Ni(1.6) or 4 different sets of Ni SAFs with 1.6 nm of absolute difference in the thickness of the two Ni layers. These thicknesses of NiFe and effective Ni were chosen carefully because of past experiments where phase control in Josephson junctions with these spin-valve structures was demonstrated [97]. We chose the thick Nb/Al base to make these structures as close to the actual junctions as possible. NiFe was chosen as the free layer because it is used as the free layer in JMRAM and is a soft, easily switchable magnet. The Cu(4) layer in the middle was used to magnetically separate the fixed and the free layer.

Since the arrays have the same sample area by design, we can directly compare the moment versus field curves of these samples at 10 K. We first measured the major loop: these curves have a big enough field range ($\pm$10000 Oe) to perform a complete reversal of the magnetization of both the free and fixed layer. We then measured the minor loop: the sample is first saturated at a high field, and then only the reversal of the free layer is performed at a low field range (130 to -170 Oe). The M vs H curves for both the major and minor loops are shown in Fig. 4.15.

The major loops for these spin valve structures look very similar to the M vs H curves for unbalanced Ni/Ru/Ni SAFs discussed earlier, except for low fields around 0 Oe. This is because the NiFe free layer switches completely at low fields, so the rest of the curve is

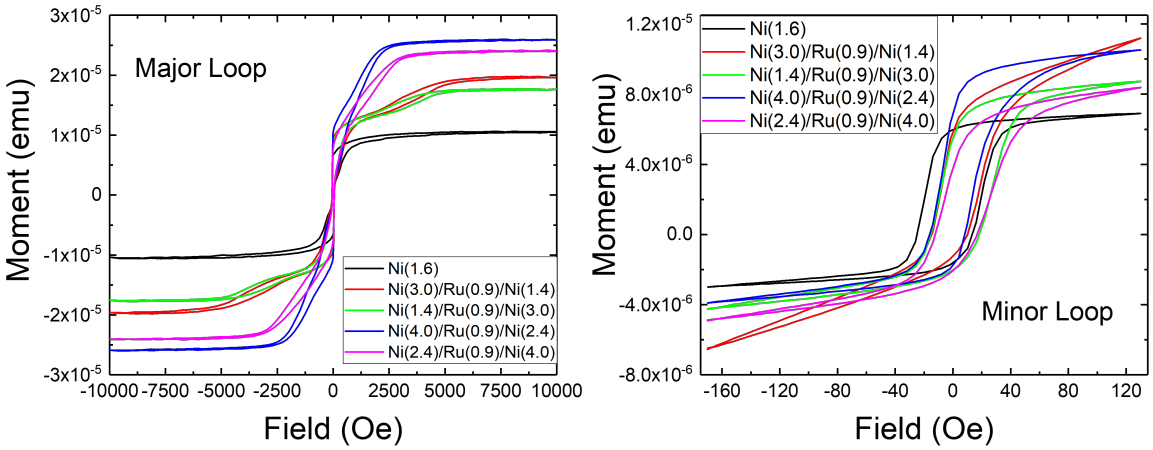

Figure 4.15: **Moment vs field for NiFe(1.3)/Cu(4)/FL arrays.** The left panel shows the major loops whereas the right panel shows the minor loops.

driven by the reversal in the unbalanced Ni/Ru/Ni SAF. The minor loops looks similar to the M vs H curves for NiFe, however they are somewhat rounder and do not seem to fully saturate at the closing, probably because of the multi-domain nature of Ni. We were hoping to avoid this behavior in the unbalanced Ni SAF systems, however it seems like the this was not the case. More significantly, in most of the unbalanced SAF systems, we see a lower coercivity in the minor loops than the plain Ni control samples, which indicates that this unwanted influence is reduced.

We repeated the above experiment for a different effective Ni thickness of 1.2 nm and NiFe thickness of 1.6 nm. The thicknesses were chosen for the same reasons stated above. The M vs H curves are shown in Fig. 4.16,

We saw similar results for this pair of Ni and NiFe thicknesses. The Ni(3.0)/Ru(0.9)/Ni(1.8) sample had a much lower coercivity than other samples and shows promise for future use.

We also studied the effect of thicker Ni layers in the unbalanced SAFs, and the influence of deposition rate on the fixed and free later switching. However, for those samples we did not

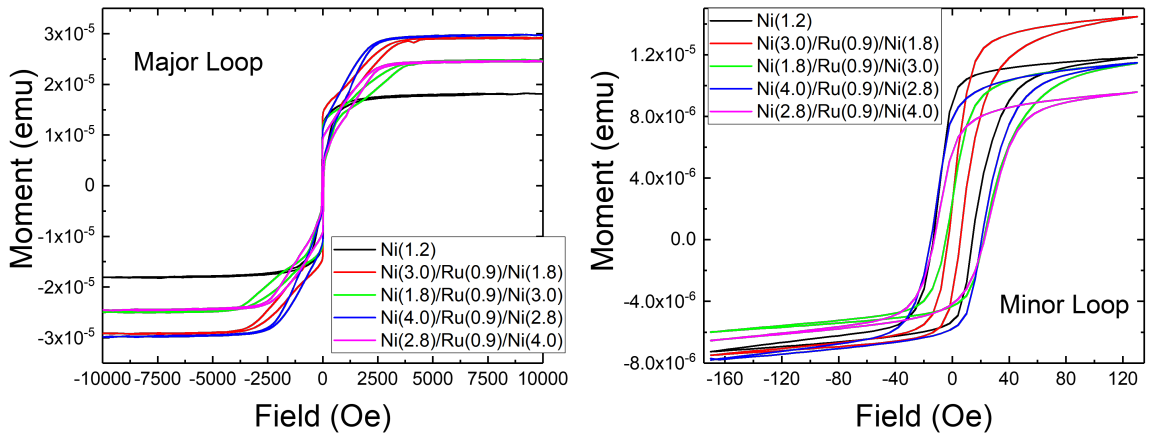

Figure 4.16: **Moment vs field for NiFe(1.6)/Cu(4)/FL arrays.** The left panel shows the major loops whereas the right panel shows the minor loops.

find a clear advantage of the unbalanced Ni SAF over Ni. We do not show these ambiguous results to avoid confusion.

4.4 Conclusions

We studied Ni/Ru/Ni systems with the motivation of using unbalanced synthetic antiferromagnets as a replacement for the fixed Ni layer in JMRAM with potentially better magnetic properties. We studied the RKKY oscillation for balanced Ni(2.0)/Ru(x)/Ni(2.0) systems and found the first and second antiferromagnetic peaks at x = 0.9 and 2.3 nm, respectively. We also found that the antiferromagnetic coupling at Ru thickness of 0.9 nm holds true for thicker Ni layers. We then studied the transport properties of Josephson junctions with balanced Ni/Ru/Ni synthetic antiferromagnets and found that the decay of critical currents with thickness was very slow [26]. This interesting behavior may be due to phase cancellations in opposing magnetic layers. We also studied the magnetic properties of unbalanced Ni/Ru/Ni SAFs in blanket films and spin-valves containing unbalanced

Ni/Ru/Ni SAFs as fixed layer and NiFe as free layer in elliptical arrays. We saw improvement in magnetic switching properties in some cases compared to Ni which might be useful for their application as a replacement of Ni in JMRAM. Further magnetic study of films/arrays and transport study of Josephson junctions containing unbalanced Ni/Ru/Ni SAFs need to be performed to explore and establish the advantages of these systems over plain Ni.

Chapter 5

Role of interfaces in supercurrent transmission

In this chapter we discuss the role of interfaces in supercurrent transmission through ferromagnetic Josephson junctions. The motivation behind this work is to improve the supercurrent transmission through the free NiFe layer in the JMRAM device. One simple way to increase I_c through ferromagnetic Josephson junctions is to increase the lateral area of the junctions. However, this can cause other problems; the magnetic layers can become multi-domained and their reliable switching can be affected. The ideal method is thus to increase the critical current density J_c through the same junction area.

Magnetic Josephson junctions in the JMRAM device contain Ni as the fixed layer and NiFe (Permalloy) as the free layer. NiFe is a soft magnet and and has sharp switching properties with low coercivity. But supercurrent transmission through NiFe is significantly lower compared to Ni [22,80,95]. J_c can be increased by switching to different ferromagnetic materials, however since the magnetic switching properties change with materials, this is not feasible. For our case, we wanted to retain the NiFe layer for its magnetic properties but somehow increase the supercurrent through the junction. To do this, we tried to improve the transport at the interface of the ferromagnet and the adjacent normal metal. Since there are no extensive theoretical studies for supercurrent transport through various interfaces, we looked at normal transport instead.

Supercurrent is an equilibrium property and involves the transfer of Cooper pairs. However, it can be influenced by the same bulk and interface properties as normal transport.

Because the supercurrent transport depends on spin properties, we focused on another spin-dependent transport phenomenon: Giant Magnetoresistance (GMR).

5.1 Interface transport properties in GMR

Giant magnetoresistance (GMR) is a quantum mechanical magnetoresistance effect. It is observed in multilayers composed of alternating ferromagnetic and non-magnetic conductive layers. For the case of Current-Perpendicular-to-Plane Magnetoresistance (CPP-MR), the transport through magnetic multilayers can be explained by using the simple two-current-series resistor model. For a N/F/N structure, this model states that the area×resistance value is uniquely determined by the thickness of the ferromagnet t_F, normal metal t_N and a set of parameters for the F & N metals and their interface (F/N) [98–100]. The scattering of electrons at the F/N interface can be described by two interface specific resistances: $AR^{\uparrow}_{F/N}$ and $AR^{\downarrow}_{F/N}$. $\uparrow$ and $\downarrow$ indicate the conduction electron parallel or anti-parallel to the F-layer moment, respectively. For analysis, it is often easier to use derived parameters: the dimensionless interface spin-scattering asymmetry $\gamma_{F/N}$ and twice the enhanced interface specific resistance $2AR^{*}_{F/N}$, where

$$\gamma_{F/N} = \frac{AR^{\downarrow}_{F/N} - AR^{\uparrow}_{F/N}}{AR^{\uparrow}_{F/N} + AR^{\downarrow}_{F/N}} \tag{5.1}$$

and

$$2AR^{*}_{F/N} = \frac{AR^{\uparrow}_{F/N} + AR^{\downarrow}_{F/N}}{2} \tag{5.2}$$

Higher values of $\gamma_{F/N}$ and $2AR^{*}_{F/N}$ indicate a larger asymmetry between the resistance for the two different spin directions, thus leading to a stronger GMR effect. However, one can

argue that this would be detrimental to supercurrent transmission at the interface. In conventional superconductors, the conduction takes place via spin-singlet Cooper pairs. Since the electron spins in the pair are anti-parallel to each other, ideally we would like equal (and low) resistance for electrons of both the spin directions at the interface for optimal conduction. A preferential conduction of one spin direction versus the other would be detrimental to the Cooper pair. Assuming this is true for our ferromagnetic Josephson junctions, we would like the F/N interfaces to have low values of $\gamma_{F/N}$ and $2AR^*_{F/N}$.

We know that the magnitude of critical current density J_c of a ferromagnetic Josephson junction depends on both the bulk properties of the ferromagnet and the interfaces between the materials in the stack. For example, we see a higher I_cR_N value for Ni junctions when compared to NiFe junctions [22, 80, 95]. Since our junctions contain 2 nm of Cu on each side of the ferromagnetic layer for better growth of layers, we looked at the $\gamma_{F/N}$ and $2AR^*_{F/N}$ values for the NiFe/Cu and Ni/Cu interface in the review paper by J. Bass [39]. We also looked for other normal metals that have lower values of $\gamma_{F/N}$ and $2AR^*_{F/N}$ than the NiFe/Cu interface and found Pd/NiFe to have lower values. The $\gamma_{F/N}$ and $2AR^*_{F/N}$ values for NiFe/Cu, Ni/Cu and NiFe/Pd interfaces are listed in Table 5.1: The values for

F/N Interface	NiFe/Cu	Ni/Cu	NiFe/Pd
$\gamma_{F/N}$	0.7	0.3	0.41
$2AR^*_{F/N}$ (fΩm^2)	1.0	0.36	0.4

Table 5.1: **GMR parameters for NiFe/Cu, Ni/Cu and NiFe/Pd interfaces.** The $\gamma_{F/N}$ and $2AR^*_{F/N}$ values for these interfaces were obtained from [39].

the Ni/Cu interface are certainly lower than the NiFe/Cu interface. One could argue that some of the enhancement of critical current density seen in Ni versus NiFe junctions could be because of these properties at the interface. What if we replaced the NiFe/Cu interfaces with

Ni/Cu interfaces by adding thin layers of Ni in-between the NiFe and Cu layers? Would we see an improvement in the critical current densities? Also, the values for NiFe/Pd interface are lower compared to NiFe/Cu interface. What if we replaced the Cu spacer layers with Pd in our junctions? Would we see a similar improvement? We explore these ideas in this chapter.

5.2 Cu/Ni/NiFe/Ni/Cu system

In this section, we study the magnetic properties of Cu/Ni/NiFe/Ni/Cu films and compare their magnetic properties with Cu/NiFe/Cu films. We then study the supercurrent transport properties of Josephson junctions containing these layers and perform a similar comparison. Important results of this work were published in [101].

5.2.1 Magnetic properties of blanket films

As discussed earlier, we wanted to add thin layers of Ni between Cu and NiFe, but we were unsure about what thickness to use for optimal magnetic behaviour. Therefore, we deposited three sets of samples: $[Nb(25)/Al(2.4)]_3$/Nb(20)/Cu(2)/F/Cu(2)/Nb(5) where F = Ni(0.2)/NiFe(x)/Ni(0.2) with x = 0.4-1.8 nm in steps of 0.2 nm, Ni(0.3)/NiFe(x)/Ni(0.3) with x = 0.6-2.0 nm in steps of 0.2 nm, Ni(0.4)/NiFe(x)/Ni(0.4) with x = 0.4-3.2 nm in steps of 0.4 nm, and for comparison, NiFe(d) samples with d = 0.4-3.2 nm in steps of 0.4 nm. We chose the thick base to emulate the layer growth closer to what we have for our Josephson junctions. The moment versus field measurements were performed in SQUID-VSM mode at 10 K and the sample areas were measured using an optical microscope. Because of the presence of two different ferromagnetic layers, we plot the moment/area (instead of moment/volume) versus field curves for selected thicknesses of all 4 samples sets in Fig. 5.1.

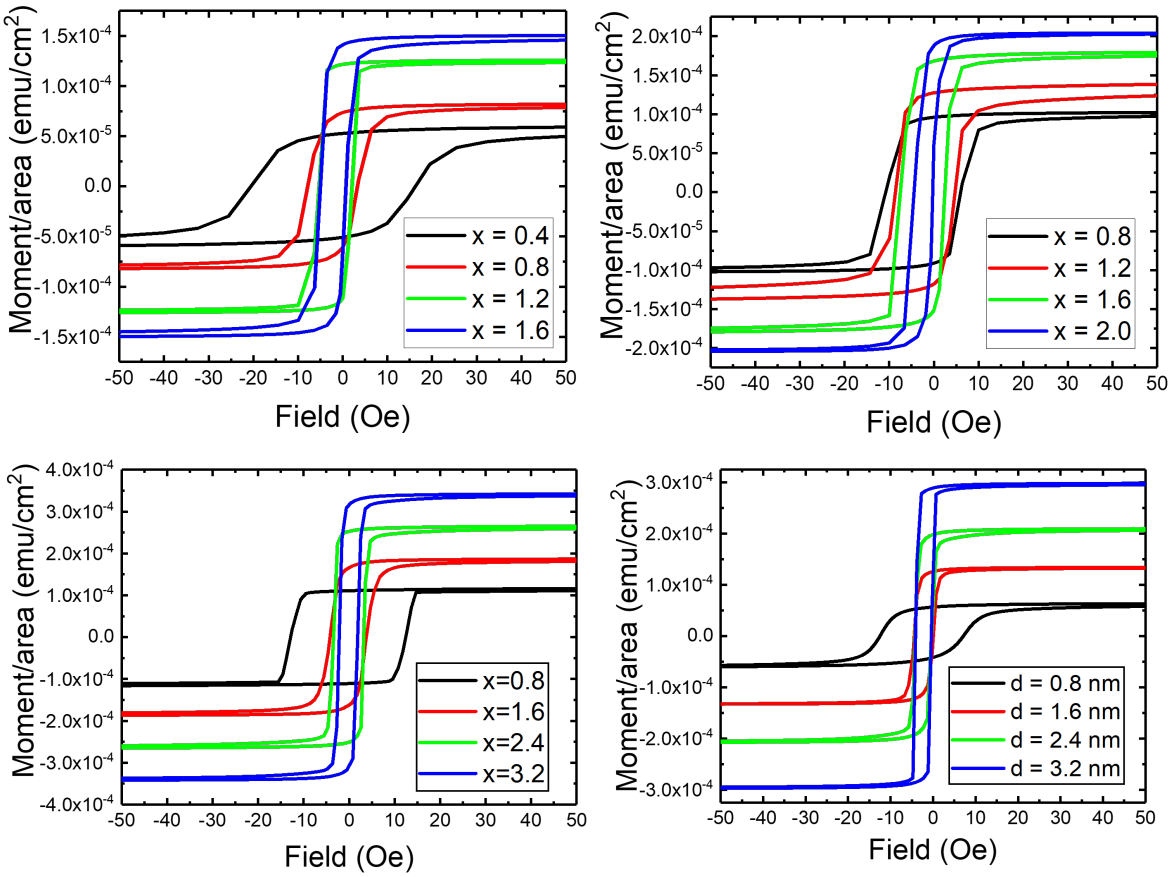

Figure 5.1: **Moment/area vs H for Ni/NiFe/Ni and NiFe.** The Ni(0.2)/NiFe(x)/Ni(0.2), Ni(0.3)/NiFe(x)/Ni(0.3), Ni(0.4)/NiFe(x)/Ni(0.4) and NiFe(d) sample sets are shown in the following order: top left, top right, bottom left and bottom right.

As seen in the figure, all curves switch in similar field ranges. Although addition of Ni changes the magnetic properties, the changes are not too significant and do not severely degrade the switching. Since our main goal is to compare the magnetic properties of NiFe samples with Ni with those of plain NiFe, we fit these curves to the Gaussian error function (Eqn. 2.26) and compared the fitting parameters next. Because of the presence of different Ni thickness in different sets, it is harder to compare them directly with varying NiFe thickness. Therefore, we decided to use the total ferromagnetic thickness $d_F = d_{\mathrm{Ni}} + d_{\mathrm{NiFe}}$ as our x-axis. The extracted coercivities H_c and switching width (sigma) values are plotted against total F thickness in Fig. 5.2.

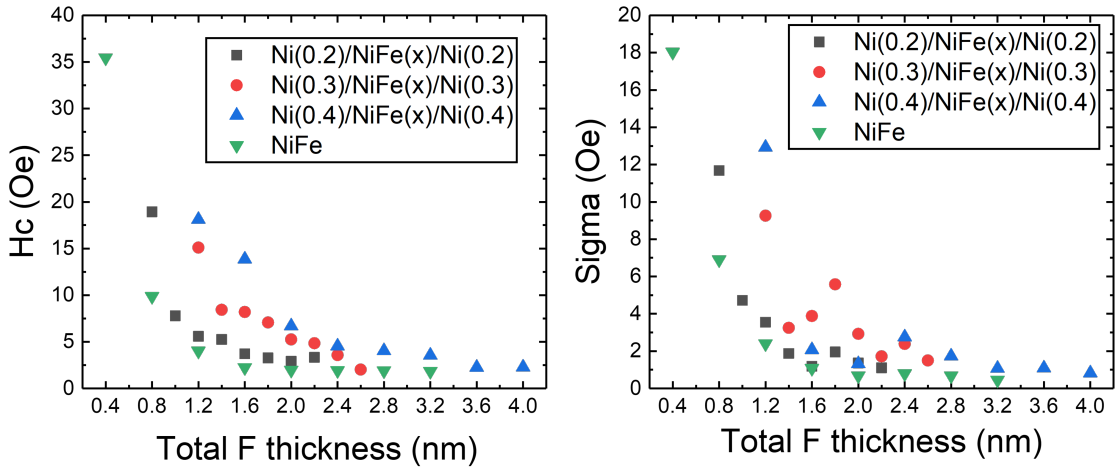

Figure 5.2: **H_c and Sigma vs total F thickness for Ni(0.2)/NiFe(x)/Ni(0.2), Ni(0.3)/NiFe(x)/Ni(0.3), Ni(0.4)/NiFe(x)/Ni(0.4) and NiFe(x).** Both quantities fall with the thickness, as expected.

The coercivities of all sample sets drop with thickness, as expected. We can also see that the coercivity of each set increases with an increase in added Ni thickness around NiFe. There is more scatter in the sigma values (which represent the switching width), however, they also drop similarly with thickness. We also compared the squareness of these samples, however there was too much scatter to find any pattern and therefore we do not show them.

Therefore, all 3 sets of Ni/NiFe/Ni have properties that are reasonably close to the NiFe samples and seem like a viable replacement. We decided to further explore the Ni(0.4) samples for our junctions because the amount of Ni in them is higher and thus any effect we expect in our junctions might be more prominent at this thickness over the thinner ones. We extracted the saturation moment M_{sat} for the Ni(0.4)/NiFe(d_{NiFe})/Ni(0.4) samples and plotted them with respect to the NiFe thickness d_{NiFe}, as shown in Fig. 5.3. The error bars represent 5% uncertainty attributed to the area estimation method.

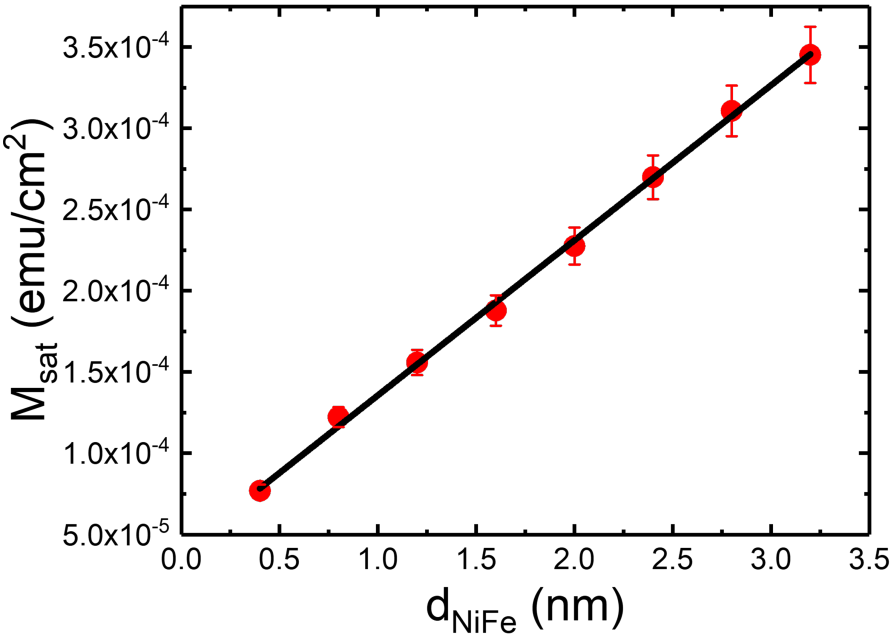

Figure 5.3: **$\mathbf{M_{sat}}$ vs $\mathbf{d_{NiFe}}$ for Ni(0.4)/NiFe($\mathbf{d_{NiFe}}$)/Ni(0.4).** The black line is a linear fit of the experimental data in red circles.

By performing a linear fit on the curve, we obtain the value of M_{NiFe} from the slope to be 952 $\pm$ 14 emu/cm^3 and the value of M_{Ni} from the intercept to be 507 $\pm$ 36 emu/cm^3. The value for Ni is very close to the nominal low-temperature magnetization value for bulk Ni of 510 emu/cm^3 [88]. This implies that there are minimal magnetic "dead layers" at the

Cu/Ni and Ni/NiFe interfaces. The NiFe value is somewhat higher than the expected value of 930 emu/cm^3 for $Ni_{80}Fe_{20}$ [88]. We attribute the discrepancy to the uncertainty in the sample areas and the small thickness range explored.

5.2.2 Transport properties of Josephson junctions

Josephson junctions were fabricated using the methods outlined in Chapter 3. The bottom lead [Nb(25)/Al(2.4)]$_3$/Nb(20)/Cu(2)/F/Cu(2)/Nb(5)/Au(10) was deposited first. After formation of elliptical pillars of 1.25 µm × 0.5 µm, 5 nm of Au was milled and then top lead Nb(160)/Au(10) was deposited. We deposited 3 sets of F: Ni(0.4)/NiFe(d_{NiFe})/Ni(0.4) where d_{NiFe} was varied from 0.4 to 3.4 nm in steps of 0.2 nm; Ni(0.2)/NiFe(d_{NiFe})/Ni(0.2) where d_{NiFe} was varied from 0.2 to 1.6 nm in steps of 0.2 nm; NiFe(d_{NiFe}) where d_{NiFe} was varied from 1.0 to 3.7 nm in steps of 0.1 nm. The measurements were performed at 4.2 K inside a liquid helium Dewar using a probe equipped with a superconducting magnet. The NiFe(d_{NiFe}) samples were fabricated and measured by Joshua Willard.

$I - V$ curves were measured in fields up to 80 mT in both directions. The $I - V$ curves were then fit to the RSJ model (Eqn. 2.19) discussed previously to extract the values of critical current I_c. The dependence of I_c on the magnetic field H for a typical sample is plotted in Fig. 5.4 and fit to the Airy function (Eqn. 2.48) for the case with an internal magnetization as discussed in Chapter 2.

The hysteresis arising from the internal magnetization of the ferromagnetic layers in the junction shifts the center of the Airy pattern in the direction of the field sweep. A sudden drop in I_c seen around ± 10 mT is due to the switch in the magnetization direction of the ferromagnetic layers. The field shift and switching field depend on the magnetic properties of the ferromagnetic layers and vary with NiFe thickness as predicted by the flux in the

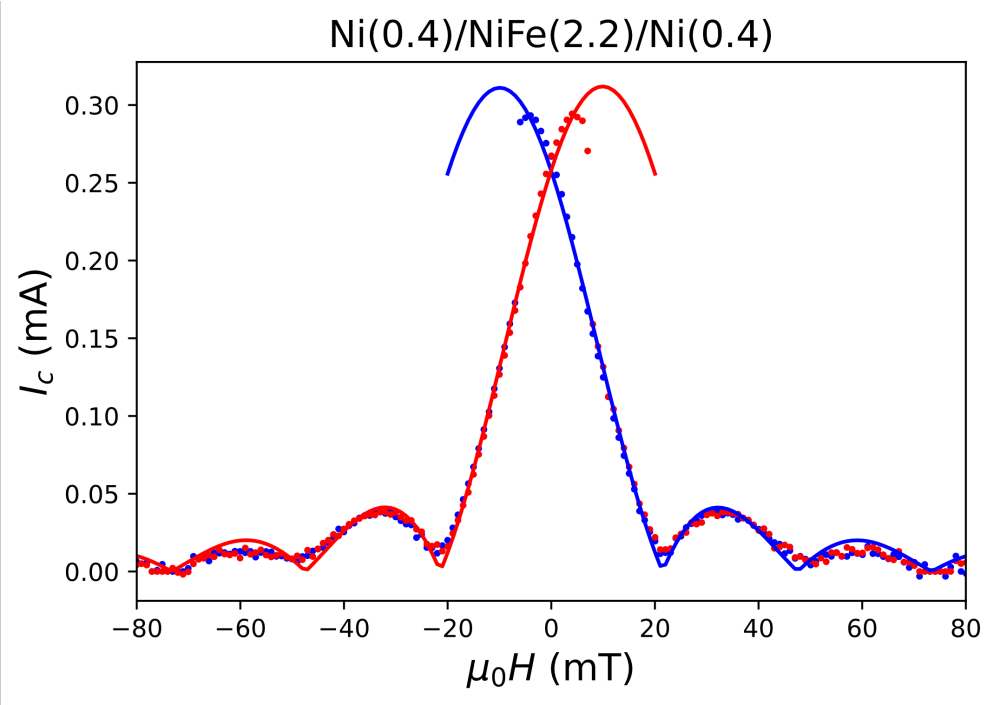

Figure 5.4: **I_c vs H for Ni(0.4)/NiFe(2.2)/Ni(0.4).** The solid lines are fits to the Airy function (Eqn. 2.48) for the upsweep (red) and downsweep (blue).

Airy function (see Eqn. 2.48). Because of the sudden switch, the value of I_{c0} in Eqn. 2.48 is usually higher than the value seen experimentally. The "true" maximum value must be extracted from the fit, as shown by the extended fit lines in the figure.

We multiply the maximum I_c value (obtained from the Airy fit) by the normal state resistance R_N to obtain I_cR_N. This product is independent of the junction area. Figure 5.5 shows a plot of I_cR_N versus the total F layer thickness d_F. Two junctions at each thickness were measured to factor for variations in thickness and interface quality during the sputtering process. The figure shows I_cR_N versus d_F for all the measured Josephson junctions containing Ni(0.4)/NiFe(d_{NiFe})/Ni(0.4) & Ni(0.2)/NiFe(d_{NiFe})/Ni(0.2) on the same plot in panel (a) and NiFe(d_{NiFe}) in panel (b). The solid lines are fits to Eqn. 2.51.

As can be seen from the figures, the maximum value of I_cR_N in the π-state of the junctions (occurring at $d_F \approx 1.6$ nm in panel (a)) is four to five times larger for the

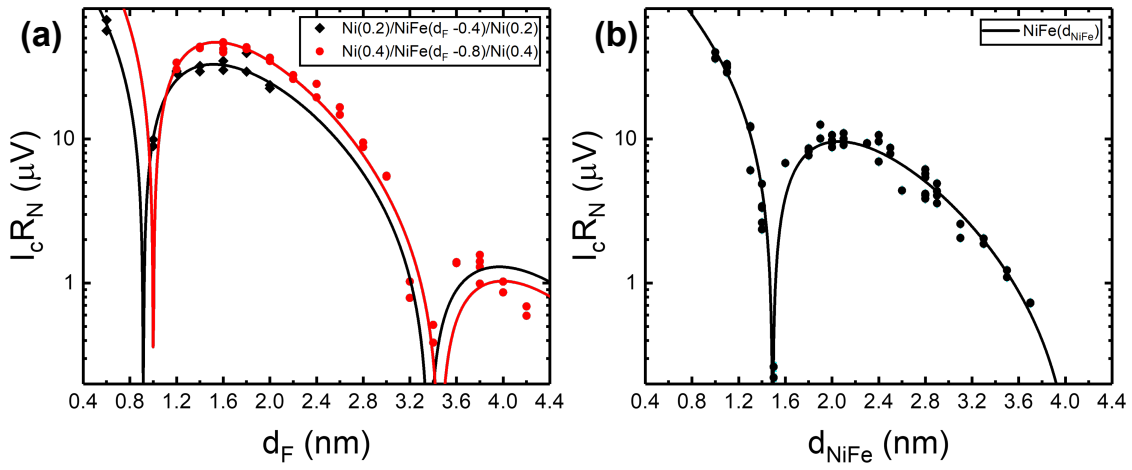

Figure 5.5: **I_cR_N vs d for Ni(0.4)/NiFe/Ni(0.4), Ni(0.2)/NiFe/Ni(0.2) and NiFe.** (a) I_cR_N vs d_F for Ni(0.4)/NiFe(d_{NiFe})/Ni(0.4) & Ni(0.2)/NiFe(d_{NiFe})/Ni(0.2) and (b) I_cR_N vs d_{NiFe} for NiFe(d_{NiFe}). The solid lines are fits to Eqn. 2.51. The NiFe(d_{NiFe}) data are courtesy of Joshua Willard.

Ni(0.4)/NiFe/Ni(0.4) junctions and about three times larger for the Ni(0.2)/NiFe/Ni(0.2) junctions, compared with the NiFe junctions without Ni at the interfaces (occurring at $d_{\mathrm{NiFe}} \approx 2.1$ nm in panel (b)). The fit parameters for all three data sets are tabulated in Table 5.2.

Sample	V_0 (μV)	ξ_{F1} (nm)	ξ_{F2} (nm)	$d_{0-\pi}$ (nm)
Ni(0.4)/NiFe(d_F-0.8)/Ni(0.4)	800 ± 110	0.64 ± 0.02	0.78 ± 0.01	1.00 ± 0.02
Ni(0.2)/NiFe(d_F-0.4)/Ni(0.2)	349 ± 39	0.76 ± 0.05	0.78 (fixed)	0.92 ± 0.01
NiFe(d_{NiFe})	252 ± 48	0.71 ± 0.04	0.74 ± 0.06	1.49 ± 0.01

Table 5.2: **Fit parameters for Ni(0.4)/NiFe/Ni(0.4), Ni(0.2)/NiFe/Ni(0.2) and NiFe.** Parameters obtained from fits of Eqn. 2.51 to the data shown in Fig. 5.5 for junctions containing Ni(0.4)/NiFe(d_F-0.8)/Ni(0.4), Ni(0.2)/NiFe(d_F-0.4)/Ni(0.2) and NiFe(d_{NiFe}). The value of ξ_{F2} for Ni-0.2 samples was fixed to the value obtained from the Ni-0.4 data set, 0.78 nm. This is because of less number of junctions fabricated and measured in this set, so there are not enough data points to establish the oscillation period.

There are two possible explanations for this increase in the I_cR_N values. Firstly, it could

be because of a shift in the location of the peak of the π-state to a lower thickness because of the added Ni layers, thus creating an "illusion" of enhancement. This enhancement of I_cR_N achieved due to the damping-oscillatory nature of the pair correlation function is well studied [76, 102]. The position of the first 0-π in Fig. 5.5 show that the transition has been shifted from an F-layer thickness of 1.5 nm for the case of NiFe to a total F-layer thickness of 0.9-1.0 nm for Ni/NiFe/Ni. Because of this shift, the maximum value of I_c occurs at 1.6 nm for Ni/NiFe/Ni, somewhat thinner than the 2.1 nm of NiFe. There is also less NiFe in the Ni/NiFe/Ni layers versus the NiFe which could lead to a smaller decay.

Secondly, it could be because of the hypothesis based on spin-dependent scattering parameters ($\gamma_{F/N}$ and $2AR^*_{F/N}$) derived from the GMR data that was discussed in the previous section. We suggested that the supercurrent will likely be larger in systems with small values of both $2AR^*$ and γ, all other things being equal. This enhancement might be reduced because of the addition of two Ni/NiFe interfaces, but because the Ni layers are very thin, one could view the Ni/NiFe/Ni as a single material with a spatial gradient in Fe concentration instead of 3 different layers. We think it is more likely that the second explanation is the more significant of the two, however theoretical and computational studies on such systems need to be made for a better understanding and to establish the exact reason.

The first $0-\pi$ transition at $d_F < 1.0$ nm made it difficult for us to fabricate junctions in the 0-phase for Ni(0.4)/NiFe(d_F-0.8)/Ni(0.4). Below 0.4 nm of NiFe, we can hardly claim that the resulting junctions are NiFe-like, since they would clearly be dominated by 0.4 nm of Ni on each side. But the I_cR_N data suggest that, even at Ni(0.4)/NiFe(0.4)/Ni(0.4), the junctions are still in the π-phase as can be seen in the downturn in I_cR_N as d_F decreases below 1.6 nm. Fabricating the Ni-0.2 samples enabled us characterize even thinner junctions and the data clearly suggest that the junctions with $d_F = 0.6$ nm are in the 0-phase, while

the $0-\pi$ transition occurs in the vicinity of $d_F = 0.9$ nm. Because of the similar structure and material thicknesses of the junctions, this result for the Ni-0.2 set indirectly makes a strong case for the Ni-0.4 set to also have a $0-\pi$ transition at a similar thickness. However, as we mentioned earlier, this is not possible to verify directly.

We also discuss the field shift, junction size and resistance variation in these Josephson junctions in Appendix E and F.

5.3 Pd/NiFe/Pd system

In this section, we study the magnetic properties of Pd/NiFe/Pd films and compare their properties with Cu/NiFe/Cu films. We then study the supercurrent transport properties of Josephson junctions containing these layers and perform a similar comparison. We are currently working on a manuscript based on these results.

5.3.1 Magnetic properties of blanket films

As discussed earlier, we wanted to replace the Cu/NiFe interfaces in our Josephson junctions with Pd/NiFe interfaces. The motivation behind this was the lower values of GMR parameters $\gamma_{F/N}$ and $2AR^*_{F/N}$ that we believe might be favorable for supercurrent transmission [39]. We first studied the magnetic properties of Pd/NiFe/Pd blanket films and compared them to Cu/NiFe/Cu to make sure that the coercivity and switching width were in similar ranges. We deposited $[Nb(25)/Al(2.4)]_3$/Nb(20)/Pd(2)/NiFe(x)/Pd(2)/Nb(5) where x = 0.4-3.2 nm in steps of 0.4 nm and $[Nb(25)/Al(2.4)]_3$/Nb(20)/Cu(2)/NiFe(x)/Cu(2)/Nb(5) samples with x = 0.4-3.2 nm in steps of 0.4 nm. The thick Nb/Al base was chosen to have the stack similar to our Josephson junctions. The moment vs field measurements were performed in SQUID-VSM mode at 10 K and the sample areas were measured using an optical

microscope. Moment/area vs field curves for selected thicknesses of both sample sets are shown in Fig. 5.6.

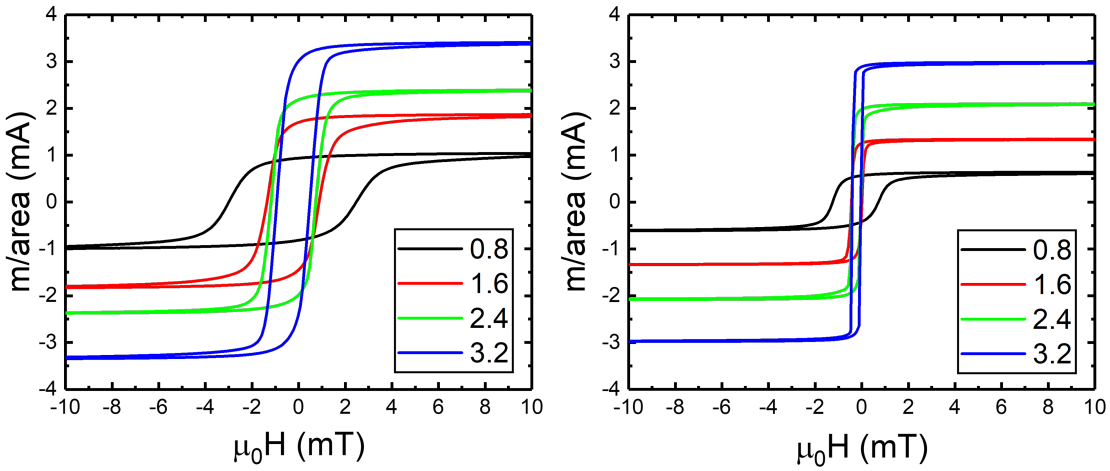

Figure 5.6: **m/area vs H for Pd(2)/NiFe(x)/Pd(2) and Cu(2)/NiFe(x)/Cu(2).** The samples with Pd are on the left panel and the samples with Cu are on the right panel.

As seen in the figure, the m/area for Pd(2)/NiFe(x)/Pd(2) is somewhat larger than that of Cu(2)/NiFe(x)/Cu(2). This is because of magnetic polarization of Pd due to the adjacent NiFe layer. We fit the above curves to the Gaussian error function (Eqn. 2.26) and compared the fit parameters. The extracted coercivities H_c for both sample sets are plotted against d_{NiFe} in Fig. 5.7.

The coercivities of both sample sets drop with thickness, as expected. The coercivities of the samples with Pd spacers is larger than those of the corresponding samples with Cu spacers. We found that Pd(2)/NiFe(0.4)/Pd(2) had a much higher coercivity than other samples in the set. We also extracted the saturation moment per unit area (m_{sat}/area) for Pd(2)/NiFe(x)/Pd(2) samples and plotted them versus the NiFe thickness (d_{NiFe}) as shown in Fig. 5.8. The error bars represent 5% uncertainty attributed to the area estimation method.

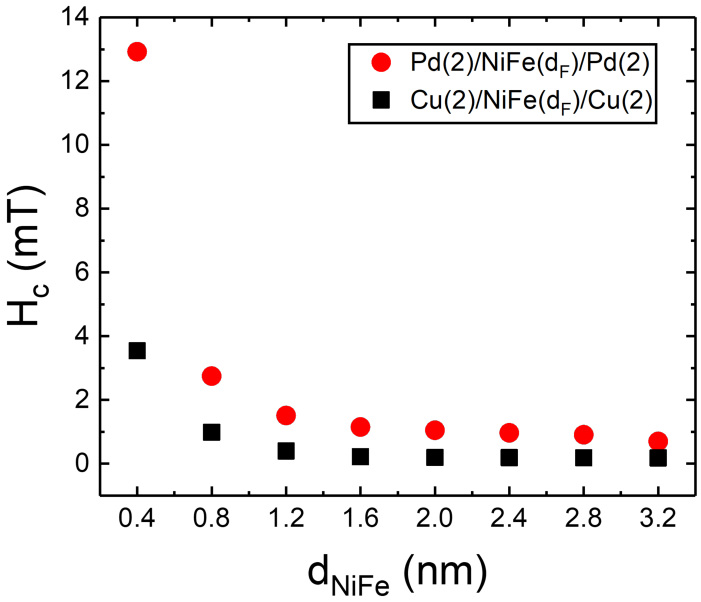

Figure 5.7: **H_c vs d_{NiFe} for Pd(2)/NiFe(x)/Pd(2) and Cu(2)/NiFe(x)/Cu(2).** H_c falls with increasing d_{NiFe}, as expected.

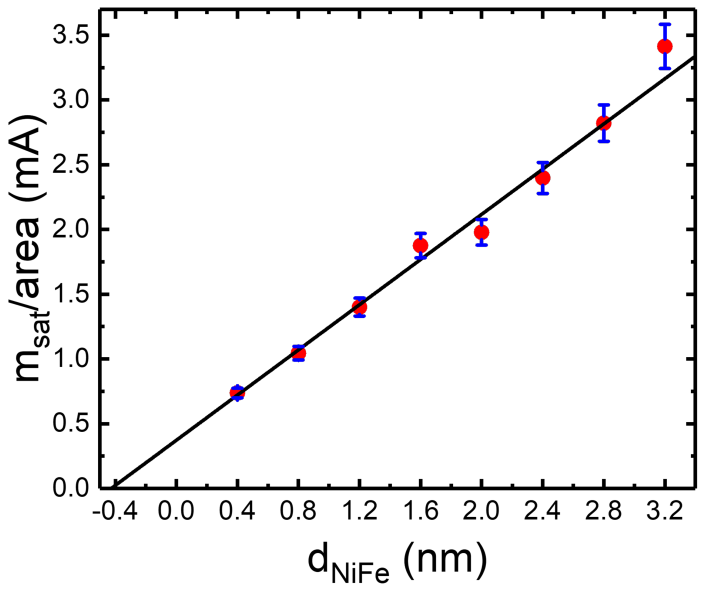

Figure 5.8: **m_{sat}/area vs d_{NiFe} for Pd(2)/NiFe(x)/Pd(2).** The data are shown in red circles, error bars in blue and the black line is a linear fit.

By performing a linear fit of the data in Fig. 5.8, we obtain the value of M_{NiFe} from the slope to be 872 ± 34 kA/m. This value is somewhat lower than the expected value of 930 kA/m for $Ni_{80}Fe_{20}$ [88]. We attribute this discrepancy to the uncertainty in the sample areas and the possible upward curvature of the data due to the small thickness range explored. The value of the x-intercept indicates that the polarization in the Pd layer is equivalent to 0.43 nm of NiFe i.e. as if each side of the NiFe layer had an extra thickness of 0.21 nm.

5.3.2 Transport properties of Josephson junctions

Josephson junctions containing Pd/NiFe/Pd were fabricated using the methods discussed in Chapter 3. We deposited the bottom lead containing $[Nb(25)/Al(2.4)]_3$/Nb(20)/Pd(2)/NiFe(x)/Pd(2)/Nb(5)/Au(10) first where x = 0.4-3.2 nm in steps of 0.2 nm. Then elliptical pillars of dimension 1.25 µm × 0.5 µm were formed. 5 nm of Au was then milled the top lead Nb(160)/Au(10) was deposited. Four probe measurements with varying field were performed at 4.2 K inside a liquid helium Dewar. The Cu/NiFe/Cu junctions were fabricated and measured by Joshua Willard previously for the Ni/NiFe/Ni study and we reused the data for comparison.

The $I-V$ curves were measured in fields up to 100 mT in both directions. The $I-V$ curves were then fit to the RSJ model (Eqn. 2.19) and critical current I_c values were extracted. The dependence of this I_c on the magnetic field H for a typical sample is plotted in Fig. 5.9. The solid lines are fits to the Airy function (Eqn. 2.48) for the case with an internal magnetization, discussed in Chapter 2.

Similar to the Ni/NiFe/Ni Josephson junctions discussed earlier, we see a horizontal shift in the pattern and a sudden drop in I_c which depend on the NiFe thickness. The maximum I_c value was extracted from the fit, as shown by the extended fit lines in the

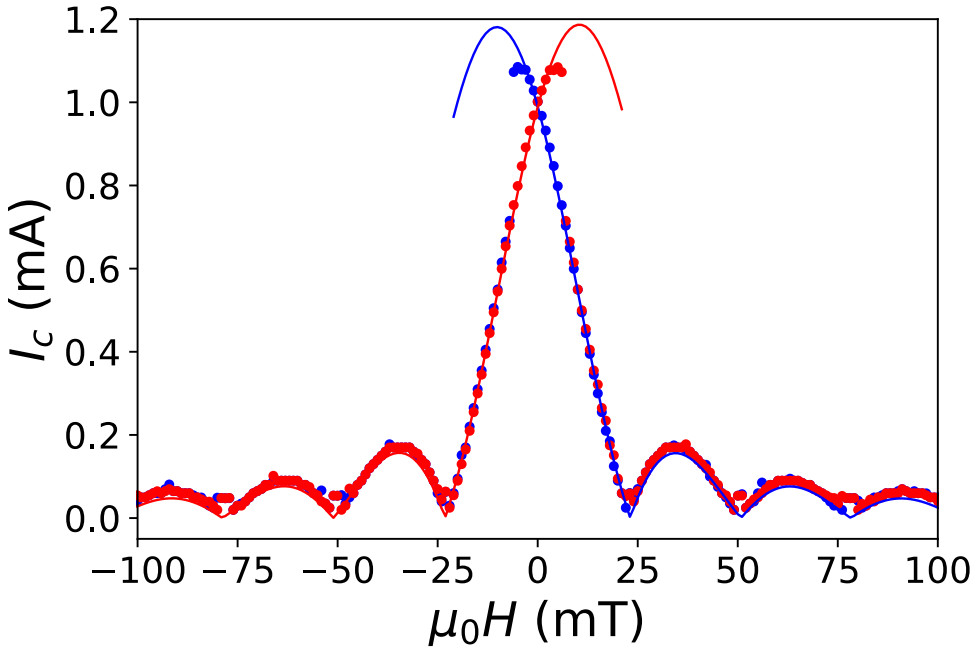

Figure 5.9: **I_c vs H for Pd(2)/NiFe(1.2)/Pd(2).** The solid lines are fits to the Airy function (Eqn. 2.48) for upsweep (red) and downsweep (blue).

figure. The maximum I_c value was then multiplied by the normal state resistance R_N to obtain I_cR_N to account for variations in junction area during fabrication. A plot of I_cR_N vs NiFe thickness (d_{NiFe}) is shown in Fig. 5.10 for all the measured Josephson junctions containing Pd(2)/NiFe(d_{NiFe})/Pd(2) in the left panel and Cu(2)/NiFe(d_{NiFe})/Cu(2) in the right panel. The solid lines are fits to Eqn. 2.51, discussed earlier.

As can be seen from the figures, the maximum value of I_cR_N in the π-state of the junctions occurring at $d_{\mathrm{NiFe}} \approx 1.2$ nm for Pd(2)/NiFe(d_{NiFe})/Pd(2) is about two times larger than that of Cu(2)/NiFe(d_{NiFe})/Cu(2) occurring at $d_{\mathrm{NiFe}} \approx 2.1$ nm. This enhancement seems to validate our original hypothesis based on the spin-dependent parameters at the F/N interface from GMR data. The fit parameters (from Eqn. 2.51) for both data sets are tabulated in Table 5.3.

The Pd/NiFe/Pd data exhibit a $0 - \pi$ transition at a thickness of around 0.6 nm, which

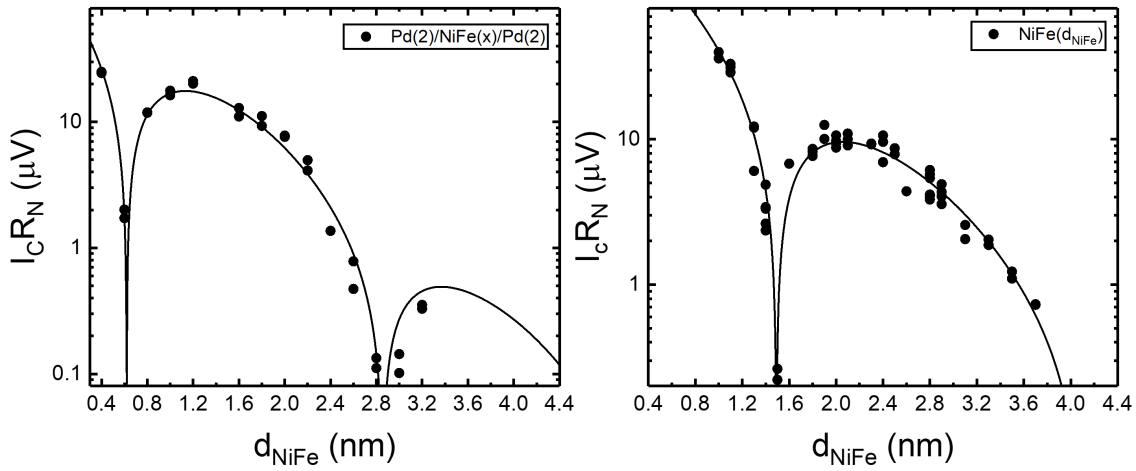

Figure 5.10: **I_cR_N vs d_{NiFe} for Pd(2)/NiFe/Pd(2) and Cu(2)/NiFe/Cu(2).** I_cR_N vs d_{NiFe} for Pd(2)/NiFe(d_{NiFe})/Pd(2) (left) and Cu(2)/NiFe(d_{NiFe})/Cu(2) (right). The solid lines are fits to Eqn. 2.51. The Cu/NiFe/Cu data are courtesy of Joshua Willard.

Sample	Pd(2)/NiFe/Pd(2)	Cu(2)/NiFe/Cu(2)
V_0 (μV)	164 ± 6	252 ± 48
ξ_{F1} (nm)	0.63 ± 0.02	0.71 ± 0.04
ξ_{F2} (nm)	0.71 ± 0.01	0.74 ± 0.06
$d_{0-\pi}$ (nm)	0.62 ± 0.01	1.49 ± 0.01

Table 5.3: **Fit parameters for Pd(2)/NiFe/Pd(2) and Cu(2)/NiFe/Cu(2).** Parameters determined from fits of Eqn. 2.51 to the data shown in Fig. 5.10 for junctions containing Pd(2)/NiFe(d_{NiFe})/Pd(2) and Cu(2)/NiFe(d_{NiFe})/Cu(2).

when added with the 0.42 nm of Pd polarisation discussed earlier, is similar to that of Ni [80]. However, this value is shorter than the 1.5-1.7 nm observed in NiFe [33, 54, 101]. We saw a similar unexplained effect in our Cu/Ni/NiFe/Ni/Cu data. This seems to indicate that the interface is also playing a strong role (along with the Pd polarization) in determining the location of the $0 - \pi$ transition [102].

5.4 Conclusions

The Josephson junctions in the JMRAM device contain Ni as fixed layers and NiFe as free layers but supercurrent transmission through NiFe is significantly lower compared to Ni. To increase the supercurrent transmission through the free layer, we looked at the transport at the interface of the ferromagnet and adjacent normal metal in previous GMR studies. We found that Ni/Cu and NiFe/Pd interfaces have better properties for supercurrent transmission compared to NiFe/Cu interfaces. We studied the role of interfaces in the supercurrent transport by adding thin layers of Ni around NiFe and also by replacing Cu with Pd in a different study.

For Ni(0.4)/NiFe(d_{NiFe})/Ni(0.4), we found that the maximum value of $I_c R_N$ in the π-state was four to five times larger compared with the NiFe(d_{NiFe}) junctions without Ni [101]. We saw a similar improvement by a factor of three for the Ni(0.2)/NiFe(d_{NiFe})/Ni(0.2) junctions. For Pd(2)/NiFe(d_{NiFe})/Pd(2), the maximum value of $I_c R_N$ in the π-state of the junctions was found to be about two times larger than that of Cu(2)/NiFe(d_{NiFe})/Cu(2). Both studies support our hypothesis that the supercurrent transmission through a ferromagnetic Josephson junction can be improved by switching to interfaces with better spin-dependent transport properties.

Chapter 6

Conclusions and Outlook

In this concluding chapter, we summarize the thesis by emphasizing the main experimental results and providing a brief outlook of future studies that could be performed.

In Chapter 1, we introduced superconducting computing and the current state of its development. We then talked about superconducting memory architectures with the specific example of JMRAM by Northrop Grumman Corporation. We then talked about our own research at Michigan State University its relation to the JMRAM project. In Chapter 2, we introduced the theory behind superconductivity, ferromagnetism and the interaction between the two via proxmity effect. We then discussed the Josephson effect and the theory behind Josephson junctions. We then presented the properties of ferromagnetic Josephson junctions. In Chapter 3, we introduced the equipment that we use for the fabrication and measurement of our samples. We also discussed in the processes detail.

In Chapter 4, we introduced synthetic antiferromagnets with the motivation of using unbalanced Ni/Ru/Ni SAFs as a replacement for plain Ni in the pseudo-spin valve structure used in JMRAM. We characterized the magnetic properties of balanced Ni/Ru/Ni blanket films and found their RKKY interaction profile versus thickness. Then, we studied the supercurrent transport through balanced Ni/Ru/Ni Josephson junctions and found that the Fraunhofer patterns were symmetric, as predicted by theory. We also observed that the I_cR_N decays very slowly with Ni thickness and speculated that the reason behind this slow decay must be the phase cancellation in opposing Ni layers, as predicted by theory. This slow

decay could enable the advantage of using thicker Ni layers with better magnetic properties compared to plain Ni. We then studied the magnetic properties of unbalanced Ni/Ru/Ni SAFs which behaved as expected. We then studied their magnetic properties as part of a spin-valve structure with NiFe and found that in some cases, the unbalanced Ni/Ru/Ni SAFs has a lower switching field of the free layer compared to that in plain Ni of equivalent thickness. However, further studies need to be conducted to characterize the magnetic properties of a wide range of thickness pairs of these unbalanced SAFs to select the best thicknesses which show a clear advantage over plain Ni. Josephson junctions with these structures need to be studied next and compared with Josephson junctions containing Ni to see if there is a clear magnetic advantage and to quantify the reduction in critical current compared to Ni.

In Chapter 5, we introduced the spin-dependent transport properties at F/N interfaces studied extensively in GMR. We then hypothesized that F/N pairs with "better" spin-dependent transport properties will have a higher supercurrent transmission. We found that Cu/Ni and Pd/NiFe interfaces had better properties compared to Cu/NiFe interfaces. To this effect, we studied the supercurrent transport through Cu/Ni/NiFe/Ni/Cu Josephson junctions and compared them with Cu/NiFe/Cu Josephson junctions. We found that the supercurrent transmission was 4-5 times higher in the π state for the former, showing a clear improvement. We also studied Pd/NiFe/Pd Josephson junctions and found that the supercurrent transmission was 2 times higher in the π state compared to Cu/NiFe/Cu Josephson junctions. Results from both studies seem to support our hypothesis that spin-dependent properties affect the supercurrent transmission. Experimental studies need to be performed on various F/N pairs to see if similar improvements are seen across a broad range of material pairs. However, to establish the mechanism behind these results, it would be helpful to have first principle theoretical studies of these systems performed.

APPENDICES

Appendix A

Magnetic properties of Ni/Ag/Ni blanket films

We found studies of Ni/Ag/Ni synthetic antiferromagnets in the literature with Ni thickness of 0.8 nm with the peak in antiferromagnetic coupling at an Ag thickness of 1.0 nm [103]. These samples were deposited on glass substrates and at very low temperatures, but we wanted to replicate them in our deposition system to see if this was possible. We deposited blanket films of Nb(5)/Cu(2)/[Ni(0.8)/Ag(x)]$_n$/Ni(0.8)/Cu(2)/Nb(5) multi-layers. We kept the Ni thickness fixed at 0.8 nm and varied the Ag thickness x between 0.9-1.3 nm in steps of 0.1 nm and the n = 2, 4 and 7. We also had one sample Nb(5)/Cu(2)/[Ni(0.8)/Ag(1.0)]$_{30}$/Ni(0.8) /Cu(2)/Nb(5). The Nb(5)/Cu(2) base and top layers were used to facilitate better growth and to protect the layers from oxidation, respectively. The deposition took place with the usual pressure and temperature parameters (-25°C) with a large Ag gun. We then measured the moment versus field curves of these samples in the SQUID-VSM at 10K, as shown in Fig. A.1. The measurements were performed in VSM mode with a field range of ±4000 Oe at 5 K, but we only show a blown up version of the curves between ±1000 Oe (200 Oe for the last sample) for visual clarity.

All the samples have ferromagnetic behavior as seen in the curves. The increase in n increased the saturation moment value, as expected. For most cases, the coercivity of the curves increased with increasing Ag thickness. We suspect that this could be because Ag has a tendency to form clusters during deposition [104]. Poor Ag growth at the deposition temperature of -25°C can lead to a poor coupling between the Ni layers.

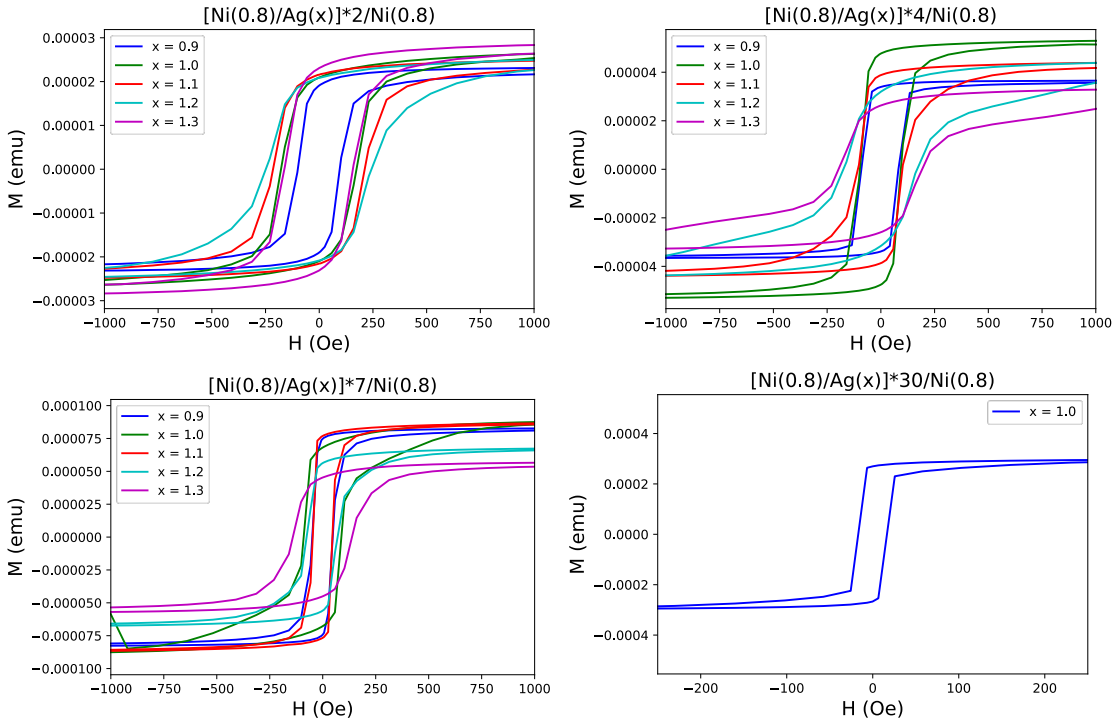

Figure A.1: **Moment vs field for $[Ni(0.8)/Ag(x)]_n/Ni(0.8)$.** None of the samples show antiferromagnetic behavior.

Next, we focused on the deposition parameters. We know that the deposition quality of Ag can vary with the gun and the temperature. To test if that changes the magnetic behavior of the samples, we deposited 3 sets of the same Nb(5)/Cu(2)/$[Ni(0.8)/Ag(x)]_3$/Ni(0.8) /Cu(2)/Nb(5) sample where x = 1.0-1.3 nm in steps of 0.1 nm. The first set was sputtered with a small Ag gun around -25 °C, the second set was also sputtered with the small Ag gun but around -80 °C and the third set was sputtered with a big Ag gun around -80 °C. The deposition rate of the small Ag guns was 1.5 Å/s while that of the big guns was 2.0 Å/s. The moment versus field measurements were performed at a field of ± 8000 Oe at 5 K, as shown in Fig. A.2. The larger field was used because some of the samples did not fully saturate at ± 4000 Oe. Unfortunately, all of the samples were found to be ferromagnetic again. We saw slightly better deposition results with the big Ag gun, but the differences were minimal.

We were unable to deposit samples at even lower temperatures as we were already at the

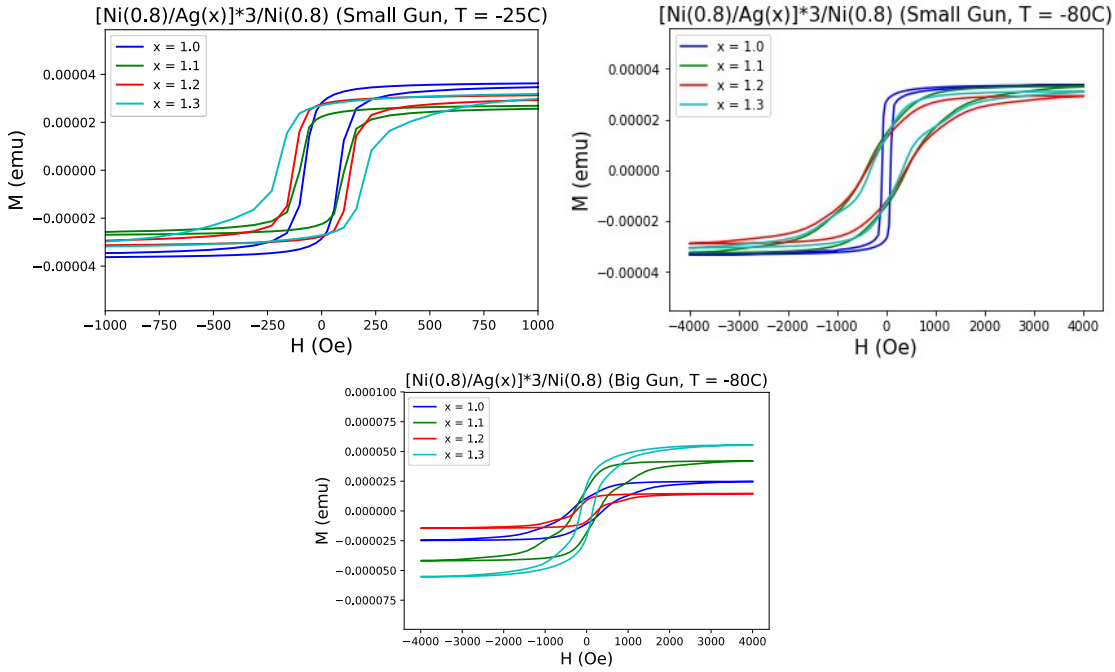

Figure A.2: **Moment vs field for [Ni(0.8)/Ag(x)]$_3$/Ni(0.8).** The samples were deposited using two different guns and at two different temperatures.

lowest limit possible for our sputtering chamber. So the next thing we did was to sputter samples with a bigger thickness range for Ag to check if we had wrongly guessed the thickness range where we should be expecting to see the antiferromagnetic coupling. We deposited Nb(5)/Cu(2)/[Ni(0.8)/Ag(x)]$_3$/Ni(0.8)/Cu(2)/Nb(5) where x = 1.4-2.1 nm in steps of 0.1 nm. We used the big Ag target for this run with a deposition temperature of -75 °C. The The moment vs field measurements were performed at a field of ± 8000 Oe at 5 K.

Unfortunately, these samples were also found to be ferromagnetic for this Ag thickness range. We attribute this failure to obtain the antiferromagnetic coupling to the inability to obtain low enough temperatures required for the smooth deposition of Ag.

Later, we found examples of Ag deposition where the Ag layer was deposited first to enable smooth deposition [105]. We decided to repeat this and deposited Nb(5)/Cu(2)/ Ag(x)/Ni(0.8)/Ag(x)/Ni(0.8)/Ag(x)/Cu(2)/Nb(5) where x = 0.9 - 1.5 nm in steps of 0.2

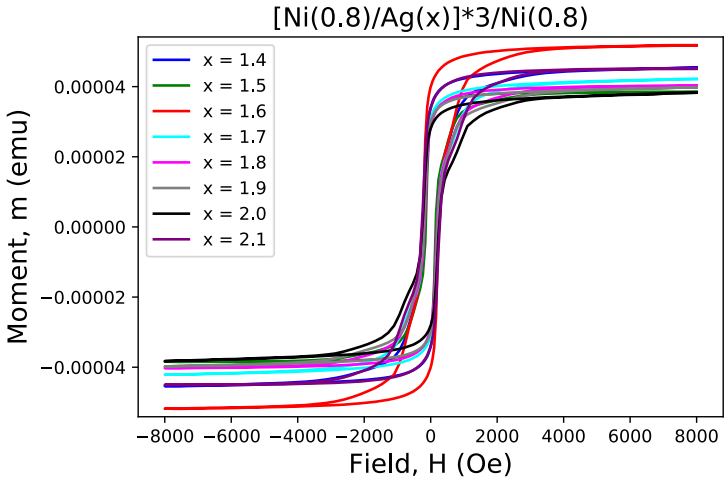

Figure A.3: **m vs H for $[Ni(0.8)/Ag(x)]_3/Ni(0.8)$.** None of the samples show strong antiferromagnetic behavior.

nm. The moment versus field measurements were performed at a field of ± 5000 Oe at 10K. The moments were divided by the sample area to get moment/area versus field. The curves are shown in Fig. A.4.

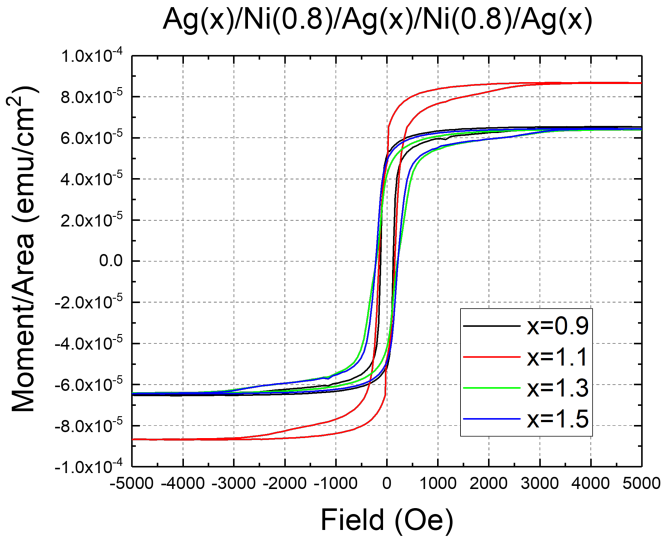

Figure A.4: **Moment/area vs field for $[Ag(x)/Ni(0.8)]_2/Ag(x)$.** None of the samples show antiferromagnetic behavior.

Unfortunately, all the samples were ferromagnetic. The reason behind the higher moment for x = 1.1 nm is unknown, however it is likely because of an incorrect area.

Appendix B

Magnetic properties of Ni blanket films

The discussion in this appendix was published in [26]. Since Ni has been extensively used throughout this thesis work, we studied the magnetic properties of Ni blanket films. We sputtered Nb(5)/Cu(2)/Ni(d_{Ni})/Cu(2)/Nb(5) samples with d_{Ni} = 1.2, 1.6, 2.0, 3.0 and 4.0 nm. We measured magnetization (M) versus field (H) curves for these samples at 10 K using MPMS3 and show a selected set in Fig. B.1.

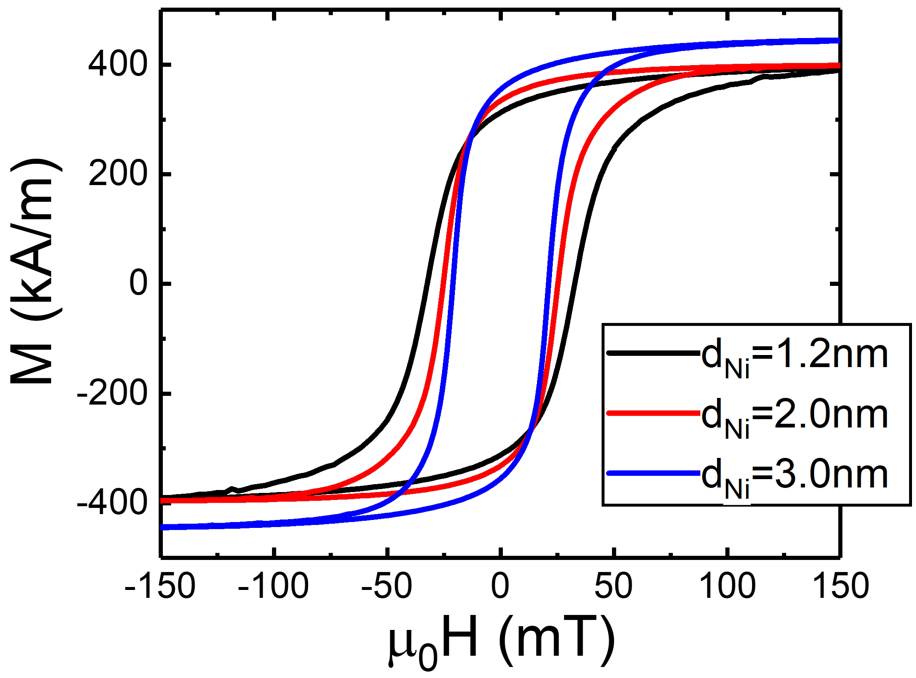

Figure B.1: **M vs H for Ni(x).** Figure was taken from [26].

As seen in Fig. B.1, the coercivity of Ni increases with decreasing thickness. The field above which the irreversible behavior ceases also increased with decreasing thickness. This

field is close to the saturation field H_{sat}, and we define it as the field where the magnetization during the upsweep reaches 99% of the value during the preceding downsweep. Figure B.2 shows H_{sat} versus the thickness of Ni, d_{Ni}. At low temperatures, defects or surface roughness can cause H_{sat} to increase significantly for very low thicknesses, probably due to pinning of domain walls.

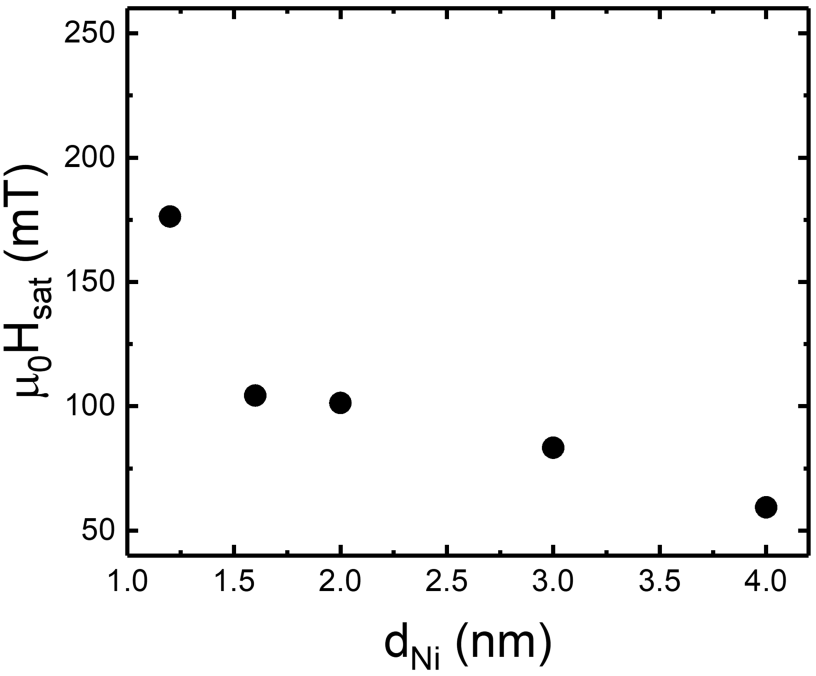

Figure B.2: **H_{sat} vs d_{Ni} for Ni(x).** Figure was taken from [26].

Appendix C

Effect of measurement temperature on the magnetic properties of Ni and Ni/Ru/Ni synthetic antiferromagnets

The discussion in this appendix was published in [26]. In Chapter 4, we found strong antiferromagnetic coupling (and the first peak) for the Ni(2.0)/Ru(0.9)/Ni(2.0) sample. The M vs H curves for this sample show minimal hysteresis. But for the sample at the second peak, i.e Ni(2.0)/Ru(0.9)/Ni(2.0), the loops have wider openings due to a weaker coupling, magnetocrystalline anisotropy and disorder. We wanted to study the effect of the low measurement temperatures on the coupling strength and the shape of the M vs H curves. We measured M vs H curves for the Ni(2.0)/Ru(2.3)/Ni(2.0) sample from 10 K to 340 K in steps of 30 K and data for a selected set of temperatures are shown in the inset of Fig. C.1. We also extracted the saturation magnetization values from these curves and plotted them versus the measurement temperature in the same figure.

As seen in Fig. C.1, the saturation magnetization value of Ni decreases with increasing temperature, as expected. However, we also see an apparent improvement in the antiferromagnetic coupling (the hysteretic gap between the loops decreases) between the Ni layers with increasing temperature. To determine the cause behind this effect, we performed a similar study on a Ni(4.0) sample fabricated earlier and discussed in the previous appendix. We measured M vs H curves for the Ni(4.0) sample from 10 K to 340 K in steps of 30 K, as shown in the inset of Fig. C.2. We also extracted the saturation magnetization values from these curves and plotted them versus the measurement temperature in the same figure.

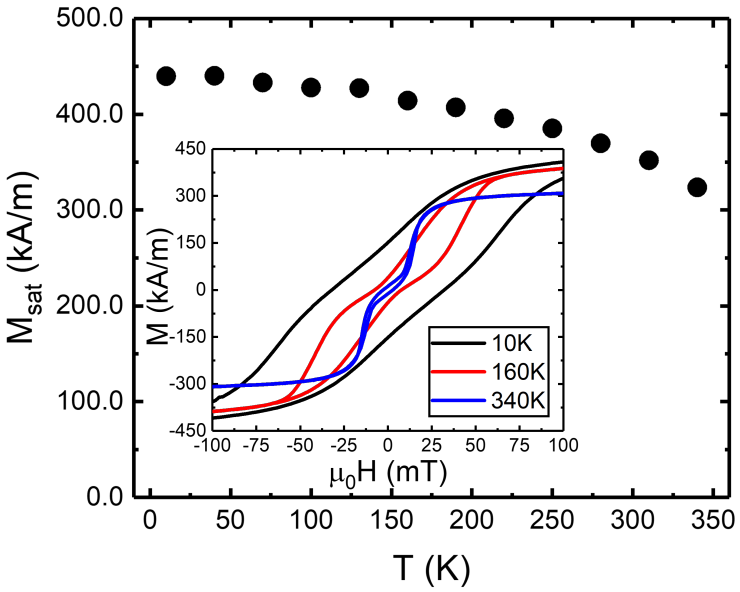

Figure C.1: **Temperature effects on magnetic properties of Ni(2.0)/Ru(2.3)/Ni(2.0).** Saturation magnetization (M_{sat}) vs measurement temperature (T) for Ni(2.0)/Ru(2.3)/Ni(2.0). *Inset:* M vs H curves for a selected set of measurement temperatures. Figure was taken from [26].

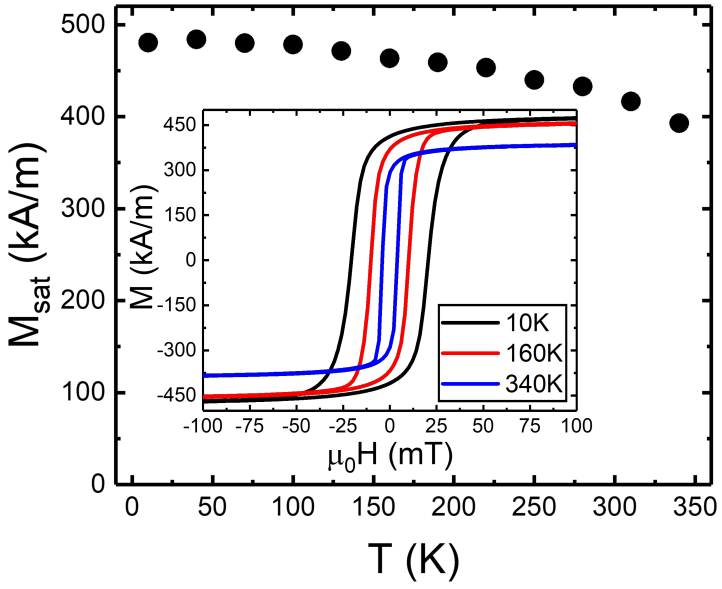

Figure C.2: **Temperature effects on magnetic properties of Ni(4.0).** Saturation magnetizaton (M_{sat}) versus measurement temperature (T) for Ni(4.0). **Inset:** M vs H curves for a selected set of measurement temperatures. Figure was taken from [26].

Figure C.2 shows a similar closing of the hysteretic gap with increasing temperature as seen in the SAFs. Therefore, this effect seen in the SAF is due to the magnetic behavior of the Ni films, rather than an increase in the antiferromagnetic coupling strength through the Ru. We also found that the M_{sat} values are higher for Ni than for the SAF, hinting at magnetic dead layers at the two Ni/Ru interfaces.

We studied the effect of temperature on the coercivity of both of these samples next. The coercivity of Ni(4.0) was found by fitting the hysteresis loops to the Gaussian error function discussed in Eqn. 2.26. Since the same is not possible for Ni(2.0)/Ru(2.3)/Ni(2.0) because of the lack of typical hysteresis, we determined the coercivity by taking the average of the coercivity at $M = 0$ for upsweep and downsweep of the M vs H. The coercivities were calculated by fitting a few points around the $M = 0$ crossing point to a straight line. Figure C.3 shows the dependence of coercivity (H_c) on the measurement temperature (T) for both the samples.

At high temperatures, the SAF has lower H_c than the plain Ni film, as expected. At lower temperature, we see the opposite which was somewhat surprising. However, each Ni film in the SAF has a thickness of only 2 nm rather than 4 nm, which makes the comparison somewhat unfair. The H_c of Ni films increases rapidly as their thickness is reduced, as shown in Fig. C.3, which could be causing this crossover effect.

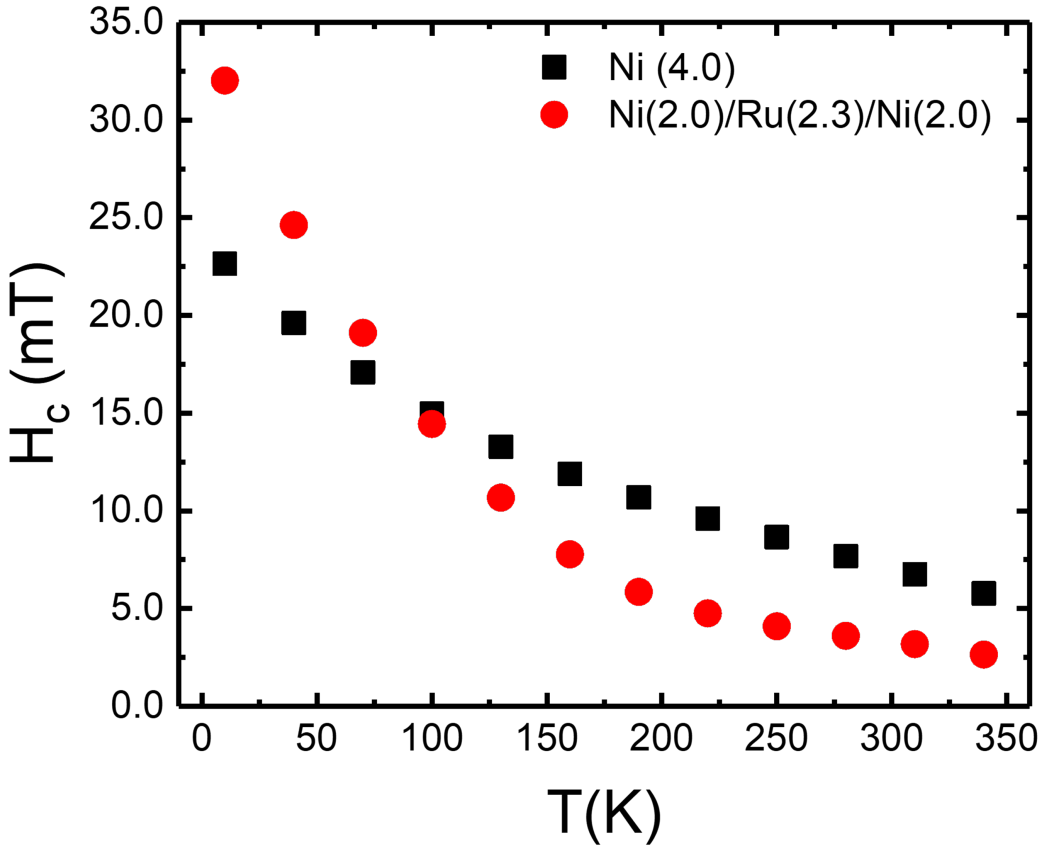

Figure C.3: **H_c vs T for Ni(4.0) and Ni(2.0)/Ru(2.3)/Ni(2.0).** Figure was taken from [26].

Appendix D

Remanence in Ni/Ru/Ni Josephson junctions

The discussion in this appendix was published in [26]. The Fraunhofer patterns for Ni/Ru/Ni (shown in Fig. 4.12) are well centered at zero field, indicating that the Ni/Ru/Ni SAF inside the junction has no visible remanent magnetic moment. This appears to contradict the remanent magnetization visible in the M vs H curves shown in Fig. 4.5 for blanket films. However, this is simply due to the different field ranges of the two measurements – 2 T for the film characterization measurements versus 100 mT for the Josephson junction measurements. We remeasured the M vs H curves for the Ni(2.0)/Ru(0.9)/Ni(2.0) SAF up to a field of 100 mT to be consistent with the field range of our I_cR_N measurements. Figure D.1 shows a blow-up of both curves (new measurement versus previous measurement for the blanket film). As we can see, the remanent magnetization in the case of low $H_{\max}$ is much smaller when compared to that of high $H_{\max}$. To estimate the amount of shift this remanent magnetization would produce in our junctions, we modify the expression for the magnetic flux Φ that appears in Eqn. 2.48 to the following:

$$\Phi = \mu_0 H(2\lambda_L + d_N + d_F)w + \mu_0 M d_F w \tag{D.1}$$

where M is the net magnetization of the ferromagnetic layers and all other quantities are the same as before. This implies that the magnetization would shift the Fraunhofer curves

by a field

$$H_{\text{shift}} = \frac{-Md_F}{(2\lambda_L + d_N + d_F)} \tag{D.2}$$

The M_{rem} in the low H_{max} measurement for Ni(2.0)/Ru(0.9)/Ni(2.0) is estimated to be 3.3 kA/m. Using this value in the above equation, we calculate the shift around zero applied field in the Fraunhofer pattern to be $\mu_0 H_{\text{shift}} = -0.12$ mT. This shift is too small to be visible; hence our Fraunhofers patterns are symmetric around zero field and exhibit no visible hysteresis between upsweep and downsweep measurements.

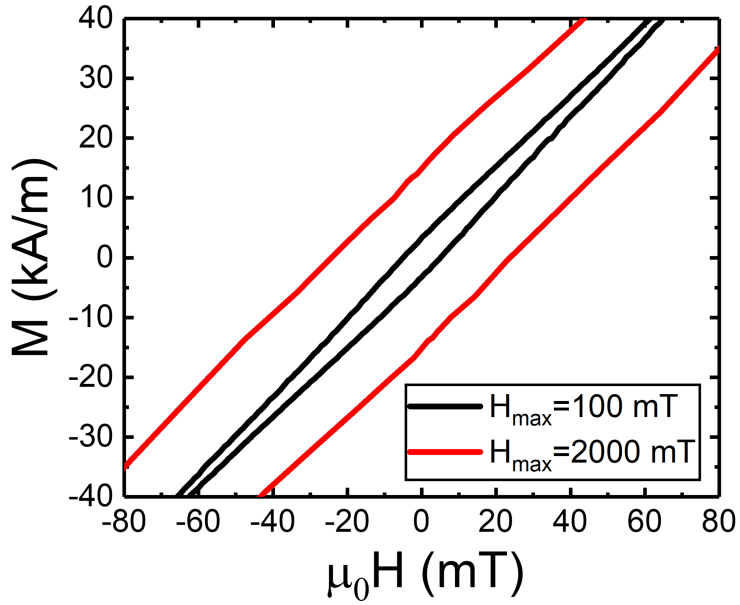

Figure D.1: **M vs H for Ni(2.0)/Ru(0.9)/Ni(2.0)**. The measurements were performed at two different maximum fields of 100 and 2000 mT. Figure was taken from [26].

Appendix E

Junction width variation in Ni/NiFe/Ni Josephson junctions

The discussion in this appendix was published in [101]. The effective London penetration depth $2\lambda_{\text{eff}}$ in the flux Φ in Eqn. 2.49 is given by:

$$2\lambda_{\text{eff}} = \lambda_1 \tanh\left(\frac{d_1}{2\lambda_1}\right) + \lambda_2 \tanh\left(\frac{d_2}{2\lambda_2}\right) \tag{E.1}$$

where λ_1, λ_2 are the London penetration depths and d_1, d_2 are the thicknesses of the top and bottom leads, respectively [106]. $2\lambda_{\text{eff}}$ approaches $\lambda_1 + \lambda_2$ when both electrodes are much thicker than their respective London penetration depths. In the limit of thin electrodes, $2\lambda_{\text{eff}}$ approaches $(d_1 + d_2)/2$ instead. Our Ni/NiFe/Ni Josephson junctions are in the intermediate case, with each electrode thickness within a factor of two of its λ value.

The λ for our bottom $[\text{Nb/Al}]_3$/Nb multilayer was recently found to be in the vicinity of 185 nm [24, 107] – much longer than the value of 85 nm we expect for our sputtered Nb films [82]. Using $\lambda = 185$ nm and 85 nm for the bottom and top electrodes, respectively, and using $d_1 = 102.2$ nm and $d_2 = 150$ nm, we get $2\lambda_{\text{eff}} \approx 110$ nm from Eqn. E.1. The magnetic flux through through the junction due to the external field is calculated by adding the total thickness of the normal layers, $d_N = 14$ nm, and the thickness of the ferromagnetic layers, d_F. Using the above values, we can extract the junction widths, w, from the fits of Eqn. 2.48 to the experimental Airy patterns. w is plotted versus total F-layer thickness d_F in the lower panel of Fig. E.1 for the complete set of Ni(0.4)/NiFe(d_F-0.8)/Ni(0.4) junctions. The data show a lot of scatter, however, the average junction width is about 550 nm, which

agrees with estimates obtained from scanning electron microscopy pictures taken during the fabrication process.

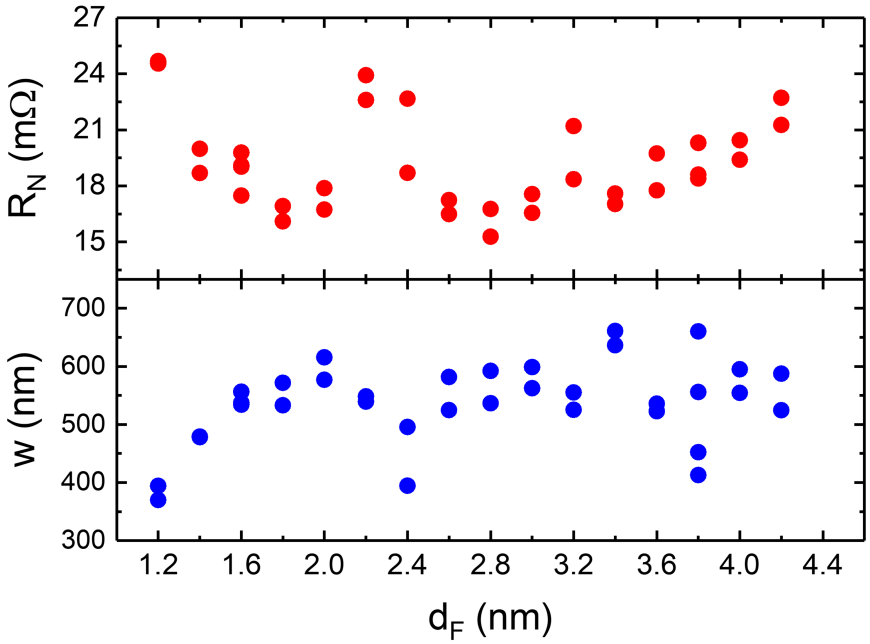

Figure E.1: **R_N and w vs d_F for Ni(0.4)/NiFe(d_F-0.8)/Ni(0.4).** Figure taken from [101].

In the upper panel of Fig. E.1, we show the normal state resistance R_N of the junctions. There seems to be an inverse correlation between these two, especially in the extreme cases. Ideally, there should not be so much scatter in the junction widths since the e-beam lithography process is highly reproducible. We suspect that the reason behind this scatter is the SiO_x thermal deposition, which is the least well-controlled process. The color of the deposited SiO_x layer varies between different shades of brown which indicates an unintended thickness variation. This variation in SiO_x thickness can lead to variations in the lateral opening size of the junctions, which in turn leads to varying resistances. Optical microscopy inspection of our junctions during the fabrication process reveals that the junctions with higher R_N values tend to have smaller junction openings after lift-off of the negative e-beam resist. This is consistent with those junctions having smaller extracted junction widths w.

For the data shown in Fig. E.1, the mean and standard deviation of the resistance measurements were found to be 19.2 $\pm$ 2.5 mΩ, whereas for the widths we found 551.2 $\pm$ 69.6 nm. In relative terms, the resistances vary by $\pm$ 13% while the widths vary by $\pm$ 12.6%. Since resistance is inversely proportional to junction area, one would expect larger relative variation in resistance. However, since this is not the case, it indicates that other unknown factors contribute to the width variation.

Appendix F

Fraunhofer field shifts in Ni/NiFe/Ni Josephson junctions

The discussion in this appendix was published in [101]. As discussed earlier, the data shown in Fig. 5.4 are shifted in field due to the contributions of the Ni and NiFe magnetizations to the total magnetic flux in the junction. Assuming that the magnetic trilayer is uniformly magnetized at remanence (and ignoring any magnetic flux that returns inside the junction due to the F-layers), the field shift is given by

$$\mu_0 H_{\text{shift}} = \frac{-\mu_0(M_{\text{Ni}} d_{\text{Ni}} + M_{\text{NiFe}} d_{\text{NiFe}})}{(2\lambda_{\text{eff}} + d_N + d_{\text{Ni}} + d_{\text{NiFe}})} \tag{F.1}$$

where we have replaced Md_F in Eqn. 2.49 with $M_{\text{Ni}} d_{\text{Ni}} + M_{\text{NiFe}} d_{\text{NiFe}}$. The field shift values obtained by fitting the Fig. 5.4 data to Eqn. 2.48 are plotted versus NiFe thickness in Fig. F.1 for the Ni(0.4)/NiFe(d_{NiFe})/Ni(0.4) and Ni(0.2)/NiFe(d_{NiFe})/Ni(0.2) sample sets, in red circles and black squares, respectively.

The field shift increases with increasing NiFe thickness, as expected. However, there is significant scatter in the data. The solid lines are the predicted values calculated from Eqn. F.1 using the values of M_{Ni} and M_{NiFe} from the magnetic data in Fig. 5.3 and the $2\lambda_{\text{eff}} + d_N = 124$ nm, as calculated in the previous appendix. All the data points fall below the lines, which could be because of two possible reasons: either there is a substantial amount of flux from the F layer that returns inside the junction, or the remanent magnetization of the Ni/NiFe/Ni trilayers is less than the saturation magnetization. The latter might be because of some magnetic relaxation at the ends of the ellipses, or due to domain formation.

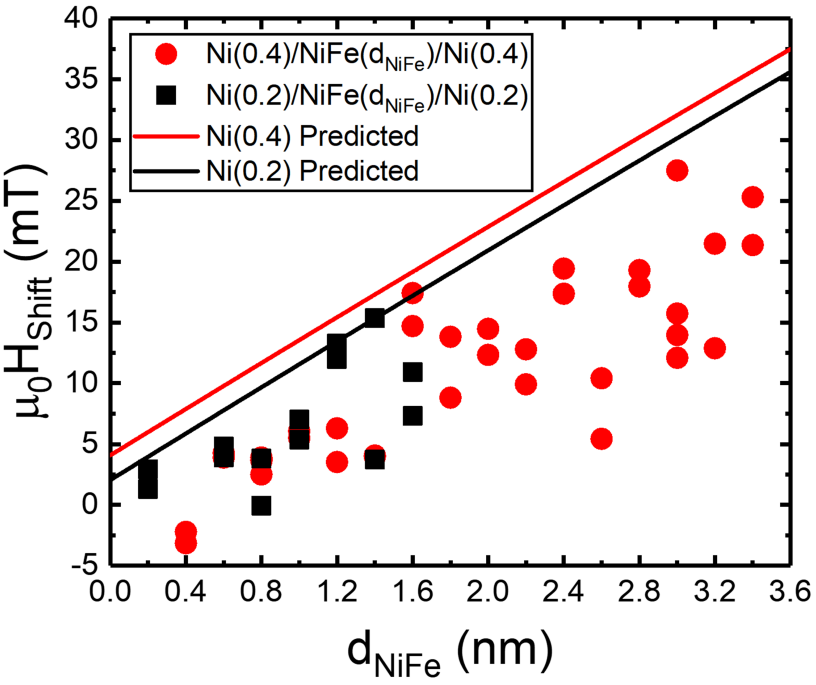

Figure F.1: **H_{shift} vs d_{NiFe} for Ni(0.4)/NiFe/Ni(0.4) and Ni(0.2)/NiFe/Ni(0.2).** Solid lines are predictions based on Eqn. F.1. Figure was taken from [101].

Appendix G

Critical temperatures of bottom and top Nb leads

The critical temperature of Nb films can vary with the thickness and roughness of the deposition. We deposited our bottom $[Nb(25)/Al(2.4)]_3/Nb(20)$ and top Nb(160)/Au(10) leads on Si substrates. To determine their critical temperatures, we then measured their moment/area versus temperature in the range of 5-10 K (in steps of 0.1 K) at a fixed applied field of 100 Oe, using the DC mode of MPMS3. Figure G.1 shows the plot of moment/area versus temperature.

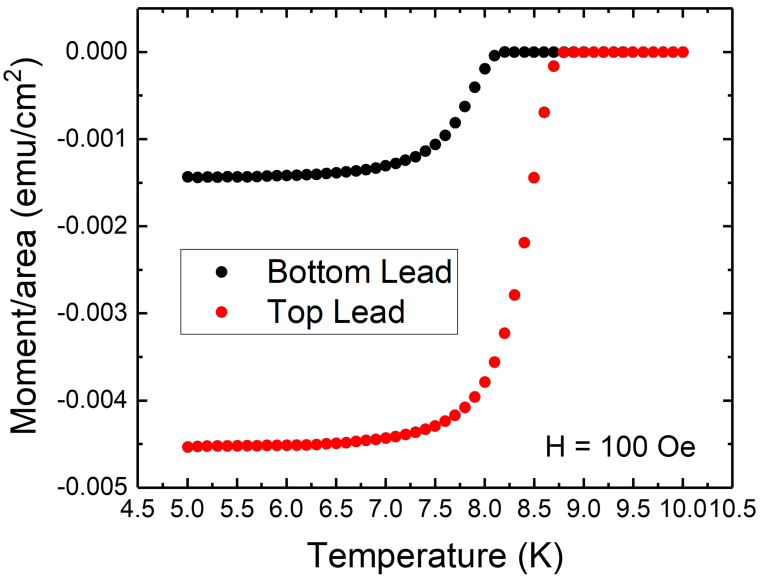

Figure G.1: **DC Moment/area vs temperature for bottom and top leads.** The measurement was performed at a fixed applied field of 100 Oe.

Below the critical temperature, the moment/area starts dropping. As seen in Fig. G.1, the critical temperatures of the bottom and top leads are around 7.9 K and 8.7 K, respectively.

REFERENCES

REFERENCES

[1] Nicola Jones. How to stop data centres from gobbling up the world's electricity. *Nature*, 561(7722):163–167, 2018.

[2] David Mytton. Data centre water consumption. *npj Clean Water*, 4(1):1–6, 2021.

[3] D. Scott Holmes, Andrew L. Ripple, and Marc A. Manheimer. Energy-Efficient Superconducting Computing—Power Budgets and Requirements. *IEEE Transactions on Applied Superconductivity*, 23(3):1701610–1701610, 2013.

[4] Marc A. Manheimer. Cryogenic computing complexity program: Phase 1 introduction. *IEEE Transactions on Applied Superconductivity*, 25(3):1–4, 2015.

[5] D. Scott Holmes, Alan M. Kadin, and Mark W. Johnson. Superconducting computing in large-scale hybrid systems. *Computer*, 48(12):34–42, 2015.

[6] Caleb Howington, Alex Opremcak, Robert McDermott, Alex Kirichenko, Oleg A. Mukhanov, and Britton L. T. Plourde. Interfacing Superconducting Qubits With Cryogenic Logic: Readout. *IEEE Trans. Appl. Supercond.*, 29(5):1–5, 2019.

[7] Dudley A. Buck. The cryotron–a superconductive computer component. *Proceedings of the IRE*, 44(4):482–493, 1956.

[8] Brian David Josephson. Possible new effects in superconductive tunnelling. *Physics letters*, 1(7):251–253, 1962.

[9] Brian David Josephson. Supercurrents through barriers. *Advances in Physics*, 14(56):419–451, 1965.

[10] Wilhelm Anacker. Josephson computer technology: An IBM research project. *IBM Journal of research and development*, 24(2):107–112, 1980.

[11] Konstantin K. Likharev, Oleg A. Mukhanov, and Vasilii K. Semenov. Resistive single flux quantum logic for the Josephson-junction digital technology. *SQUID*, 85:1103–1108, 1985.

[12] Konstantin K. Likharev and Vasilii K. Semenov. RSFQ logic/memory family: A new Josephson-junction technology for sub-terahertz-clock-frequency digital systems. *IEEE Transactions on Applied Superconductivity*, 1(1):3–28, 1991.

[13] Quentin P. Herr, Anna Y. Herr, Oliver T. Oberg, and Alexander G. Ioannidis. Ultra-low-power superconductor logic. *Journal of applied physics*, 109(10):103903, 2011.

[14] W. Chen, A. V. Rylyakov, V. Patel, J. E. Lukens, and K. K. Likharev. Rapid single flux quantum T-flip flop operating up to 770 GHz. *IEEE Transactions on Applied Superconductivity*, 9(2):3212–3215, 1999.

[15] Oleg A. Mukhanov. Energy-efficient single flux quantum technology. *IEEE Transactions on Applied Superconductivity*, 21(3):760–769, 2011.

[16] D. E. Kirichenko, Saad Sarwana, and A. F. Kirichenko. Zero static power dissipation biasing of RSFQ circuits. *IEEE Transactions on Applied Superconductivity*, 21(3):776–779, 2011.

[17] Mark H. Volkmann, Anubhav Sahu, Coenrad J. Fourie, and Oleg A. Mukhanov. Implementation of energy efficient single flux quantum digital circuits with sub-aJ/bit operation. *Superconductor Science and Technology*, 26(1):015002, 2012.

[18] Masamitsu Tanaka, Atsushi Kitayama, Tomohito Koketsu, Masato Ito, and Akira Fujimaki. Low-energy consumption RSFQ circuits driven by low voltages. *IEEE transactions on applied superconductivity*, 23(3):1701104–1701104, 2013.

[19] Naoki Takeuchi, Yuki Yamanashi, and Nobuyuki Yoshikawa. Energy efficiency of adiabatic superconductor logic. *Superconductor Science and Technology*, 28(1):015003, 2014.

[20] F. Bedard, N. Welker, G. R. Cotter, M. A. Escavage, and J. T. Pinkston. Superconducting technology assessment. *National Security Agency, Office of Corporate Assessments*, 2005.

[21] E. C. Gingrich, Bethany M. Niedzielski, Joseph A. Glick, Yixing Wang, D. L. Miller, Reza Loloee, W. P. Pratt Jr, and Norman O. Birge. Controllable 0–π Josephson junctions containing a ferromagnetic spin valve. *Nature Physics*, 12(6):564–567, 2016.

[22] Joseph A. Glick, Mazin A. Khasawneh, Bethany M. Niedzielski, Reza Loloee, W. P. Pratt Jr, Norman O. Birge, E. C. Gingrich, P. G. Kotula, and N. Missert. Critical current oscillations of elliptical Josephson junctions with single-domain ferromagnetic layers. *Journal of Applied Physics*, 122(13):133906, 2017.

[23] Joseph A. Glick, Samuel Edwards, Demet Korucu, Victor Aguilar, Bethany M. Niedzielski, Reza Loloee, W.P. Pratt Jr, Norman O. Birge, P.G. Kotula, and N. Missert. Spin-triplet supercurrent in Josephson junctions containing a synthetic antiferromagnet with perpendicular magnetic anisotropy. *Physical Review B*, 96(22):224515, 2017.

[24] Alexander E. Madden, Joshua C. Willard, Reza Loloee, and Norman O. Birge. Phase controllable Josephson junctions for cryogenic memory. *Superconductor Science and Technology*, 32(1):015001, 2018.

[25] Victor Aguilar, Demet Korucu, Joseph A. Glick, Reza Loloee, W. P. Pratt Jr, and Norman O. Birge. Spin-polarized triplet supercurrent in Josephson junctions with perpendicular ferromagnetic layers. *Physical Review B*, 102(2):024518, 2020.

[26] Swapna Sindhu Mishra, Reza Loloee, and Norman O. Birge. Supercurrent transmission through Ni/Ru/Ni synthetic antiferromagnets. *Applied Physics Letters*, 119(17):172603, 2021.

[27] C. Bell, G. Burnell, C. W. Leung, E. J. Tarte, D. J. Kang, and M. G. Blamire. Controllable Josephson current through a pseudospin-valve structure. *Appl. Phys. Lett.*, 84(7):1153–1155, 2004.

[28] Valery V. Ryazanov, Vitaly V. Bol'ginov, Danila S. Sobanin, Igor V. Vernik, Sergey K. Tolpygo, Alan M. Kadin, and Oleg A. Mukhanov. Magnetic Josephson Junction Technology for Digital and Memory Applications. *Physics Procedia*, 36:35–41, 2012.

[29] Timofei I. Larkin, Vitaly V. Bol'ginov, Vasily S. Stolyarov, Valery V. Ryazanov, Igor V. Vernik, Sergey K. Tolpygo, and Oleg A. Mukhanov. Ferromagnetic Josephson switching device with high characteristic voltage. *Appl. Phys. Lett.*, 100(22):222601, 2012.

[30] Igor V. Vernik, Vitaly V. Bol'ginov, Sergey V. Bakurskiy, Alexander A. Golubov, Mikhail Yu. Kupriyanov, Valery V. Ryazanov, and Oleg A. Mukhanov. Magnetic Josephson Junctions With Superconducting Interlayer for Cryogenic Memory. *IEEE Trans. Appl. Supercond.*, 23(3):1701208–1701208, 2013.

[31] Makram Abd El Qader, R. K. Singh, Sarah N. Galvin, L. Yu, J. M. Rowell, and N. Newman. Switching at small magnetic fields in Josephson junctions fabricated with ferromagnetic barrier layers. *Appl. Phys. Lett.*, 104(2):022602, 2014.

[32] Burm Baek, William H. Rippard, Samuel P. Benz, Stephen E. Russek, and Paul D. Dresselhaus. Hybrid superconducting-magnetic memory device using competing order parameters. *Nature Comm.*, 5(1):1–6, 2014.

[33] Ian M. Dayton, Tessandra Sage, Eric C. Gingrich, Melissa G. Loving, Thomas F. Ambrose, Nathan P. Siwak, Shawn Keebaugh, Christopher Kirby, Donald L. Miller, Anna Y. Herr, Quentin P. Herr, and Ofer Naaman. Experimental Demonstration of a Josephson Magnetic Memory Cell With a Programmable π-Junction. *IEEE Magnetics Letters*, 9:1–5, 2018.

[34] Said Tehrani, J. M. Slaughter, E. Chen, M. Durlam, J. Shi, and M. DeHerren. Progress and outlook for MRAM technology. *IEEE Transactions on Magnetics*, 35(5):2814–2819, 1999.

[35] Anna Y. Herr and Quentin P. Herr. Josephson magnetic random access memory system and method, September 18 2012. US Patent 8,270,209.

[36] A.Y. Herr, Q.P. Herr, and O. Naaman. Phase hysteretic magnetic Josephson junction memory cell. *US Patent Application*, pages 2015–0094207, 2015.

[37] J. M. Slaughter, R. W. Dave, M. DeHerrera, M. Durlam, B. N. Engel, J. Janesky, N. D. Rizzo, and S. Tehrani. Fundamentals of MRAM technology. *Journal of superconductivity*, 15(1):19–25, 2002.

[38] Joseph A. Glick, Victor Aguilar, Adel B. Gougam, Bethany M. Niedzielski, Eric C. Gingrich, Reza Loloee, William P. Pratt Jr, and Norman O. Birge. Phase control in a spin-triplet SQUID. *Science advances*, 4(7):eaat9457, 2018.

[39] Jack Bass. CPP magnetoresistance of magnetic multilayers: A critical review. *Journal of Magnetism and Magnetic Materials*, 408:244–320, 2016.

[40] H. Kamerlingh Onnes. The Superconductivity of Mercury. *Comm. Phys. Lab. Univ., Leiden*, pages 122–124, 1911.

[41] Walther Meissner and Robert Ochsenfeld. Ein neuer effekt bei eintritt der supraleitfähigkeit. *Naturwissenschaften*, 21(44):787–788, 1933.

[42] J. Bardeen, L. N. Cooper, and J. R. Schrieffer. Microscopic theory of superconductivity. *Phys. Rev.*, 106:162–164, Apr 1957.

[43] Piotr Jaworski. Diagram of the Meissner effect. Magnetic field lines, represented as arrows, are excluded from a superconductor when it is below its critical temperature., 2005. https://commons.wikimedia.org/wiki/File:EfektMeisnera.svg.

[44] Fritz London and Heinz London. The electromagnetic equations of the supraconductor. *Proceedings of the Royal Society of London. Series A-Mathematical and Physical Sciences*, 149(866):71–88, 1935.

[45] Vitaly L. Ginzburg and Lev D. Landau. On the theory of superconductivity. In *On superconductivity and superfluidity*, pages 113–137. Springer, 2009.

[46] C.A. Reynolds, Bernard Serin, W.H. Wright, and L.B. Nesbitt. Superconductivity of isotopes of mercury. *Physical Review*, 78(4):487, 1950.

[47] Emanuel Maxwell. Isotope effect in the superconductivity of mercury. *Physical Review*, 78(4):477, 1950.

[48] Herbert Fröhlich. Interaction of electrons with lattice vibrations. *Proceedings of the Royal Society of London. Series A. Mathematical and Physical Sciences*, 215(1122):291–298, 1952.

[49] John Bardeen and David Pines. Electron-phonon interaction in metals. *Physical Review*, 99(4):1140, 1955.

[50] Leon N. Cooper. Bound electron pairs in a degenerate Fermi gas. *Physical Review*, 104(4):1189, 1956.

[51] Michael Tinkham. *Introduction to superconductivity*. Courier Corporation, 2004.

[52] R. E. Glover III and M. Tinkham. Transmission of superconducting films at millimeter-microwave and far infrared frequencies. *Physical Review*, 104(3):844, 1956.

[53] Ivar Giaever. Energy gap in superconductors measured by electron tunneling. *Physical Review Letters*, 5(4):147, 1960.

[54] Joseph Allen Glick III. *Ferromagnetic Josephson Junctions Carrying Spin-Triplet Supercurrent for Cryogenic Memory*. Michigan State University, 2017.

[55] Pierre Curie. *Oeuvres de Pierre Curie: publiées par les soins de la Société française de physique*. Gauthier-Villars, 1908.

[56] Pierre Weiss. La variation du ferromagnétisme avec la température. *Comptes Rendus*, 143:1136–1139, 1906.

[57] Werner Heisenberg. Mehrkörperproblem und Resonanz in der Quantenmechanik. *Zeitschrift für Physik*, 38(6):411–426, 1926.

[58] Paul Adrien Maurice Dirac. On the theory of quantum mechanics. *Proceedings of the Royal Society of London. Series A, Containing Papers of a Mathematical and Physical Character*, 112(762):661–677, 1926.

[59] Lev D. Landau and Evgeny Lifshitz. On the theory of the dispersion of magnetic permeability in ferromagnetic bodies. In *Perspectives in Theoretical Physics*, pages 51–65. Elsevier, 1992.

[60] Edmund Clifton Stoner and E. P. Wohlfarth. A mechanism of magnetic hysteresis in heterogeneous alloys. *Philosophical Transactions of the Royal Society of London. Series A, Mathematical and Physical Sciences*, 240(826):599–642, 1948.

[61] RockMagnetist. A plot of magnetic hysteresis loops predicted by Stoner-Wohlfarth theory for various angles between field and easy axis., 2010. https://commons.wikimedia.org/wiki/File:SwHyst_vs_angle.svg.

[62] R. Holm and W. Meissner. Messungen mit Hilfe von flüssigem Helium. XIII. *Zeitschrift für Physik*, 74(11):715–735, 1932.

[63] A. F. Andreev. The thermal conductivity of the intermediate state in superconductors. *Zh. Eksperim. i Teor. Fiz.*, 46, 1964.

[64] Shashi K. Upadhyay, Akilan Palanisami, Richard N. Louie, and R. A. Buhrman. Probing Ferromagnets with Andreev Reflection. *Phys. Rev. Lett.*, 81:3247–3250, Oct 1998.

[65] R. J. Soulen, J. M. Byers, M. S. Osofsky, B. Nadgorny, T. Ambrose, S. F. Cheng, P. R. Broussard, C. T. Tanaka, J. Nowak, J. S. Moodera, A. Barry, and J. M. D. Coey. Measuring the Spin Polarization of a Metal with a Superconducting Point Contact. *Science*, 282(5386):85–88, 1998.

[66] Alexandre I. Buzdin, L. N. Bulaevskii, and S. V. Panyukov. Critical-current oscillations as a function of the exchange field and thickness of the ferromagnetic metal (F) in an SFS Josephson junction. *JETP lett*, 35(4):178–180, 1982.

[67] Peter Fulde and Richard A. Ferrell. Superconductivity in a strong spin-exchange field. *Physical Review*, 135(3A):A550, 1964.

[68] A. I. Larkin and Y. N. Ovchinnikov. Inhomogeneous state of superconductors. *Soviet Physics-JETP*, 20:762–769, 1965.

[69] Eugene A. Demler, G. B. Arnold, and M. R. Beasley. Superconducting proximity effects in magnetic metals. *Physical Review B*, 55(22):15174, 1997.

[70] Alexandre I. Buzdin. Proximity effects in superconductor-ferromagnet heterostructures. *Reviews of modern physics*, 77(3):935, 2005.

[71] L. N. Bulaevskii, V. V. Kuzii, and A. A. Sobyanin. Superconducting system with weak coupling to the current in the ground state. *JETP lett*, 25(7):290–294, 1977.

[72] V. V. Ryazanov, V. A. Oboznov, A. Yu. Rusanov, A. V. Veretennikov, Alexandre Avraamovitch Golubov, and J. Aarts. Coupling of two superconductors through a ferromagnet: Evidence for a π junction. *Physical review letters*, 86(11):2427, 2001.

[73] T. Kontos, M. Aprili, J. Lesueur, F. Genêt, B. Stephanidis, and R. Boursier. Josephson junction through a thin ferromagnetic layer: negative coupling. *Physical Review Letters*, 89(13):137007, 2002.

[74] Alexandre I. Buzdin and M. Yu. Kupriyanov. Josephson junction with a ferromagnetic layer. *JETP lett*, 53(6):321, 1991.

[75] F. S. Bergeret, A. F. Volkov, and K. B. Efetov. Josephson current in superconductor-ferromagnet structures with a nonhomogeneous magnetization. *Physical Review B*, 64(13):134506, 2001.

[76] N. G. Pugach, M. Yu. Kupriyanov, E. Goldobin, R. Kleiner, and D. Koelle. Superconductor-insulator-ferromagnet-superconductor Josephson junction: From the dirty to the clean limit. *Physical Review B*, 84(14):144513, 2011.

[77] Z. Radović, N. Lazarides, and N. Flytzanis. Josephson effect in double-barrier superconductor-ferromagnet junctions. *Physical Review B*, 68(1):014501, 2003.

[78] Paul H. Barsic, Oriol T. Valls, and Klaus Halterman. Thermodynamics and phase diagrams of layered superconductor/ferromagnet nanostructures. *Physical Review B*, 75(10):104502, 2007.

[79] Hervé Ness, Ivan A. Sadovskyy, Andrey E. Antipov, Mark van Schilfgaarde, and Roman M. Lutchyn. Supercurrent decay in ballistic magnetic Josephson junctions. *npj Computational Materials*, 8(1):1–11, 2022.

[80] Burm Baek, Michael L. Schneider, Matthew R. Pufall, and William H. Rippard. Anomalous supercurrent modulation in Josephson junctions with Ni-based barriers. *IEEE Transactions on Applied Superconductivity*, 28(7):1–5, 2018.

[81] J. W. A. Robinson, S. Piano, G. Burnell, C. Bell, and M. G. Blamire. Zero to π transition in superconductor-ferromagnet-superconductor junctions. *Physical Review B*, 76(9):094522, 2007.

[82] Trupti S. Khaire, W. P. Pratt Jr, and Norman O. Birge. Critical current behavior in Josephson junctions with the weak ferromagnet PdNi. *Physical Review B*, 79(9):094523, 2009.

[83] M. A. Ruderman and C. Kittel. Indirect Exchange Coupling of Nuclear Magnetic Moments by Conduction Electrons. *Phys. Rev.*, 96:99–102, Oct 1954.

[84] Tadao Kasuya. A Theory of Metallic Ferro- and Antiferromagnetism on Zener's Model. *Progress of Theoretical Physics*, 16(1):45–57, 07 1956.

[85] Kei Yosida. Magnetic Properties of Cu-Mn Alloys. *Phys. Rev.*, 106:893–898, Jun 1957.

[86] Stuart S. P. Parkin. Systematic variation of the strength and oscillation period of indirect magnetic exchange coupling through the 3d, 4d, and 5d transition metals. *Physical Review Letters*, 67(25):3598, 1991.

[87] H. A. M. Van den Berg, Reinder Coehoorn, M. A. M. Gijs, P. Grünberg, T. Rasing, and K. Röll. *Magnetic multilayers and giant magnetoresistance: fundamentals and industrial applications*, volume 37. Springer Science & Business Media, 2013.

[88] Robert C. O'handley. *Modern magnetic materials: principles and applications*. Wiley, 2000.

[89] Ya. M. Blanter and F. W. J. Hekking. Supercurrent in long SFFS junctions with antiparallel domain configuration. *Physical Review B*, 69(2):024525, 2004.

[90] A. Vedyayev, C. Lacroix, N. Pugach, and N. Ryzhanova. Spin-valve magnetic sandwich in a Josephson junction. *EPL (Europhysics Letters)*, 71(4):679, 2005.

[91] Benoît Crouzy, S. Tollis, and D. A. Ivanov. Josephson current in a superconductor-ferromagnet junction with two noncollinear magnetic domains. *Physical Review B*, 75(5):054503, 2007.

[92] Sergey Viktorovich Bakurskiy, M. Yu. Kupriyanov, Artem Alexandrovich Baranov, Alexandre Avraamovitch Golubov, Nikolay Viktorovich Klenov, and Igor I. Soloviev. Proximity effect in multilayer structures with alternating ferromagnetic and normal layers. *JETP letters*, 102(9):586–593, 2015.

[93] H. Geng, J. W. Heckman, W. P. Pratt, J. Bass, F. J. Espinosa, S. D. Conradson, D. Lederman, and M. A. Crimp. Occasional "long-range" nonequilibrium body-centered-cubic structures in NiFe/Cu spin valves. *Journal of applied physics*, 86(8):4166–4175, 1999.

[94] Y. Blum, A. Tsukernik, M. Karpovski, and A. Palevski. Oscillations of the superconducting critical current in Nb-Cu-Ni-Cu-Nb junctions. *Physical review letters*, 89(18):187004, 2002.

[95] J. W. A. Robinson, S. Piano, G. Burnell, C. Bell, and M. G. Blamire. Critical current oscillations in strong ferromagnetic π junctions. *Physical review letters*, 97(17):177003, 2006.

[96] Mazin A. Khasawneh, Carolin Klose, W. P. Pratt Jr, and Norman O. Birge. Spin-memory loss at Co/Ru interfaces. *Physical Review B*, 84(1):014425, 2011.

[97] Norman O. Birge, Alexander E. Madden, and Ofer Naaman. Ferromagnetic Josephson junctions for cryogenic memory. In *Spintronics XI*, volume 10732, pages 124–134. SPIE, 2018.

[98] Shufeng Zhang and Peter M. Levy. Conductivity perpendicular to the plane of multilayered structures. *Journal of Applied Physics*, 69(8):4786–4788, 1991.

[99] S. F. Lee, W. P. Pratt Jr, Q. Yang, P. Holody, R. Loloee, P. A. Schroeder, and J. Bass. Two-channel analysis of CPP-MR data for Ag/Co and AgSn/Co multilayers. *Journal of magnetism and magnetic materials*, 118(1-2):L1–L5, 1993.

[100] T. Valet and A. Fert. Theory of the perpendicular magnetoresistance in magnetic multilayers. *Physical Review B*, 48(10):7099, 1993.

[101] Swapna Sindhu Mishra, Robert M. Klaes, Joshua Willard, Reza Loloee, and Norman O. Birge. Enhancement of supercurrent through ferromagnetic materials by interface engineering. *Phys. Rev. B*, 106:014519, Jul 2022.

[102] D. M Heim, N. G. Pugach, M. Yu. Kupriyanov, E. Goldobin, D. Koelle, R. Kleiner, N. Ruppelt, M. Weides, and H. Kohlstedt. The effect of normal and insulating layers on 0-π transitions in Josephson junctions with a ferromagnetic barrier. *New Journal of Physics*, 17(11):113022, 2015.

[103] C. A. Dos Santos, B. Rodmacq, M. Vaezzadeh, and B. George. Oscillatory magnetic coupling in Ag/Ni superlattices. *Applied physics letters*, 59(1):126–128, 1991.

[104] Shigeru Baba, Akira Kinbara, and Mitsuhiro Adachi. Island structure of sputter-deposited Ag thin films. *Vacuum*, 42(4):279–282, 1991.

[105] Y. Muhammad, Fridrik Magnus, Thomas Thersleff, P. Poulopoulos, Vassilios Kapaklis, Klaus Leifer, and Björgvin Hjörvarsson. Growth of polycrystalline Ag/Ni multilayers at room temperature. *Thin solid films*, 558:184–188, 2014.

[106] Antonio Barone and Gianfranco Paterno. *Physics and applications of the Josephson effect*. Wiley, 1982.

[107] P. Quarterman, Nathan Satchell, B. J. Kirby, Reza Loloee, Gavin Burnell, Norman O. Birge, and J. A. Borchers. Distortions to the penetration depth and coherence length of superconductor/normal-metal superlattices. *Phys. Rev. Materials*, 4:074801, Jul 2020.